Studies for the Laser Preheating Stage of Magnetized Liner Inertial Fusion

by

Stephanie M. Miller

A dissertation submitted in partial fulfillment
of the requirements for the degree of
Doctor of Philosophy
(Nuclear Engineering and Radiological Sciences)
in the University of Michigan
2024

Doctoral Committee:

Professor Ryan D. McBride, Co Chair,
Professor Carolyn C. Kuranz, Co Chair,
Professor Nicholas M. Jordan
Professor Eric Johnsen

Stephanie M. Miller

smmil@umich.edu

ORCID iD: 0000-0003-4881-548X

Dedication

Reflecting on my years in grad school I can't help but be reminded of the wise words of Jane Fonda: "I don't even know what I would do without my women friends. I have my friends therefore I am. I exist because I have my women friends. They make me stronger, they make me braver, they tap me on the shoulder when I might be in need of course correcting." This thesis is dedicated to the women in my life. This thesis would not exist without the following incredible women: Sylvia, Somya, Jenny, Polly, Kelsey, Hannah, Sophia, Chika, Sema, Jasleen, Angel, Sindhu, Mackenzie, Nomita, Estelle, Kimberly, Kathy, and Sonal.

Acknowledgments

I would like to give a special acknowledgement to Matt Gomez, my fellowship supervisor, co-PI, and most of all mentor. He taught me so much about science and even more about how to be a scientist. I would also like to thank Matt Weis for providing HYDRA simulations that bolstered the experimental results presented.

I would also like to thank my co-advisors Ryan McBride and Carolyn Kuranz for their financial, emotional, and academic support throughout my graduate career, and my committee members Nick Jordan and Eric Johnsen for their time and input to my dissertation work and thesis.

Finally, I would like like to thank my fellow graduate students (at Michigan and elsewhere) for their help, support, camaraderie, and most importantly friendship. Especially Paul Campbell for teaching me so much about physics, continuing to hold his patience with my many questions, and and spending countless late nights working on the LTD together.

This work was supported by the NNSA Laboratory Residency Graduate Fellowship under DOE contract DE-NA-0003864, the NNSA Stewardship Sciences Academic Program under DOE cooperative agreements DE-NA-0003764 and DE-NA-0004148, the NNSA-DS/SC-OFES HEDLP Program under DOE contract DE-NA-0002956, and by Sandia National Laboratories, a multi-mission laboratory managed and operated by National Technology and Engineering Solutions of Sandia, LLC., a wholly owned subsidiary of Honeywell International, Inc., for the U.S. Department of Energy's National Nuclear Security Administration under contract DE-NA-0003525.

TABLE OF CONTENTS

LIST OF FIGURES

FIGURE

LIST OF TABLES

TABLE

LIST OF APPENDICES

ABSTRACT

Magnetized Liner Inertial Fusion (MagLIF) is an approach to inertial confinement fusion being studied experimentally on the Z pulsed-power facility at Sandia National Laboratories (SNL). In MagLIF, a preheating laser enters a cylindrical target after passing through a laser entrance hole (LEH) window. The laser then heats the pressurized target fuel and sends shock waves through the fuel, towards the fuel-confining cylindrical metal shell (or "liner"). The shock waves are then transmitted into (and travel through) the liner wall.

To scale MagLIF to higher fusion yield and ultimately reach ignition, the laser energy coupled to the fuel must be maximized. Additionally, the laser must not ablate target materials that could mix into and contaminate the fuel. Energy coupling and mix mitigation can be improved with a method of removing the LEH window called "Laser Gate." Presented in this dissertation is a successful proof-of-concept of the Laser Gate method for removing the LEH window. In our experimental tests, the LEH window was removed from the target and cleared from the laser path. The measured window opening time (from fast framing camera images) agrees well with estimates from a simple window opening model.

Another important factor in preventing mix of target material into the fuel is the target walls. As the shock waves move through the walls, the walls first compress and then expand. There can also be material ejected from the liner that mixes into the fuel and degrades the fusion yield. An experimental campaign was conducted on the Omega EP laser facility to study this wall movement and to compare the experimental results with numerical simulations. The key takeaways from these experiments include the observation of an axial dependence of wall movement radially away from the axis, and density profiles that allude to potential mix of target material into the fuel.

Overall, the experimental results help to validate and compare HYDRA simulations and predictions. This is crucial because efforts at SNL to scale MagLIF to larger yields are ongoing, and this scaling work relies heavily on simulation capabilities. The discrepancies observed between the experimental wall movement and the simulated wall movement indicate that there are areas where the models, simulations, and measurements could be improved. These and other findings are presented and discussed throughout this dissertation.

CHAPTER 1

Introduction

Fusion occurs when two smaller atoms fuse together into a larger atom and energy is released. To increase the probability of fusion, the atoms are heated to the fourth state of matter, also known as plasma. These plasmas can be unstable and can quickly cool off. There are different methods to confine plasma long enough to ignite into a sustained fusion reaction. The sun is held together with gravitational confinement, while Magnetic Confinement Fusion (MCF) utilizes strong magnetic fields, and Inertial Confinement Fusion (ICF), the focus of this research, utilizes the inertia of an imploding fuel capsule (or "target").

Two of the mainline schemes within ICF are indirect drive ICF on the National Ignition Facility at Lawrence Livermore National Laboratory (LLNL) and Magnetized Liner Inertial Fusion (MagLIF) on the Z pulsed-power facility at Sandia National Laboratories (SNL). The National Ignition Facility (NIF) is the world's largest high-energy laser. The NIF contains 192 laser beams that all converge on a metallic tube (called a "hohlraum") which houses a spherical capsule containing deuterium-tritium (DT) fuel. It is considered indirect ICF because the lasers do not directly hit the capsule. Instead, they hit the inner walls of the hohlraum and generate x-rays. The x-rays absorbed by the capsule cause the capsule to implode radially inward, compressing the DT fuel inside to thermonuclear fusion conditions. The first laboratory demonstration of a burning-plasma state occurred recently at the NIF [7]. A burning plasma is when the main source of heating in the plasma comes from the the fusion reaction themselves. Even more recently, and even more impressively, fusion ignition was demonstrated on the NIF [7, 8]. Ignition is when a burn wave is successfully launched through a cryogenic fuel layer within the imploding capsule, and more energy is produced than input into

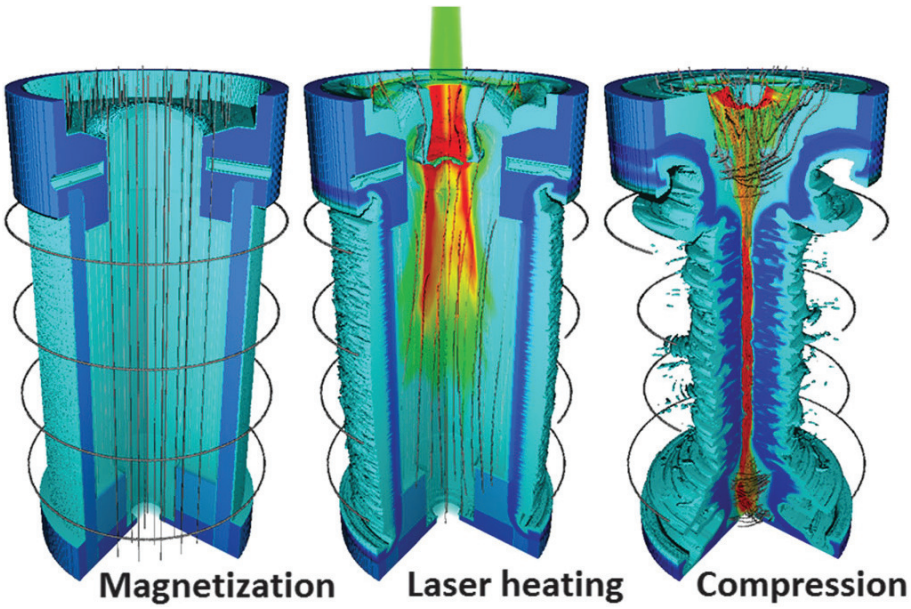

Figure 1.1: A schematic representation of the three phases of MagLIF. An axial current generates an azimuthal magnetic field, which is used to implode a gas-filled cylindrical target that is premagnetized with an axial field. Near the start of the implosion, the fuel is heated by the Z-Beamlet laser. The liner compresses and further heats the fuel to fusion-relevant temperatures and densities at stagnation. Reprinted figure with permission from M. R. Gomez *et al.*, Phys. Rev. Lett., **113**, 155003, (2014) Copyright 2014 by the American Physical Society. [1].

the system. This monumental achievement resulted in a fusion energy yield (3.15 MJ) that was greater than the laser energy delivered by the NIF laser (2.05 MJ). It is also a promising step toward reaching a self-sustaining fusion energy source.

Another approach to ICF in a laboratory setting is Magnetized Liner Inertial Fusion (MagLIF) [3, 9]. This concept is being experimentally tested on the Z pulsed-power facility at Sandia National Laboratories (SNL) in Albuquerque, New Mexico [1, 10, 11]. The Z Machine is the most powerful laboratory radiation source in the world. It is a pulsed power device that accumulates large amounts of energy over long timescales (minutes) and then discharges the energy over short timescales (nanoseconds) to generate large amounts of power. In the MagLIF scheme, a preheating laser beam is used. At the Z facility, the preheating laser, called the Z-Beamlet Laser (ZBL), is the same as one of the 192 laser beams used on the NIF, demonstrating one of many instances of ICF collaboration across facilities.

The MagLIF concept can be described by the three-stage process illustrated in Fig. 1.1. A

MagLIF target consists of a cylindrical metal tube (or "liner") surrounded by vacuum and filled with fusion fuel (e.g., pressurized deuterium or deuterium-tritium gas). During the first stage of MagLIF, the entire target (including both the liner and the fuel) is premagnetized with an axial magnetic field. This is done to thermally insulate the hot fuel from the cold liner wall during the implosion. Premagnetization also traps charged fusion products in the fuel during peak compression, so the charged products deposit their kinetic energy back into the fuel for self-heating (e.g., self-heating from α particles created from the deuterium-tritium fusion events). Note that the axial field is amplified via magnetic flux compression during the implosion phase. This amplification allows the field to thermally insulate the fuel even as the fuel becomes increasingly hotter and the radial extent of the fuel becomes increasingly smaller.

During the laser preheating stage of MagLIF (which occurs just as the fuel begins to implode), a few nanosecond, multi-kilojoule laser pulse deposits energy into the pressurized fuel held inside the target, as shown in the center image of Fig. 1.1. This laser pulse raises the fuel temperature to $\sim$100 eV. Then, during the compression stage, the Z facility's current pulse, which rises from 0 to approximately 20 MA in 100 ns, flows axially along the liner's outermost surfaces. This generates an azimuthal magnetic field that surrounds the liner and a corresponding intense magnetic pressure that drives the liner radially inwards. The imploding liner does adiabatic "PdV" work on the hot, magnetized fuel. This both compresses and further heats the fuel to fusion relevant temperatures ($>$2 keV) and densities ($>$0.2 g/cm^3) [1, 3].

In initial MagLIF experiments [1], there was a lack of laser preheating energy coupled into the fuel. Increasing the energy of the preheated fuel can lead to higher fusion yields, and is critical to understanding MagLIF performance scaling. The dependence of fusion yield on laser preheat energy coupling is shown in Fig. 1.2 [2]. Here, the experimental deuterium-deuterium (DD) neutron yields, shown with the orange lines, were measured to be 5×10^{11}, 1×10^{12}, and 2×10^{12} neutrons. The laser energy used in these experiments was 2 kJ. Using the semi-analytic model of MagLIF [4], the DD neutron yield expected would have been 2.5×10^{13} if all 2 kJ of the laser energy was absorbed (shown by the navy lines). The measured neutron yields (5×10^{11}, 1×10^{12}, 2×10^{12})

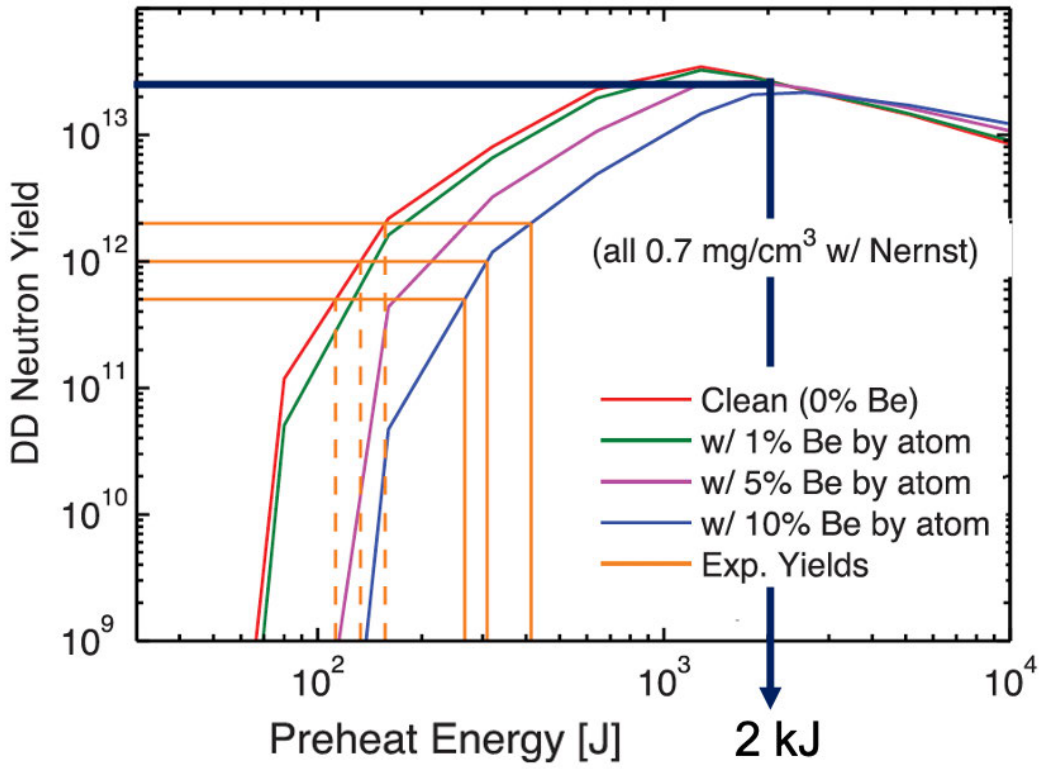

Figure 1.2: The absorbed preheating laser energy is linked to the deuterium-deuterium (DD) neutron fusion yield. If all 2 kJ of laser preheating energy are absorbed, the yield is expected to be 2.5×10^{13}. Instead, the yield was measured to be between 5×10^{11} and 2×10^{12} (shown in orange). These measured neutron yields indicate that between 100-400 J of energy were absorbed. Increasing the absorption of preheating energy would increase the DD neutron yield. Figure from R.D. McBride *et al.* Physics of Plasmas **23**, 012705 (2016) [2].

correspond to an absorbed energy of 100-400 J (an order of magnitude less than the available laser energy). This demonstrates a potential for improvement in yield by increasing preheat laser energy coupling. Such improvements could push the MagLIF platform with its present preheat laser system closer to the goal of scientific breakeven on today's Z facility (and potentially to high-yield fusion ignition on a future facility).

Two specific MagLIF target components are the focus of study in this dissertation. The first feature is the laser entrance hole (LEH) window, discussed in Chapter 3 and in Ref. [12], and the second is the target wall (or liner), discussed in Chapter 4. Both of these target components play an important role in the laser preheating stage of MagLIF.

The laser entrance hole (LEH) is covered by a thin (few-micron-thick) window which is used to

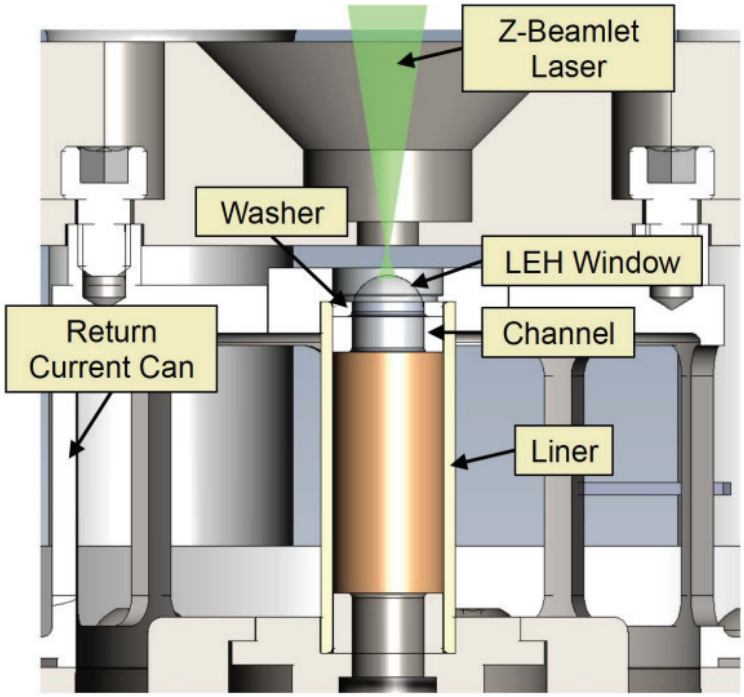

Figure 1.3: An illustration of the MagLIF target chamber area showing the preheating laser (Z-Beamlet) illuminating the LEH window from above the fuel-containing liner target. The Z-beamlet Laser enters the target through the laser entrance hole (LEH) window that is held in place by the washer. The laser then passes through the channel (a pressurized section of the target that does not implode and does not contribute to yield) and then into the main target body surrounded by the metallic liner.

hold the pressurized fuel in place (see Fig. 1.3). This window is nominally transparent; however, the high intensity laser causes the window material to ablate (off of the window and into the fuel) and ionize, which leads to laser-plasma instabilities (LPI). Energy coupling losses from the preheating laser to the fuel are believed to occur because of LPI, energy absorption into the window material, and from window material mixing into the fuel (which leads to enhanced radiation loss) [11, 13–17]. To reduce these losses, the LEH window could be removed before the preheating laser passes through the LEH. This concept of early-time window removal is referred to as "Laser Gate" [10].

There are presently two implementations of the Laser Gate window removal method being investigated. One implementation [10], which is being tested at SNL [18, 19], uses an auxiliary laser pulse to remove the window early in time. This auxiliary beam has a six-pronged spatial profile resembling the shape of an asterisk. When this auxiliary pulse is applied to the LEH window, the

window material is weakened/broken in the shape of the beam's spatial profile, which allows the pressurized fuel to push the window open like a flower opening with six petals. The subsequent preheating laser pulse (Z-Beamlet) is then free to enter the fuel region without interacting with these blown-open window petals [19].

Another implementation of Laser Gate has now been tested at the University of Michigan (UM) and is the subject of this dissertation. This implementation uses a current pulse to heat a wire wrapped around the perimeter of the LEH window (see Fig. 1.4). The heated wire melts/weakens the window material that the wire is in contact with, thus cutting/breaking the window attachment to the target in a controlled fashion. This then allows the pressurized fuel to push the window open away from the target and out of the laser path. The subsequent preheating laser pulse (Z-Beamlet) would be timed to enter the LEH after the window has fully opened and is no longer an obstruction. Fig. 1.4 shows the wire is in contact with only about half of the LEH window perimeter. This allows the window opening direction to be controlled by creating a hinge for the window to open along. Ideally, the window material would stay hinged to the target so that the window is not free to move about and potentially interfere with the preheating laser or other equipment. When integrated with MagLIF experiments, this pulsed-power implementation of Laser Gate should lead to reduced LPI, reduced energy losses due to absorption in the window material, and reduced radiative losses due to fuel-window mix.

Besides MagLIF, the Laser Gate concept could, in principle, be applied to other ICF programs as well. For example, Laser Gate could be used to remove the LEH windows from the hohlraums that surround the ICF targets on the National Ignition Facility (NIF) [20, 21]. The LEH windows and gas-fill densities used for the NIF hohlraums are fairly similar to those used for MagLIF targets. However, a more detailed cost-benefit analysis would be required to assess whether or not Laser Gate on the NIF would be useful and practical.

In addition to LEH window material mixing with and contaminating the fuel, there is also a concern that laser-ablated wall material could mix into the fuel. In a MagLIF target, the liner (or wall) is a thin metallic tube that holds the pressurized fusion fuel in place (see Fig. 1.3). During

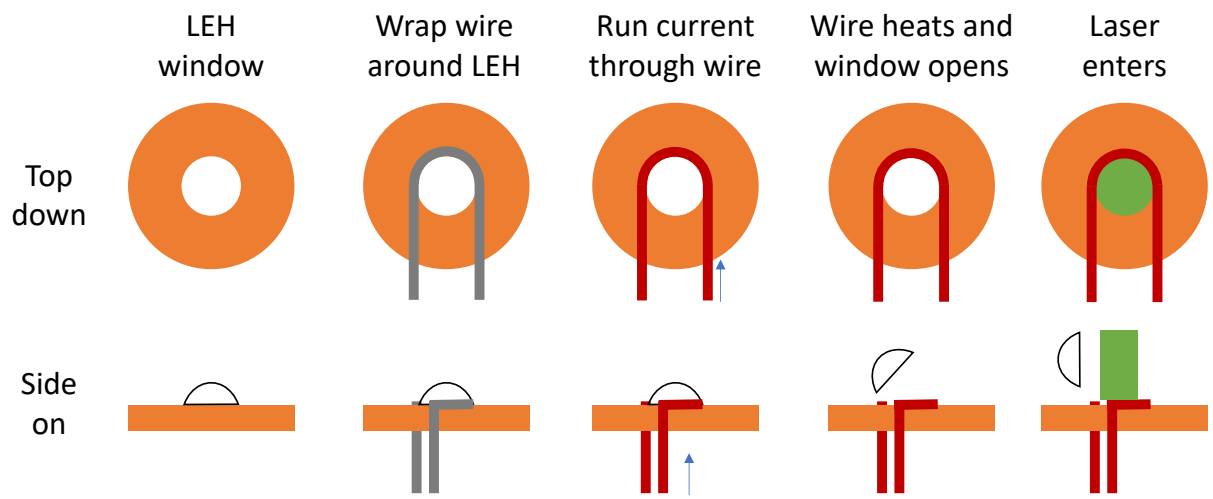

Figure 1.4: Pulsed-power implementation of the Laser Gate concept, where electrical current is driven through a wire to remove the LEH window from the preheating laser path. A thin nichrome wire is wrapped around the window perimeter. Current is driven through the wire to heat and break the window material at the perimeter. The pressure from the target pushes the window out of the way of the incoming laser. Both top-down and side-on views are presented.

the laser preheating stage of MagLIF, shock waves from the laser heating of the fuel interact with the liner. Additionally, the liner is compressed by the magnetic pressure of the Z machine during the final (implosion) stage of MagLIF, which heats the fuel to fusion relevant temperatures and densities [1]. The liner plays a vital role in the MagLIF concept. Ablated wall material mixing with the fuel–and liner implosion non-uniformities–can lead to a decrease in fusion yield.

The yield loss from the mixing of ablated wall material into the fuel occurs as the laser enters the gas filled target and the gas heats to a plasma creating the shock waves. The shock waves bounce off the inner surface of the liner and can cause material to eject from the wall and mix with the fuel. Also, there are potential loses associated with non-uniform wall movement that could seed larger perturbations as the liner compresses during the final stage of MagLIF. As part of this dissertation research, a radiography platform was developed to understand this wall movement and mix as a function of time and position.

MagLIF liner movement and mix is an important area of study. Presently, a platform to study mix in MagLIF is being developed for the National Ignition Facility (NIF) [22]. By contrast, the liner movement and mix platform utilized for this dissertation was developed for the OMEGA

laser facility at the Laboratory for Laser Energetics (LLE). The OMEGA 60 facility was used for a preliminary campaign and the OMEGA EP facility was used for the primary experimental campaign. In these OMEGA liner experiments, a primary (heating) laser enters the cylindrical target along its cylindrical axis. This laser generates shock waves in the fuel, which propagate radially outward and get transmitted into the liner wall. A secondary laser is used to generate x-rays for taking radiographic images of the shock wave propagation.

The development of this platform will help us understand the dynamics of wall movement and mixing. Additionally, the data acquired can help benchmark codes used to design integrated MagLIF experiments on the Z machine. This dissertation includes pertinent theory for the laser preheating stage of MagLIF (Chapter 2), the design and testing of a Laser Gate proof-of-concept experiment [12] (Chapter 3), the OMEGA wall movement experiments (Chapter 4), and conclusions and recommendations for future research (Chapter 5).

CHAPTER 2

Laser Preheating Stage Theory

This chapter covers the relevant theory governing the laser preheating stage of Magnetized Liner Inertial Fusion (MagLIF). In the preheating stage of MagLIF, a laser beam enters a pressurized target through a thin window known as the Laser Entrance Hole (LEH) window. This work aims to remove the LEH window, so the opening dynamics of the window material are discussed. Then the laser deposits energy into the fuel, launching shock waves. Both the energy deposition and shock wave processes are discussed.

2.1 Window Opening Dynamics

A MagLIF target includes a few-micron-thick window that holds the pressurized fusion fuel inside the target, and is where the preheating laser enters the target. In the Laser Gate concept, this window, referred to as the LEH window, is removed from the MagLIF target body. In the version of the Laser Gate concept studied here, the window is opened by wrapping a nichrome wire around the perimeter of the LEH window and pulsing current through this wire. When the highly resistive wire heats up, it weakens the edge of the LEH window allowing the pressurized fuel to open the window up and away from the target, as shown in Fig. 1.4.

To determine if this Laser Gate concept could be a practical addition to the MagLIF platform, analytic estimates were calculated to compare the opening time of the LEH window to the time it would take for the fusion fuel (gas) to evacuate the target. To be a valid concept for the MagLIF platform, there must still be fusion fuel in the target when the window is out of the laser path. So, the window opening time must be much less than the fuel evacuation time. For this analysis, the

LEH window is assumed to be a rigid disk that hinges about one point on its perimeter, as shown in Fig. 2.1.

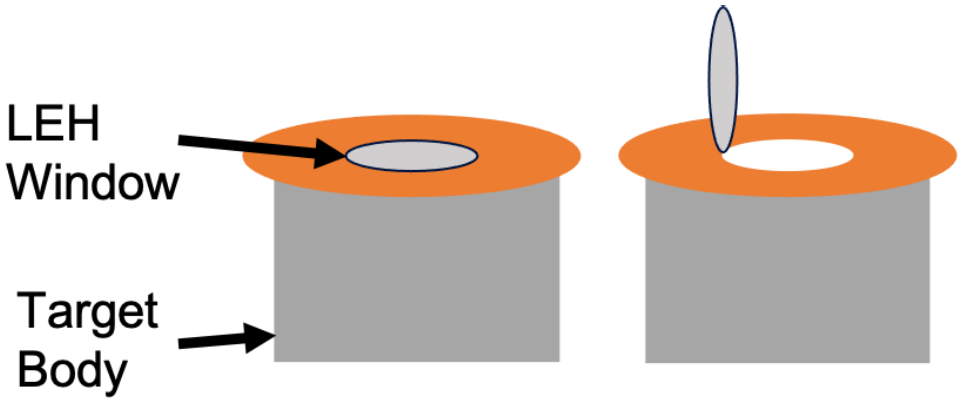

Figure 2.1: To calculate the window opening time, the window was assumed to be a rigid disk rotating about one point on the perimeter of the window. The LEH window begins closed (left) and is considered open when it rotates a full 90° (right). Additionally, the pressure inside the target is approximated to be constant.

To derive the time for the window to rotate about this hinge point, from 0 to 90°, we start with the equation for angular acceleration $\theta = \omega t_0 + \alpha t^2/2$. Here, θ is the $\pi/2$ radians (or 90°) that the window has moved to be considered opened, ω is the angular velocity, $t_0 = 0$ is the initial time, α is the rotational acceleration, and t is the opening time referred to as t_{open}. Additionally, torque can be shown as $\tau = I\alpha$ where I is the inertia, and α is the rotational acceleration. All of this combined gives an opening time of

$$t_{\text{open}} = \left(\frac{\pi I}{\tau}\right)^{1/2}. \tag{2.1}$$

The torque, exerted on the window from the pressure of the internal fuel can be derived starting from $d\tau = dF \cdot y$ and assuming constant pressure to give $d\tau = P \cdot dA \cdot y$ where F is the force, y is distance from the hinge point, P is the pressure of the fuel, and A is the area of the window. From this, the torque can be expressed as,

$$\tau = \int d\tau = 2P \int_0^{2r} \sqrt{2yr - y^2}\, y\, dy = \pi P r^3. \tag{2.2}$$

Using the same variable definitions, inertia can be calculated from the moment of inertia equation $dI = y^2 dm = \rho_w \cdot \delta \cdot y^2 \cdot dA$ where I is inertia, m is mass, r is the radius of the window, δ is the window thickness, and ρ_w is the window material density. Inertia is defined as

$$I = \int dI = 2\rho_w \delta \int_0^{2r} y^2 \sqrt{2yr - y^2} dy = \frac{5}{4} \pi \rho_w \delta r^4. \tag{2.3}$$

Plugging equations 2.2 and 2.3 into equation 2.1, the window opening time can be expressed in SI units as

$$t_{\text{open}} = \left(\frac{5\pi}{4} \right)^{1/2} \left(\frac{\rho_w \times \delta \times r}{\Delta P} \right)^{1/2}, \tag{2.4}$$

where ΔP is the difference in pressure between the target fuel and the ambient pressure surrounding the target. The pressure difference was assumed to be uniform and constant.

The evacuation time, t_{evac}, was taken to be the amount of time needed for a rarefaction wave, moving at the speed of sound for the gaseous deuterium fuel, to reach the bottom of the target. This is the point where the pressure throughout the entire target has been reduced due to the evacuation of fuel. This evacuation time can be expressed in SI units as

$$t_{\text{evac}} = \left(\frac{L}{c_s} \right) = L \times \left(\frac{M}{\gamma R T} \right)^{1/2}, \tag{2.5}$$

where L is the length of the target body, c_s is the sound speed, M is the molar mass of the fuel (gas), γ is the adiabatic constant of the fuel (gas), R is the universal gas constant, and T is the temperature of the fuel (gas). Both fill gases (air for the UM Laser Gate targets and deuterium for the SNL MagLIF experiments) were taken to be diatomic, so $\gamma = 1.4$ was used. Additionally, the fuel temperature was set to room temperature.

As shown in Fig. 1.3 present MagLIF target designs include a laser entrance channel. This channel is a preexisting target component that is full of fusion fuel but is not part of the target's imploding region. This component could be optimized such that the target fuel in the imploding region is still present when the preheating laser enters. This would be done by making the channel length equal to the distance the rarefaction wave moves into the target during the time it takes the

Table 2.1: MagLIF LEH opening time target parameters. The timescales and optimal length were calculated using Eqs. 2.4, 2.5, and 2.6 .

Target Parameters	MagLIF Target
Gas Type	Deuterium
Window Thickness (μm)	1.6
Window Radius (mm)	1.1
Pressure Difference (atm/psi)	8/120
Window Material	Polyimide
Window Density (g/cm^3)	1.42
Sound Speed (m/s)	924
Target Length (mm)	12
Opening Time, $t_{\rm open}$ (μs)	3.4
Evacuation Time, $t_{\rm evac}$ (μs)	13.0
Ratio $t_{\rm open}/t_{\rm evac}$	0.26
Optimal Channel Length (mm)	3.1

window to open. This optimal channel length can be calculated by multiplying the window opening time by the sound speed which simplifies to

$$L_{\rm opt} = L \times \frac{t_{\rm open}}{t_{\rm evac}}. \tag{2.6}$$

To integrate this implementation of Laser Gate into MagLIF, the optimal length, $L_{\rm opt}$, for the laser entrance channel would need to be 3.1 mm (see Table 2.1) to mitigate the fuel lost during the window opening. This way, the gas in the imploding region of the target would still be at its original density when the window is fully open. All of the relevant parameters are shown in Table 2.1.

This analysis is also used later, in Table 3.1, to calculate and compare the opening and evacuation times for both the MagLIF targets and the surrogate targets studied at the University of Michigan.

Finally, it is important to note that $t_{\rm open}$ and $t_{\rm evac}$ have the same temperature dependence (see Eqs. 2.4, and 2.5). Thus, the ratio $t_{\rm open}/t_{\rm evac}$ is not a function of temperature. This means that Laser Gate could be implemented on a cryogenically cooled MagLIF target, which is important for future high-gain MagLIF designs [23, 24].

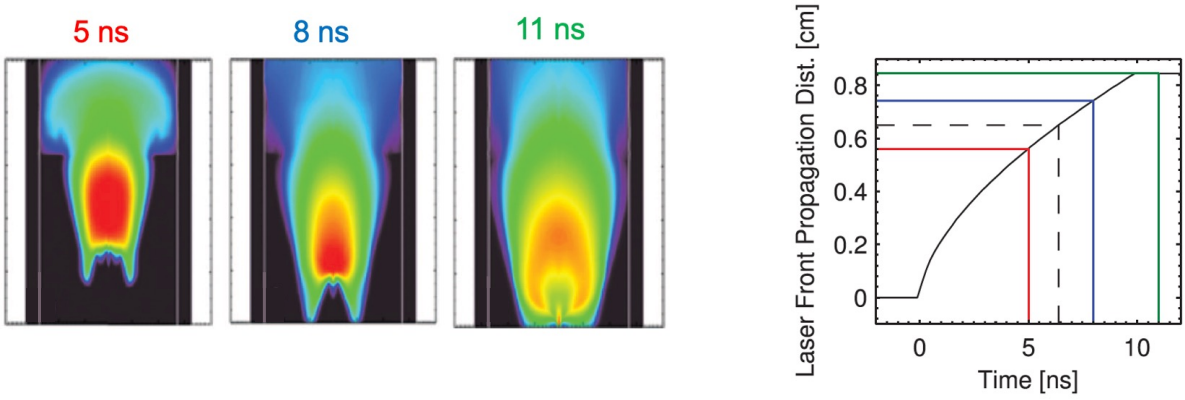

Figure 2.2: The bleaching wave shown at three different time intervals as the laser deposits energy into the fuel. The three images on the left are side-on views of the target, taken from S. A. Slutz et al., Physics of Plasmas **17**, 056303 (2010) [3]. The times of the bleaching wave simulations, shown on the left, correspond to the three times shown in the plot on the right taken from R.D. McBride and S.A. Slutz, Physics of Plasmas **22**, 052708 (2015) [4] .

2.2 Laser Energy Deposition into Gas Target

As the preheating laser enters the gas filled target from above, it deposits energy into the fuel as it interacts with the gas. This energy deposition behaves as a "bleaching wave" as shown in Fig. 2.2 [2]. A bleaching wave is used to describe the process of the laser energy entering the gas. A medium is considered "bleachable" when the transport proceeds more freely as the temperature increases [25]. In this work, the transport is the laser beam energy transport, and the medium is the pressurized gas of the target. While the laser pulse is passing through (bleaching into) the target, it deposits energy deeper and deeper into the target fuel. Ideally, the amount of energy deposited into the target fuel is maximized and heats the fuel throughout the target without depositing much energy in the beam dump located below the target (see Fig. 1.3).

In Fig. 2.2, the three images on the left (5 ns, 8 ns, and 11 ns) correspond to the colored propagation distance curves plotted in red, blue, and green, respectively, in the plot on the right. As the time from the onset of the laser pulse increases, the laser bleaching front propagates deeper into the target. The propagation distance curve is flat before 0 ns and after 10 ns because in this simulation the laser pulse is only "on" for 10 ns, so when there is no pulse there is no propagation.

The Semi-Analytic MagLIF Model (SAMM) [4] provides an in-depth analysis for laser propagation in a standard MagLIF target design. However, the SAMM model considers a uniform density throughout the target body. To account for laser propagation through a Laser Gate target as the gas undergoes expansion, a SAMM-like code called STEPH (Simulating The Energy of PreHeat) was developed. The STEPH model allows for two separate target densities as the gas escapes from the open Laser Entrance Hole (LEH) window and expands from the target after window removal. When the window is removed, the fuel inside starts to escape at the speed of sound for the fuel material. This can be modeled as a rarefaction wave moving deeper into the target also at the speed of sound. Referring to Fig. 2.3, as the rarefaction wave propagates deeper into the fuel, the density in the region of fuel above the wave front decreases. To consider a range of possible gas expansions into air or a vacuum chamber, two models were used to bookend the density in the expanded region. Referring to Figs. 2.3 and 2.4, if the gas expands straight up in a column-like expansion, the lower density fuel region above the imploding region is half the original density ($\rho = \rho_0/2$). If the gas expands into a dome shape, the lower density region has a density of $\rho = \rho_0/3.7$. In Fig. 2.4, the left cartoon shows the current MagLIF target, the middle shows Laser Gate column expansion, and the right shows Laser Gate dome expansion. The $z = 0$ dashed line represents the beginning of the imploding region. This is important because in the current MagLIF target design, there is a "cushion" region or laser entrance channel (LEC). The cushion region is included in target design for structural stability. Therefore, there is some target fuel that does not implode; only the fuel in the liner/implosion region implodes and contributes to fusion yield. This cushion region can be exploited in a Laser Gate target. The cushion region can be lengthened such that the rarefacton wave arrives at the interface between the cushion region and the imploding region at the time when the laser pulse is fired into the target, ensuring that the implosion region includes all original density fuel (ρ_0).

For the STEPH model, the density interface is at the distance into the target that the rarefaction wave, moving at the sound speed, has propagated into the fuel over the length of time required for the window to open, as calculated using Eq. 2.4. This location is also set to be the interface between

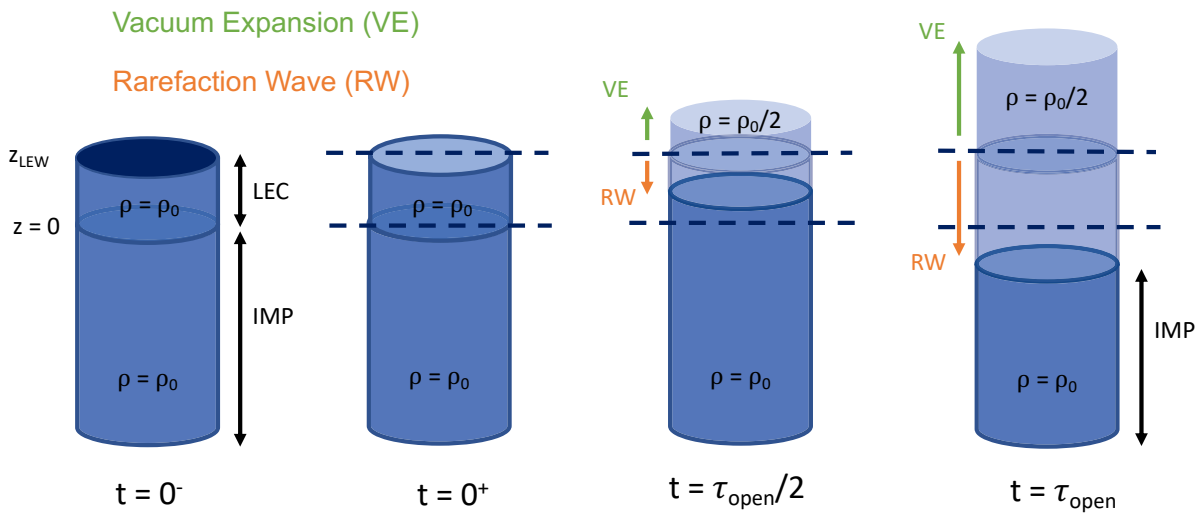

Figure 2.3: Once the LEH window is removed (in the Laser Gate concept) a rarefaction wave moving at the sound speed moves into the target, and the the target fuel begins expanding out of the target into the vacuum chamber. As this expansion occurs, there are two density regions: an original ρ_0 density and a new lower density region that is related to the volume the evacuated fuel occupies. The Laser Gate concept involves syncing the laser entry time to the window opening time (τ_{open}) and increasing the laser entrance channel ("cushion" region above the imploding region) so that the density in the imploding region remains at its original density value at the time of laser entry.

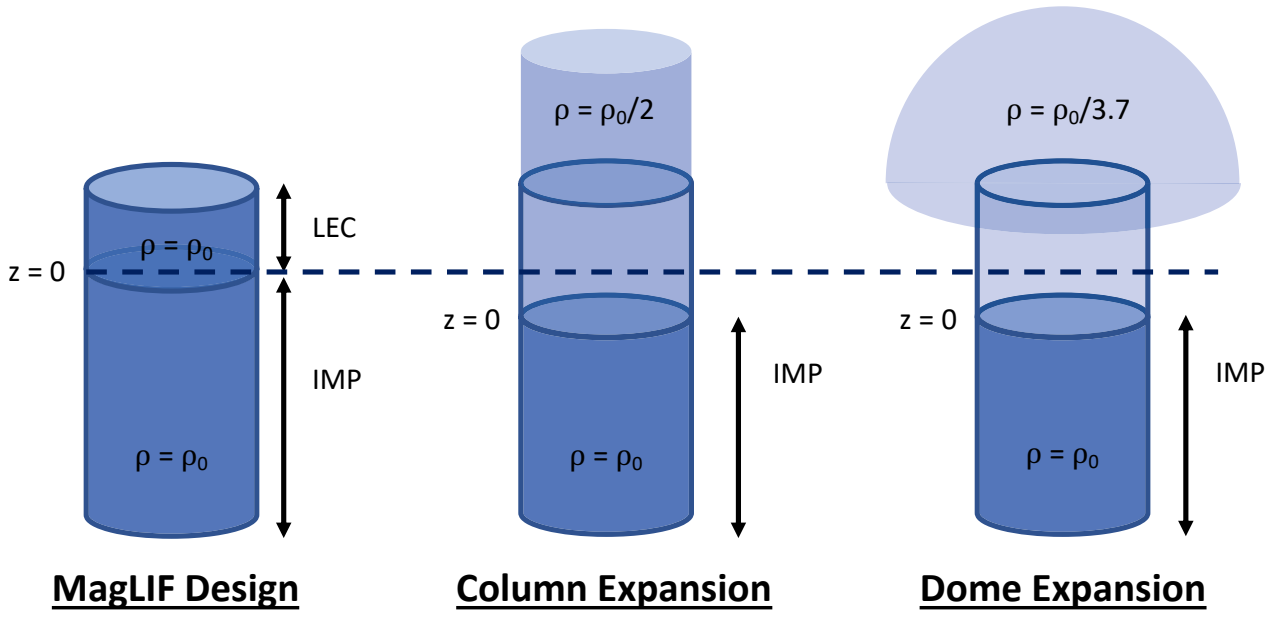

Figure 2.4: As the LEH window is removed and fuel evacuates the target, there become two separate density regions. The different expansion models from STEPH are used to bookend the range of possible expansion: column expansion (middle) and dome expansion (right). The volume occupied by the evacuated gas is what determines the density of the fuel in the expansion region. Note that the start of the unperturbed original density region (also known as the imploding region) is set to be the $z = 0$ region in the STEPH model. Laser Gate targets would implement longer Laser Entrance Channels (LECs).

Table 2.2: Relevant parameters used in the STEPH model to determine laser propagation into different target types and models. The values are similar to those used for current MagLIF designs and for original SAMM models.

Target Parameters	MagLIF Target
Laser Beam Radius (r_b)	1 mm
Laser Beam Energy (E_{laser})	8 kJ
Pulse Length (t_{laser})	10 ns
Laser Beam Wavelength (λ_b)	532 nm
Fuel Density (ρ_{fuel})	3.024 $\mathrm{kg/m^3}$
Window Density (ρ_w)	1420 $\mathrm{kg/m^3}$
Window Thickness (δ_w)	1.6 μs
Laser Beam Power (E_{laser}/t_{laser})	800 GW

the LEC and the imploding region. While the laser heating is being applied in this model (which is over a short time period relative to the time scale of the rarefaction wave), the densities in the perturbed and unperturbed regions and the location of the boundary between the two regions are all held constant. Table 2.2 shows the relevant parameters used for the STEPH model. The target parameters (fuel density, window density, and window thickness) could be easily experimentally modified to validate the STEPH code. However, the following parameters are similar to those in present MagLIF experimental designs.

Following Ref. [4], the propagation distance into the target is found starting from the heating of the fuel by the laser light with an associated absorption described as,

$$\frac{d\epsilon_b}{dt} = \frac{dI_b}{dz} = -\tilde{\kappa}(t_{ph}) \cdot \epsilon_b^{-3/2}(z,t) \cdot I_b(z,t), \tag{2.7}$$

where ϵ_b is energy density, I is laser intensity, and $\tilde{\kappa}(t_{ph})$ is the absorption coefficient. This equation has the exact solutions

$$\epsilon_b(z,t) = \epsilon_b(z_{LEH},t)\left(1 - \frac{z_{LEH}-z}{z_{LEH}-z_f(t)}\right)^{2/3}, \tag{2.8}$$

$$I_b(z,t) = I_b(z_{LEH},t)\left(1 - \frac{z_{LEH}-z}{z_{LEH}-z_f(t)}\right)^{2/3}, \tag{2.9}$$

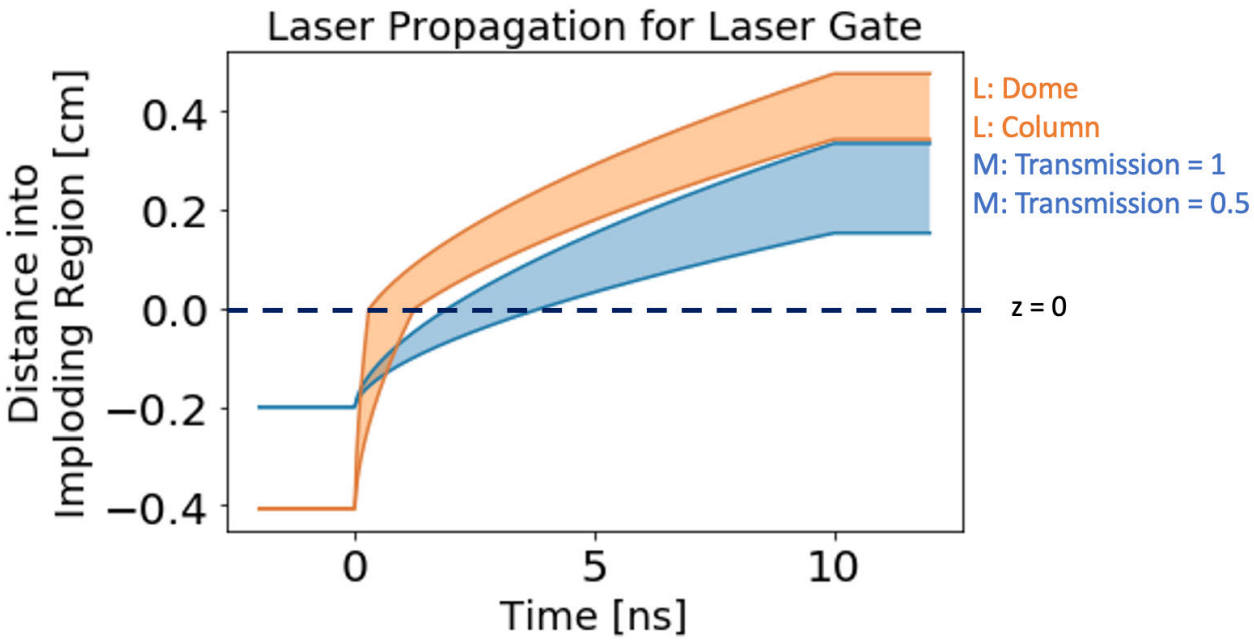

Figure 2.5: Laser propagation distances into the target bodies are shown. The orange curves represent the two density region Laser Gate models for dome and column expansion. The blue curves represent the current MagLIF experiment with laser energy transmission through the window material of 50 and 100%. The true expansion for both the Laser Gate and current MagLIF scenarios are likely in their respective shaded regions. The STEPH model proposes potential better laser propagation that could possibly be measured in an integrated Laser Gate experiment.

where

$$\epsilon_b(z_{LEH}, t) = \left(\frac{5}{2} \cdot \tilde{\kappa}(t_{ph}) \cdot I_b(z_{LEH}, t) \cdot (t - t_{ph})\right), \tag{2.10}$$

$$z_f(t) = z_{LEH} - \frac{5}{3}\frac{I_b(z_{LEH}, t)}{\epsilon_b(z_{LEH}, t)}(t - t_{ph}). \tag{2.11}$$

Using the STEPH model, the propagation is calculated twice: first in the low density region and then in the unperturbed density region. The values at the end (bottom) of the low density region are calculated and used as inputs for the start (top) of the unperturbed region. Additionally, the propagation is calculated once for the standard MagLIF case with uniform density. Figure 2.5 shows the results of the STEPH analysis comparing laser propagation in both bookended Laser Gate expansion models (column and dome) and two standard MagLIF cases where the transmission through the LEH window is 100% and 50%. This shows that the laser propagates deeper into the imploding region of a Laser Gate type target. The penetration depth can be measured and is a

good tool to assess the performance of MagLIF targets and the surrogacy of Laser Gate targets. In Fig. 2.5, the orange curves correspond to Laser Gate scenarios and the blue curves correspond to present MagLIF scenarios. The Laser Gate curves start at a more negative distance because the laser must pass through a longer distance of target material to reach the imploding region of $z = 0$. However, as shown in the figure, the laser front moves through the non imploding Laser Gate region quicker because the density is lower. The true gas expansion from the target is expected to be somewhere in between column and dome expansion, making the propagation curve somewhere in the orange shaded region. The blue curves show two types of present MagLIF targets. The upper curve assumes no energy is lost at the LEH window interface. We know this to be untrue. Originally the energy loss was about 50%, but as improvements have been made to the laser pulse shaping, it is estimated that about 80% of the energy makes it through the LEH window. The STEPH model uses a SAMM-like analysis to show an expected benefit to implementing a Laser Gate system onto the present MagLIF platform design.

However, the STEPH model only treats the gas expansion as two separate and constant density regions. There might be more of a density gradient present in the escaping gas column. More indepth analysis could be modeled to show a density gradient. However, the STEPH model was designed to be a simple model of the laser energy absorption in the Laser Gate version of MagLIF. The laser propagates faster in the less dense region of the STEPH model. If a density gradient (instead of two constant density regions) was included the propagation speed would increase in the lower density parts of the gradient, and decrease in the higher density parts of the gradient. This propagation time could be compared to the STEPH model.

In both the present and Laser Gate versions of MagLIF, Laser Plasma Instabilities (LPI) occur as a high energy laser interacts with material. These instabilities can cause energy loss from the laser beam as well as introduce mix of target material into the fuel causing asymmetries which lead to lower fusion yields as the hotspot undergoes less and asymmetric compression. The types of LPI that contribute to losses likely include [26] stimulated brillouin scattering (SBS) [27, 28], stimulated raman scattering (SRS) [29], two-plasmon decay (TPD) [30], and filamentation [28]. SRS and SBS

affect the coupling and mix, TPD affects the mix, and filamentaion affects the mix, and can act to increase SRS and SBS. In the present MagLIF design the material the laser interacts with is the LEH window material and the initial gas density. In the Laser Gate design, the laser interacts with a lower density region and a smoother density gradient at the beginning of its interaction with the target. This difference in the material and the density gradient the laser interacts with could impact the LPI that occurs.

While the implementation of a Laser Gate window opening scheme might prove to be a laborious and complex endeavor, there would be benefits to laser energy propagation that might allow present MagLIF experiments to scale to higher yield through higher laser energy coupling with the Laser Gate concept.

2.3 Wall Shocks and Liner Movement using HYDRA

During the laser preheating stage of MagLIF, the laser enters a cylindrical gas filled target, interacts with the fuel, and shock waves are created. These shock waves move radially outward toward the target wall or "liner". As shocks move through the wall material, the wall experiences a compression and then spreads out. Additionally, this process can leave low density wall material available to mix in with the fusion fuel. This process is important to understand because wall material mixing into the fuel could ultimately degrade fusion yield in an integrated MagLIF experiment. Also, tracking this wall movement can help understand wall movement dynamics and validate codes used in experimental design.

HYDRA [31] is a parallel arbitrary Lagrangian-Eulerian (ALE) 2D or 3D radiation magnetohydrodymanics (RMHD) code used consistently for designing experiments on the National Ignition Facility (NIF) and at the Z machine [32]. It has also been used in design of other MagLIF preheating experiments at other facilities such as Omega EP [33,34]. HYDRA is commonly used because of the code's parallelism, thread based load balancing capabilities, and many included physics packages that make it relevant for High Energy Density Physics (HEDP) applications [35]. The packages include magnetic fields, radiation, atomic physics, hydrodynamics, and many more. In addition to its

Table 2.3: Target and preheating laser parameters used as inputs for the 2D HYDRA simulations presented in this dissertation. These are similar to MagLIF scales and the Omega EP facility capabilities.

Target Parameters	Value
Target Length	10 mm
Target ID	4.65 mm
Target OD	4.85 mm
Liner Material	Parylene-N
Liner Density	1.01 g/cc
Fuel Pressure	141.16 PSIA
Laser Energy	3327.7 J

physics capabilities, HYDRA has also been studied on IBM's Blue Gene/Q to gather performance metrics including memory usage [35]. HYDRA can resolve small features because of its large number of zones, has 100-200 bins for photon energies, and uses a block structured mesh [35]. HYDRA is currently used for a lot of HEDP applications and has been well validated [36].

For this work, 2D HYDRA was used to simulate wall movement as the preheating laser enters the target fuel. All HYDRA simulation data here is courtesy of M. Weis at SNL. For these simulations, the Equation of State (EOS) uses a solid (tension) regime for given ambient conditions. A simulated wall density of 1.01 g/cm^3 was used instead of the standard 1.1 g/cm^3. This 8% difference in density (and ultimately mass) may cause the material to be initially out of tension (have a non-zero pressure), causing the material to tend to expand with no external forcing. However, this 8% difference in density is not expected to cause significant differences. Table 2.3 provides the target and laser parameters used for the simulation data presented in this dissertation. The values are similar to MagLIF target parameters and Omega EP laser capabilities.

Experimental shot times ranging from 10 to 40 ns were chosen from HYDRA predictions. The first experiments were done at 10 ns to attempt to catch the initial shock moving through the wall. The later time of 40 ns was chosen to show substantial outward movement of the outer wall. Also, for these experiments, later times were avoided as the wall begins to interact with the fiducial described in Sec. 4.2.

Figure 2.6 shows the density of the liner wall as a function of time and radial distance from the

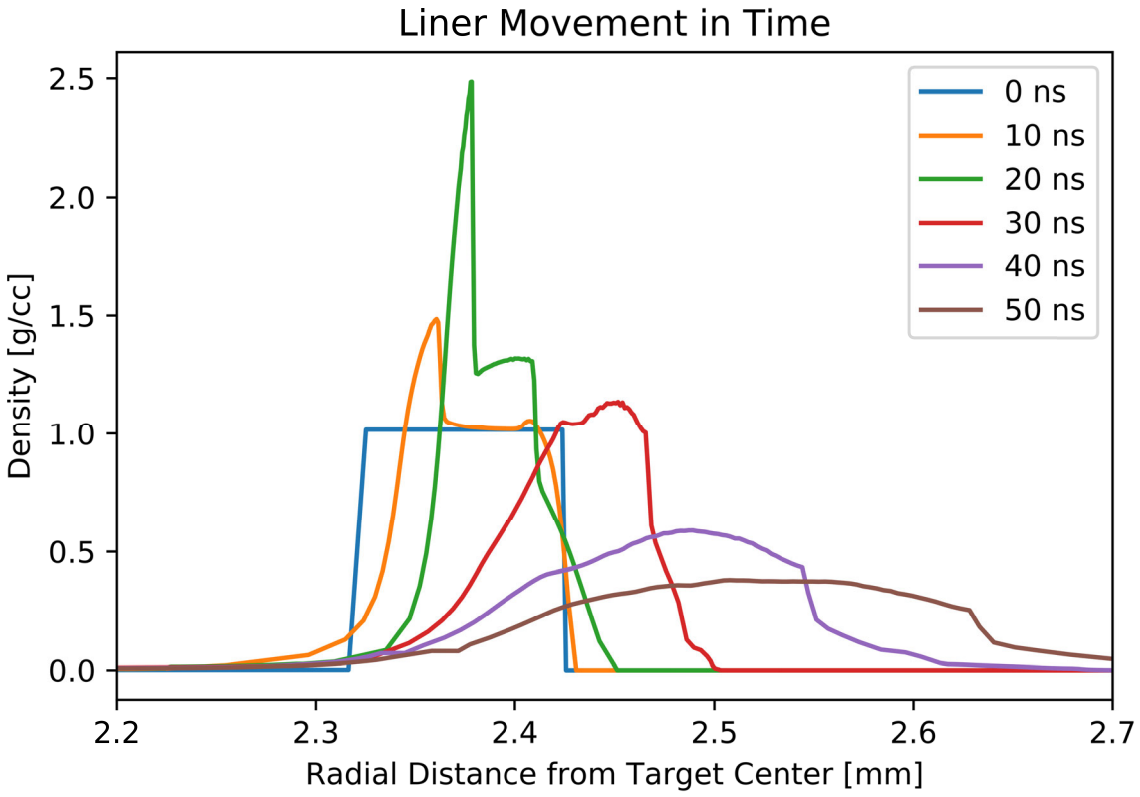

Figure 2.6: A 1.01 g/cc original density liner is simulated using HYDRA. As the shock wave moves radially outward through the target wall, the wall material first compresses and then relaxes (spreads) outward, away from the target axis. Low density tails are seen inside the original inner target radius of 2.325 mm. These low-density tails of wall material could potentially mix with the fusion fuel and degrade the fusion yield.

axis of the cylindrical target. At $t = 0$ ns, the density is uniform throughout the wall, from the inner surface at $r = 2.325$ mm to the outer surface at $r = 2.425$ mm. Then, at $t = 10$ ns, the inner surface of the liner begins to compress. At $t = 20$ ns the shock wave is providing even more compression. Finally, at $t = 30$ ns, and onward, the target liner material spreads out significantly and moves away from the axis of the target. It is important to note that there is a region of low-density wall material that moves radially inward from the original location of the liner's inner surface. If this material mixes with the fuel, then the fusion yield could be reduced.

Figure 2.7 shows more time steps between the 10 and 20 ns times. From the increased time resolution, it is observed that there are actually two shock waves generated. At $t = 10$ ns, an initial

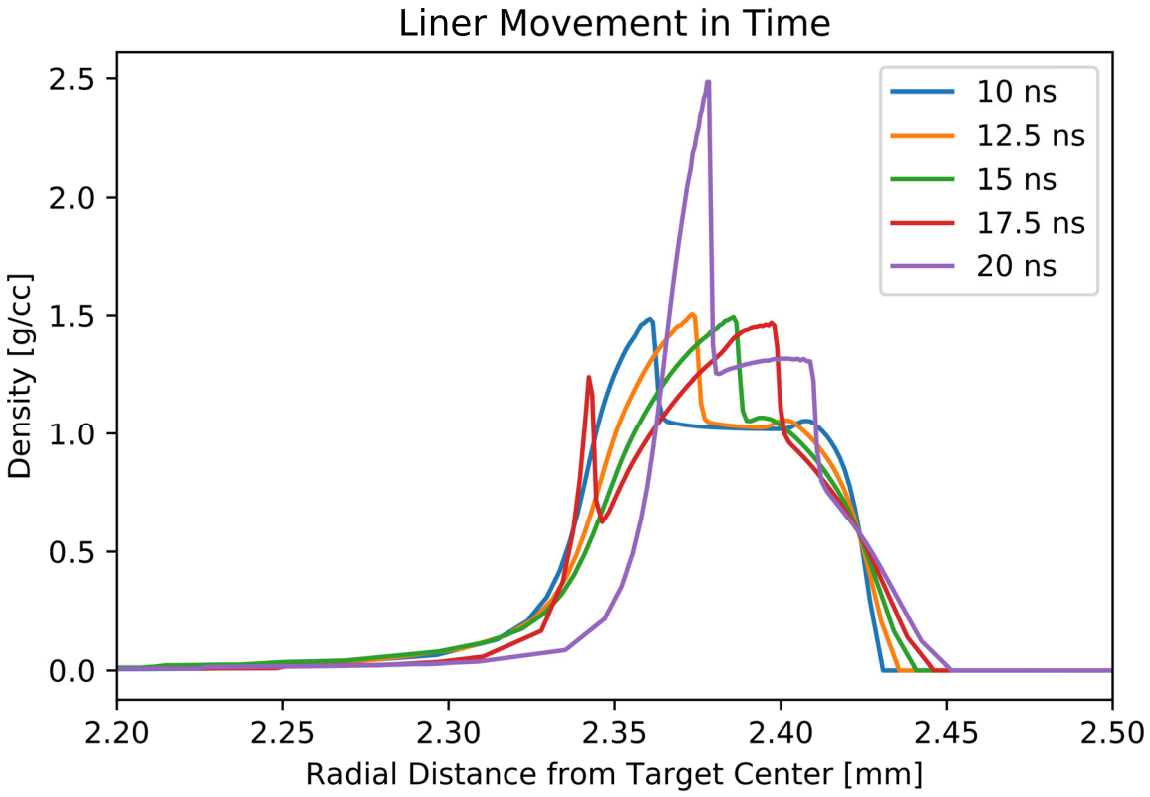

Figure 2.7: Increased time steps are shown between the 10 and 20 ns curves from Fig. 2.6. Before 17.5 ns, a single (first) shock is seen moving through the liner. At 17.5 ns, a second (larger) shock is seen entering the liner wall. This second shock further compresses the liner wall and causes the inner surface to accelerate radially outward.

shock begins to move through the liner, starting at the inner edge, as demonstrated by a compression, or increased density. This initial compression is is thought to be driven by the radiation emitted from the laser-heated fuel. From $t = 10$ ns to $t = 15$ ns, this initial shock penetrates deeper into the target wall and the outer edge of the target wall begins to move slightly. Then, at $t = 17.5$ ns, a second (stronger) shock begins at the liner's inner surface. After this is when the inner radius of the target really begins to move. The increased density in the outer half of the wall at $t = 20$ ns is the first shock wave moving through the target, while the largest peak at $t = 20$ ns is from the second shock wave.

In addition to density profiles, the HYDRA simulations can track the outer edge of the target wall. Figure 2.8 shows the liner movement for a given axial distance from the LEH. Here, $z = 0$ mm

is the location of the LEH and $z = 10$ mm is the end of the 10-mm-long imploding region of the target body.

These simulations show a significant dependence in outer edge wall movement on the axial distance (depth) into the target body. The maximum wall movement comes near the top/beginning of the target length. Additionally, the outer edge of the wall moves only a little during early times and then more so at later times. This corresponds to what can be seen in Fig. 2.6 because the second shock does not reach the outer edge of the liner until about 30 ns. The outer edge of the target moves significantly more from 30 to 40 ns than it did in the first 25 ns.

The liner behavior as it is shocked is important and can be experimentally observed. Both the density profiles and outer edge of the liner have now been measured experimentally as a result of this dissertation work. These measurements are presented in Sec. 4.3.

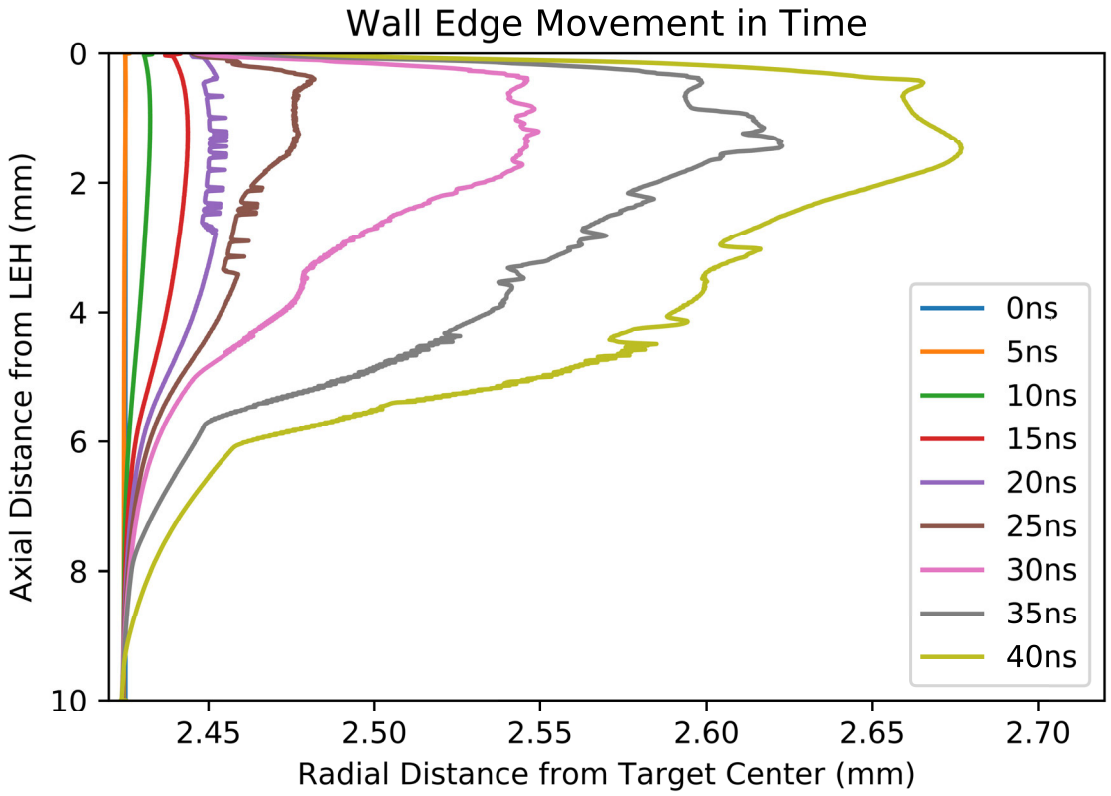

Figure 2.8: The HYDRA simulated location of the outer edge of the liner as a function of time and axial distance from the laser entrance hole (LEH). Here, $z = 0$ mm is the LEH location and $z = 10$ mm is the end of the 10-mm-long implosion region of the target body.

CHAPTER 3

Laser Gate for Energy Coupling

This chapter covers the setup and results of the Laser Gate experimental work to improve energy coupling in the laser preheating stage of MagLIF.

3.1 Experimental Design

3.1.1 Target Fabrication

The targets for these studies were designed and fabricated at the University of Michigan (UM) (see Fig. 3.1). Their dimensions were chosen to be similar to the dimensions of the MagLIF targets tested on the Z facility at SNL, while being slightly larger to allow for easier target assembly. The comparisons between the UM and SNL target types are shown in Table 3.1. The UM target bodies were all 25 mm tall. They were made from transparent acrylic tubing to allow visible diagnostic access to the gas dynamics occurring inside the targets. The tubing was chosen to be square in cross section (flat on the sides) to better enable side-on laser probing techniques (e.g., side-on bright-field schlieren/shadowgraphy imaging). Note that the work presented here does not include a study of the internal gas dynamics, but these targets were designed to enable such experiments in the future.

Each target body (each transparent acrylic tube) was capped on the top with an LEH and on the bottom with another piece of acrylic to hold the gas fill tube in place. The LEH was made from an orange polyimide washer. The washer was 0.15 mm thick, with an inner diameter of 5.16 mm and an outer diameter of 15.9 mm. The LEH window was made from 3-μm-thick Mylar. The targets were assembled using glue that was cured by ultraviolet light. A nichrome wire (80% Ni, 20% Cr)

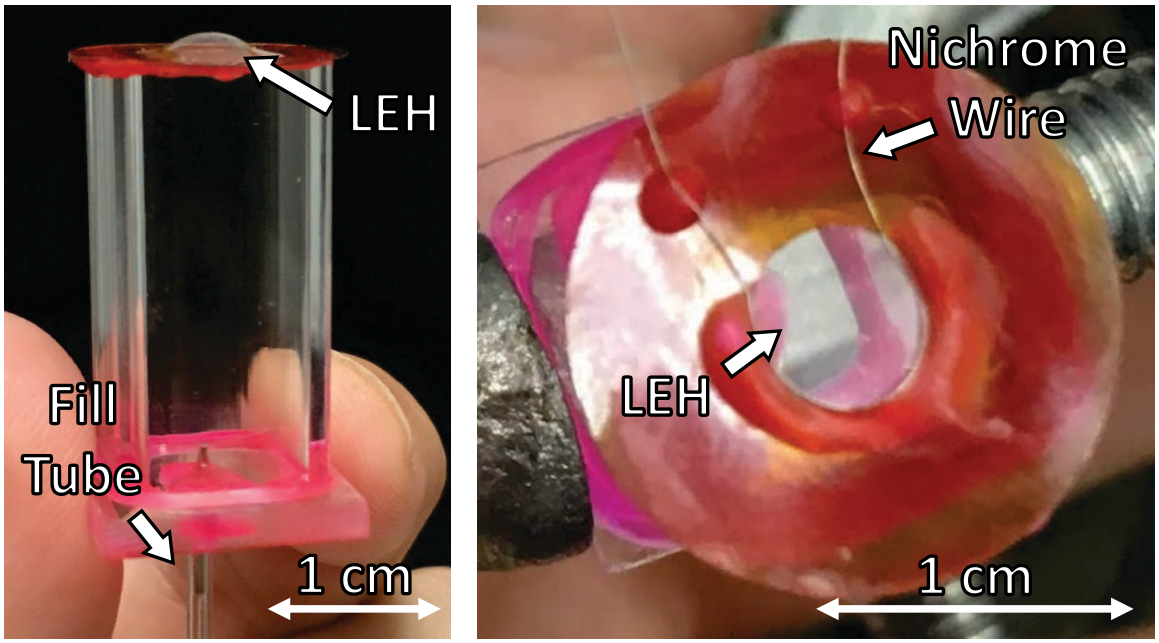

Figure 3.1: UM target for testing Laser Gate. When pressurized, the window material stretches out into the domed shape shown on the left. Shown on the right is the nichrome wire attached to about half of the LEH perimeter.

Table 3.1: Comparison of UM and SNL target parameters. The timescales were calculated using Eqs. 2.4 and 2.5 from Sec. 2.1.

Target Parameters	Laser-Gate Targets (UM)	MagLIF Targets (SNL)
Gas Type	Air	Deuterium
Window Thickness (μm)	3	1.6
Window Radius (mm)	2.6	1.1
Pressure Difference (atm/psi)	2/30	8/120
Window Material	Mylar	Polyimide
Window Density (g/cm^3)	1.38	1.42
Beveled Washer	No	Yes
Ambient Pressure	Atmosphere	Vacuum
Sound Speed (m/s)	343	924
Target Length (mm)	25	12
Opening Time, t_{open} (μs)	14.3	3.4
Evacuation Time, t_{evac} (μs)	74.1	13.0
Ratio $t_{\mathrm{open}}/t_{\mathrm{evac}}$	0.19	0.26

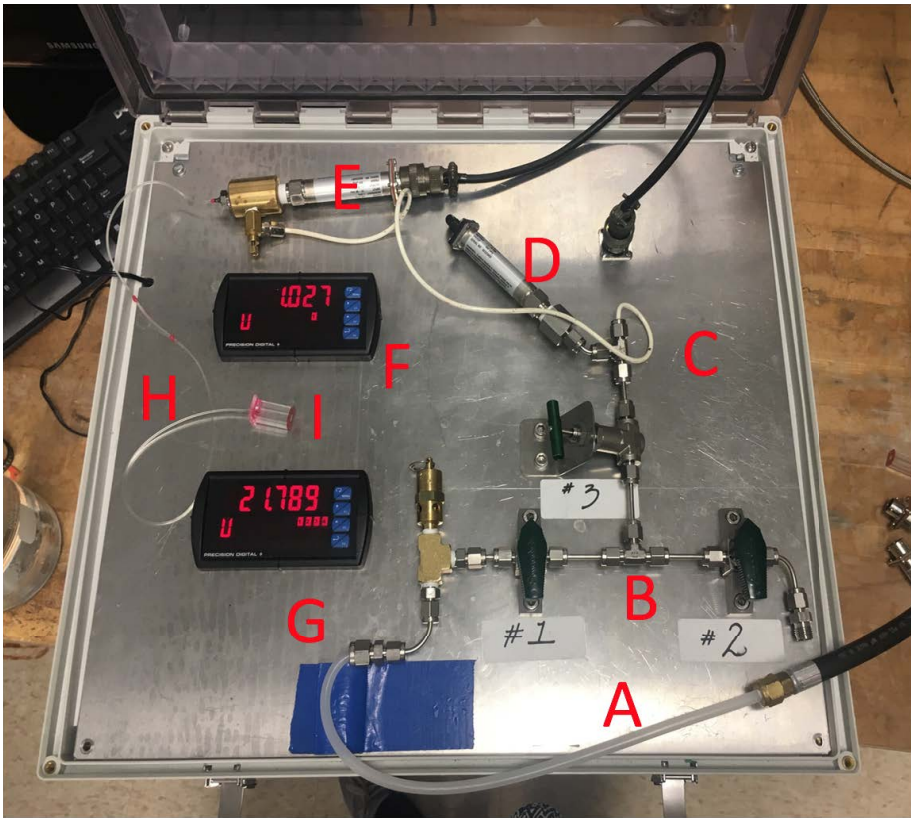

Figure 3.2: Photo of the target gas-fill system. (A) Compressed air inlet. (B) T-connector between the inlet valve (labeled #1), the outlet valve (labeled #2), and the flow control valve (labeled #3). (C) Flow line to target transducer and target. (D) System pressure transducer. (E) Target pressure transducer. (F) System pressure readout. (G) Target pressure readout. (H) Flow line to target. (I) Target.

of 100-μm diameter was glued down to one half of the inner perimeter of the washer (see Fig. 3.1). The LEH window was then glued to the underside of the polyimide washer. When these targets were pressurized, the window material would stretch and form the domed shape shown in Fig. 3.1. When the window material bubbles out, it makes contact with the nichrome wire around the washer.

To pressurize the targets, the gas-fill system shown in Fig. 3.2 was used. The pressure transducer outputs a voltage signal, and a calibration study was done to relate the output voltage to the target pressure in psi. This system is capable of achieving up to 120 psig (8.2 atm). We used air instead of deuterium to fill the targets, because air is readily available and does not require extra safety precautions.

It is important to note that SNL MagLIF experiments are done with the target surrounded by

vacuum, while our UM Laser Gate experiments were done with the target surrounded by atmosphere. The important quantity governing the window opening dynamics is the pressure difference across the window, ΔP. Thus, in this work, the pressures will be stated in terms of ΔP values.

In filling the targets, the goal was to use ΔP values similar to the lower end of the ΔP values used in MagLIF experiments at SNL (approximately 60 psi in Ref. [1]); however, we were only able to reliably achieve ΔP values of about 30 psi (2.0 atm). During our first attempts to pressurize to $\Delta P = 60$ psi, the LEH windows broke consistently. MagLIF targets fabricated at SNL are capable of reaching ΔP values of at least 120 psi (8.2 atm) [37]. The premature breaking of the Mylar windows in the UM targets is thought to be due in part to the value of $(\delta/r)^2$ that was used, where δ is the window thickness and r is the window radius, and in part to the sharp corners on the inside lip of the washers that were used. The pressure a window is capable of holding before bursting is proportional to $(\delta/r)^2$. The $(\delta/r)^2$ for an SNL target is 1.62 times larger than that of the UM targets, so the UM targets should only hold about 60% of the pressure of an SNL target. Additionally, the washers used in the construction of SNL targets are beveled on the edge that the LEH window material stretches around, see Fig. 3.3, thus eliminating the sharp corner. Future UM targets should use beveled washers and smaller LEH window radii to better match SNL's $(\delta/r)^2$ value.

Analytic estimates were calculated to compare the opening time of the LEH window to the time it would take for the fuel (gas) to evacuate the target. A detailed description of window opening dynamics and the governing equations can be found in Sec. 2.1. Ideally, the evacuation time would be much longer than the window opening time, so that most of the fuel would still be inside the target when the window is fully opened and the preheating laser pulse is applied. For the UM targets, $t_{\text{open}} \approx 14.3$ μs, and $t_{\text{evac}} \approx 74.1$ μs. For the SNL targets, $t_{\text{open}} \approx 3.4$ μs, and $t_{\text{evac}} \approx 13.0$ μs. These comparisons and others are summarized in Table 3.1. There are various MagLIF target designs that are fielded on the Z facility, but for the sake of comparison, only one set of design parameters was chosen (a set from a recent study at SNL [16]). For the SNL target chosen, the rarefaction wave will have propagated about one fourth of the way down the target by the time the window is fully open. However, in this sample set of target parameters, the laser entrance channel

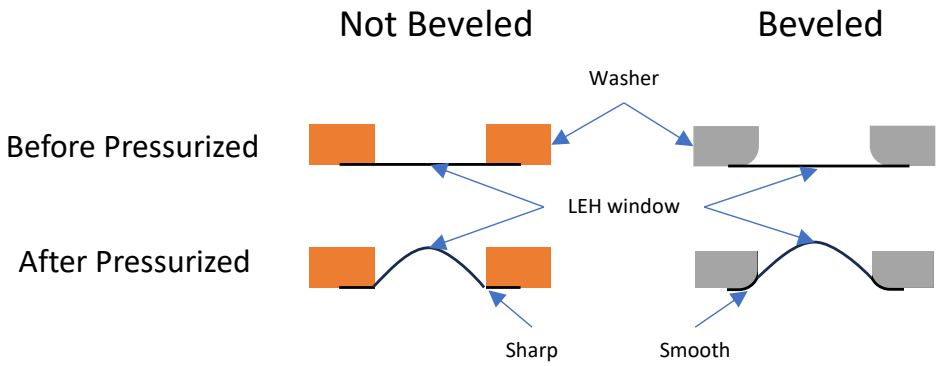

Figure 3.3: A side-on cut away view of the LEH washers showing the difference between a not beveled and a beveled edge washer. Note, these are not drawn to scale, but meant to show the difference between a sharp and smooth edge against the LEH window material. A beveled washer reduces the likelihood the window breaks while pressurizing the target.

is 2 mm in height, while the imploding liner height is 10 mm (see Fig. 1.3). The rarefaction wave propagating at roughly the speed of sound will move about 3 mm into the target during the 3.4 μs opening time. Therefore, the rarefaction wave will have propagated through the 2 mm laser entrance channel and only 1 mm (or about 10%) into the imploding fuel region throughout the opening time. This set of target parameters could be optimized by increasing the length of the laser entrance channel by 1 mm, so that the rarefaction wave arrives at the top of the imploding liner just after the window fully opens. Note, however, that any laser energy deposited in the gas escaping from the laser entrance channel is considered a loss of preheat energy, since this energy does not contribute to preheating the fuel in the imploding region of the target. If the laser entrance channel becomes too long, then this energy loss could become comparable to the energy losses associated with LPI and absorption in the LEH window material. To better understand where this transition occurs, detailed preheating studies are required. These studies would involve both simulations and experiments using the platform described in this paper.

Other possible solutions for reducing the ratio $t_{\rm open}/t_{\rm evac}$ (based on Eqs. 2.4 and 2.5) could involve increasing the gas density or decreasing the window mass (density, radius, or thickness). However, some of these changes (e.g., window thickness) could also weaken the windows and thus

reduce the fuel pressures that the targets/windows could hold. Therefore, care must be taken when evaluating such tradeoffs.

3.1.2 Diagnostic Setup

The experimental facility assembled at UM to test the Laser Gate concept included a small current pulser [38,39], an iPhone 6s video camera, and a 12-frame bright-field laser schlieren/shadowgraphy imaging system (see Fig. 3.4). The pulser was used to drive current through the nichrome wire on the target. This pulser consisted of a 240-nF capacitor (charged to 13 kV), an atmospheric-pressure spark-gap switch, and a 0.83-Ω resistor array. The pulser was charged by a DC power supply capable of generating up to 20 kV. The voltage on the power supply was increased manually until the gas in the spark-gap switch broke down, closing the switch, and allowing electrical current to flow to the target. Preliminary testing showed that the electrical current driven through the nichrome wire was so high that the wire exploded. To reduce the current, an additional resistance of 50–60 Ω was added to the output of the pulser. The wire then remained intact while still being heated enough to melt/weaken the LEH window on the target. A Pearson coil was used to measure the current through the nichrome wire. Depending on the attached output resistor, the measured peak current had a range of 150–170 A. An example current trace is shown in Fig. 3.5.

The iPhone video camera was used to image the window opening dynamics on millisecond timescales. With the slow-motion feature enabled, this camera is capable of recording up to 240 fps (a frame spacing of about 4 ms).

The 12-frame bright-field laser schlieren/shadowgraphy imaging system was used to image the window opening dynamics on microsecond timescales. The imaging system is capable of achieving temporal resolution as low as tens of nanoseconds, which could be useful for imaging future targets/experiments with faster predicted opening timescales. This system used a Coherent Verdi 6-W continuous-wave (CW) laser source with a 532-nm wavelength. A laser-fiber coupler was used to transport the beam from the laser room to the experiment. The optical setup, shown in Fig. 3.4, included an achromat lens to collimate the diverging light rays as they exited the

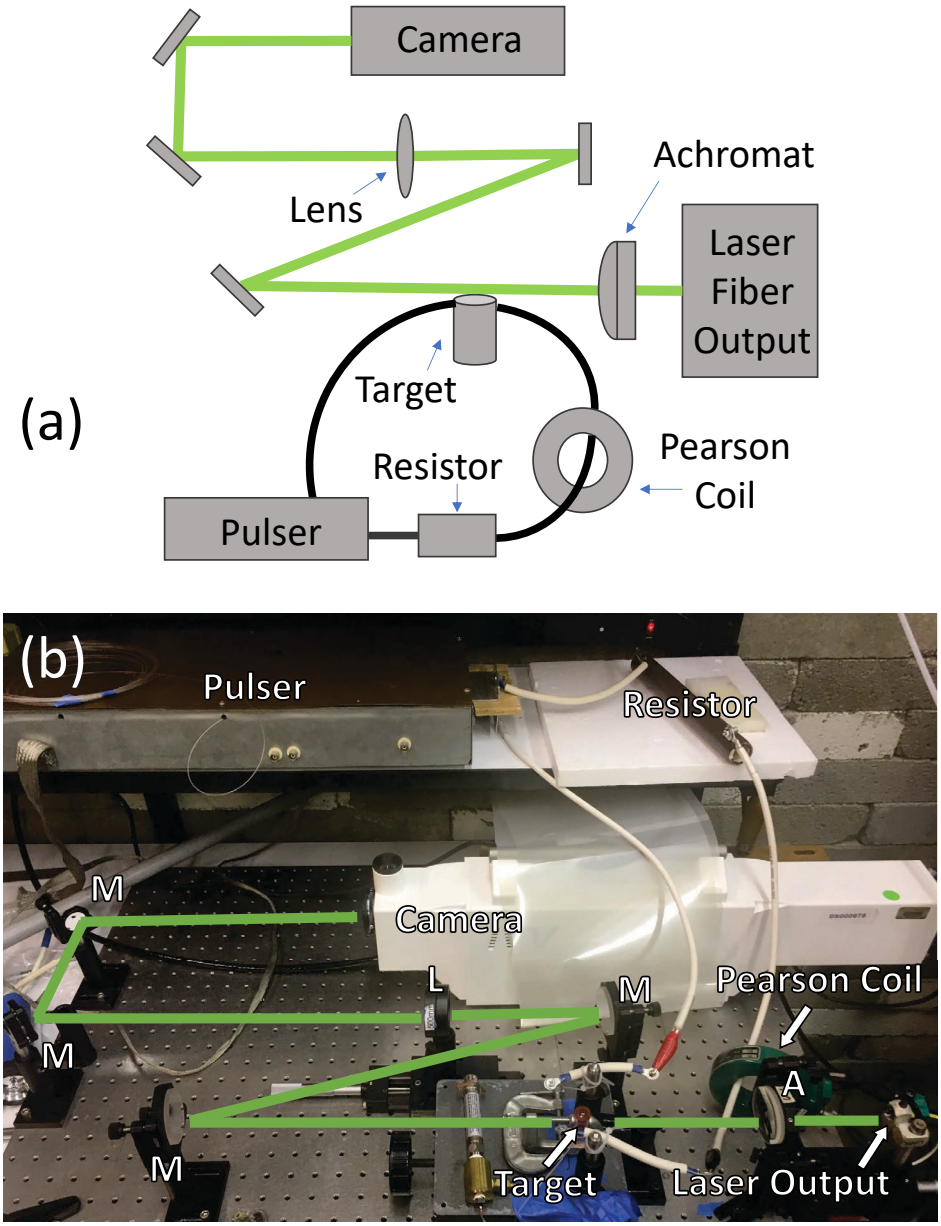

Figure 3.4: (a) Block diagram of the bright-field laser schlieren/shadowgraphy imaging system coupled to the pulser-target system. (b) Photo of the experimental configuration used to acquire schlieren/shadowgraphy images. This setup includes a collimating achromat (A), mirrors (M), and a focusing lens (L).

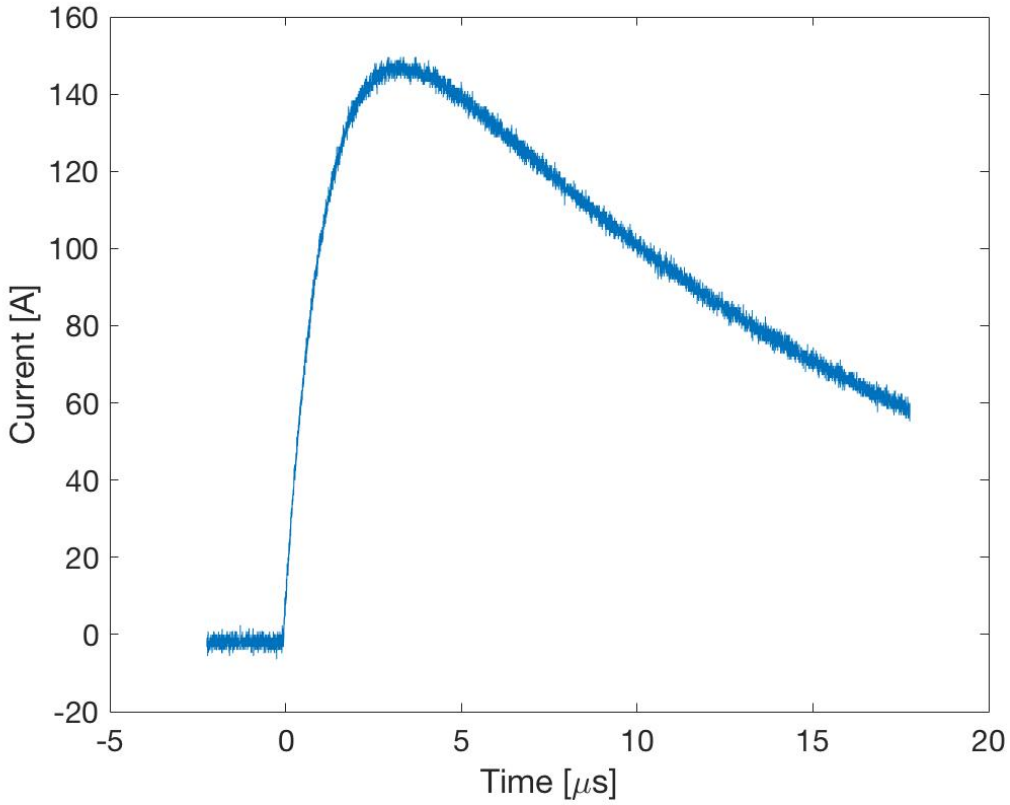

Figure 3.5: Current pulse driven through the nichrome wire to melt/weaken the LEH window. This measurement was obtained using a Pearson coil.

fiber, multiple mirrors to direct the collimated beam along the optical breadboard and through the target, and a focusing lens for relaying the light to the imaging detector. The focal length and position of the focusing lens were selected such that a negative image (a dark image on a bright background) would be formed from light rays that were refracted out of the optical system by the various target materials and escaping gas. Note that absorption and reflection processes also contribute to these negative images. Further note that our system did not use a dedicated schlieren aperture (small pinhole) at the focal point of the unperturbed laser (nor was a beam stop or knife edge used, since our system is bright-field schlieren/shadowgraphy). However, there is an effective schlieren aperture set by the acceptance angle $\Delta\phi$ of the collection optics, which is 1.46° for our system. This acceptance angle determines the minimum average density gradient ∇n that can be observed with our system. The angle is measured relative to the optical axis, and it describes the light cone that is maximally scattered by the target while still being collected by the focusing lens, L, in Fig. 3.4. If a light ray (scattered or unscattered) is collected by the focusing lens in Fig. 3.4, then it does not contribute to a dark image on a bright background field. Only light rays scattered to an angle exceeding $\Delta\phi = 1.46^\circ$ contribute to a dark image on a bright background field. The Gladstone-Dale constant [40] is calculated from $K_n = (\tilde{n} - 1)/\rho$, where $\tilde{n}$ is the index of refraction and ρ is the density of the gas (air). Calculating this gives the constant $K_n = 1.14 \times 10^{-23}$ cm^3. Also, the interaction distance is $D = 0.52$ cm through the column of escaping gas above the target, the minimum average density gradient that the system can detect/image is $\nabla n \sim \Delta\phi/(DK_n) \sim 4.3 \times 10^{21}$ cm^{-4}. For reference, the number density of the pressurized air in the target is about 5×10^{19} cm^{-3}. In future experiments, an aperture, beam stop, or knife edge could be used to reduce $\Delta\phi$ and thus measure finer density gradients. However, it is important to note that if $\Delta\phi$ is reduced too much, then the spatial resolution of the overall imaging system could become diffraction limited. For the system used in these experiments, the overall spatial resolution of about 22 μm (determined by the pixel resolution of the imaging detector) was not impacted by the system's diffraction limit, which was $d \approx \lambda/[2\sin(\Delta\phi)] \approx 10$ μm, where $\lambda = 532$ nm is the laser wavelength.

The schlieren/shadowgraphy images were recorded using a fast 12-frame ICCD camera (Invisible Vision© UHSi). For target alignment purposes, a laser power of 0.01 W was sufficient for a 100-μs exposure when the ICCD gain was set to 90.

3.2 Results

Example iPhone images of the window opening dynamics are shown in Fig. 3.6. The 0-ms frame was chosen as the last frame with no window movement. From these images, it is clear that the window material opens upwards and out of what would be the preheating laser path in a MagLIF experiment. Additionally, the window opened as if it had hinged along the side where the window was not in contact with the wire (as intended); however, the window material also completely detached from the target, which was not anticipated. Furthermore, the bending of the nichrome wire into what would be the preheating laser path of a MagLIF experiment was not anticipated.

The iPhone diagnostic was useful for demonstrating proof-of-concept, but with a 4-ms time resolution, there were many unanswered questions, including how cleanly the window opened, how fast the window opened, and how fast the nichrome wire moved into the preheating laser path. To address these questions, the bright-field laser schlieren/shadowgraphy imaging system was implemented.

Example schlieren/shadowgraphy images of the window opening dynamics, on a microsecond timescale, are presented in Fig. 3.7. For this experiment, the target was filled to $\Delta P = 27$ psi, the laser power was set to 0.03 W, the ICCD gain was set to 100, and the duration of the exposure for each frame was set to 10 μs. The images were false colored to enhance contrast and to represent the green laser (532 nm) used to backlight the experiment. The preshot was taken before the experiment, and the $t = 0$–10 μs frame corresponds to the beginning of the current pulse shown in Fig. 3.5.

In the earlier images of Fig. 3.7, the window appears to push open along a hinge on the left side of the LEH perimeter. This is consistent with the fact that the open ends of the nichrome wire extend off to the left in these images—i.e., in these images, the wire is not in contact with the window material along the left side of the LEH perimeter. Additionally, the window hinges open to a fully

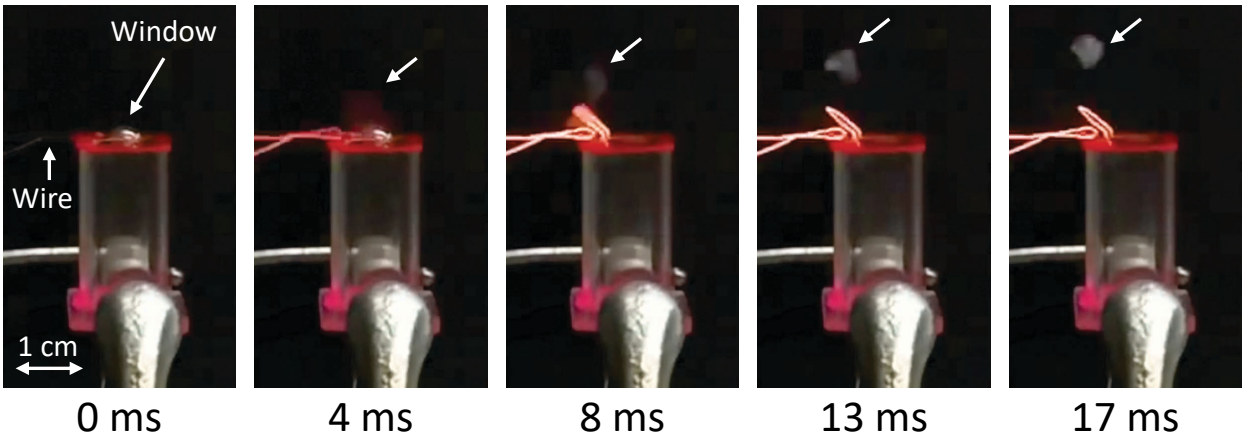

Figure 3.6: Photographs (video frames) of an LEH window opening up and out of what would be the preheating laser path in a MagLIF experiment. The white arrow points to LEH window material as it moves. The nichrome wire glows red-hot as the electrical current heats the wire and melts/weakens the window. The temporal resolution is limited by the frame rate (240 fps) of the iPhone video camera that was used to acquire these images.

upright position at $t \approx 20$ μs, which agrees well with the estimate from Eq. 2.4 ($t_{\mathrm{open}} \approx 14.3$ μs).

In the later images of Fig. 3.7, the window appears to tear away from the target after hinging open. The tear appears to be clean (with no apparent debris), and the window remains intact. These are important observations because window debris could contaminate the fuel in MagLIF and lead to enhanced radiative losses.

There are three different LEH window movement regimes that can be analyzed from Fig. 3.7. The first is defined as window opening. This includes the first four frames, when the LEH window is pivoting about its hinge point on the target. The second regime includes the fourth, fifth, and sixth frames, where a mushroom cloud, produced by the escaping gas jet, appears above the target. The third regime includes the last four frames, when the window is moving along the escaping gas column. It is important to note that all of these frames from Fig. 3.7 take place before the third frame of Fig. 3.6, which is one reason why the schlieren/shadowgraphy system was implemented. Velocities during these three regimes can be estimated. In all cases, the large uncertainty in calculated velocity comes from the time resolution of the images having 10 μs exposure. For example the location of the window in the first frame is the location from 0–10 μs (a large temporal

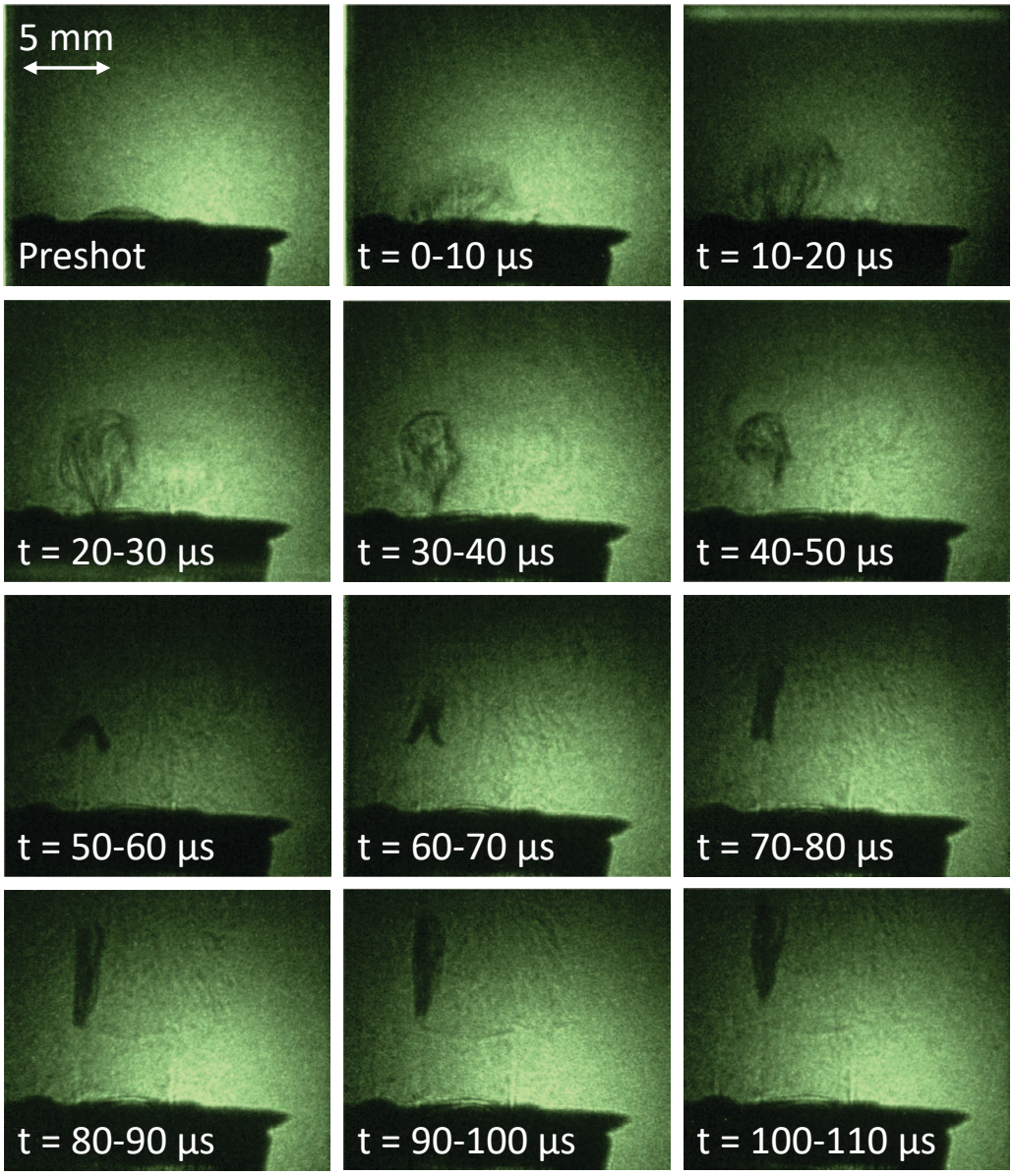

Figure 3.7: Bright-field laser schlieren/shadowgraphy images of the LEH window opening up and out of what would be the preheating laser path in a MagLIF experiment. The largely intact window appears to ride along the edge of the escaping pressurized gas column.

uncertainty). The window opening velocity is about 310 ± 80 m/s, calculated from the angular velocity of the window as it rotates open from 0 to 90 degrees (0.06 ± 0.02 rad/μs with the radius of the rotating arm equal to the 5.2 mm diameter of the window). The velocity of the escaping gas jet, calculated using the top of the mushroom cloud, is about 280 ± 110 m/s. The window's axial velocity as it moves along the escaping gas column is about 90 ± 30 m/s, calculated from the motion of the bottom edge of the window in the last four frames of Fig. 3.7. This indicates that the velocities begin near the sound speed (343 m/s) and then decrease as the pressure inside the target decreases. This slowing down as time advances and pressure decreases is also consistent with the window moving slowly in the last three frames of Fig. 3.6. The deceleration of the window at later times is likely caused by the ambient air pressure, drag on the window, and the window slipping out past the column of escaping gas into the ambient air. This further motivates conducting future experiments in vacuum conditions, where the window opening dynamics are expected to differ from the dynamics reported here. In vacuum, the escaping column of gas might change as the target gas expands into vacuum instead of air. If the shape of this escaping gas column changes in vacuum, the window movement would also likely change.

Despite becoming detached from the target, the window never crosses what would be the preheating laser path in a MagLIF experiment. In fact, it appears that the detached window rides along the edge of the escaping gas column, which is also visible in the images of Fig. 3.7. Our original intent was for the LEH window to remain attached to the target at the hinge to prevent the window from inadvertently crossing the preheating laser path as a projectile. However, if the detached window rides along the edge of the escaping gas column in a predictable way, then crossing the preheating laser path may be less of a concern after all. Consistent window movement was observed in five shots imaged by the iPhone camera and three shots imaged by the bright-field laser schlieren/shadowgraphy system. Nevertheless, there is still a concern about the detached window interfering with other equipment, such as diagnostics and the applied axial magnetic field coils used in MagLIF experiments [41]. Future experiments should be designed to assess these issues in particular. Potential solutions include altering the LEH window material (for example making

using a material that melts/weakens at different or more optimal temperature for the given heat of the wire), optimizing the heat delivery to smaller sections of the window's perimeter (for example only a quarter of contact instead of the half used presently), and strengthening the window at the hinge point (for example making the window material thicker in this area).

Finally, the images in Fig. 3.7 show that the nichrome wire remains in place for at least 100 μs. Thus, the nichrome wire will not interfere with the preheating laser pulse in MagLIF, since MagLIF experiments are conducted on timescales of hundreds of nanoseconds.

CHAPTER 4

Omega EP Wall Movement

The Laboratory for Laser Energetics (LLE) at the University of Rochester in New York has two main experimental systems: OMEGA 60 and OMEGA EP. The OMEGA EP (Extended Performance) laser system was primarily used for the experiments in this work. OMEGA EP is a pettawatt-class system with four NIF scale laser beamlines that can be used for experimental and diagnostic purposes. Two of the four beamlines are capable of producing short-pulse beams (10 to 100 ps) reaching up to 2.6 kJ of on-target energy. All four beamlines can operate in long-pulse mode (0.1 to 10 ns) reaching from 2.5 to 6.5 kJ of on-target energy depending on the pulse length [42]. Conducting experiments on this facility included working with many different people and teams that specialize in target fabrication, diagnostics, shot day approvals, and many more. All relevant shot parameters and identification information can be found in Appendix B.

4.1 Diagnostics

A major benefit of the Omega EP facility is the suite of available diagnostics. The two main diagnostics used for this work were the 4ω laser probe and the spherical crystal imager (SCI) radiography diagnostic. Figure 4.1 shows the experimental setup with the cylindrical target (cyan), the preheating beamline (shown in red), and the 4ω probe beam (shown in magenta). The SCI system (gold) [6] includes a laser backlighter (shown in blue) that interacts with a copper target generating x-rays. A quartz crystal (shown on the far right) selects the 8 keV photons that then travel toward the imager-plate detector along the SCI axis (green). The following sections describe both these diagnostics.

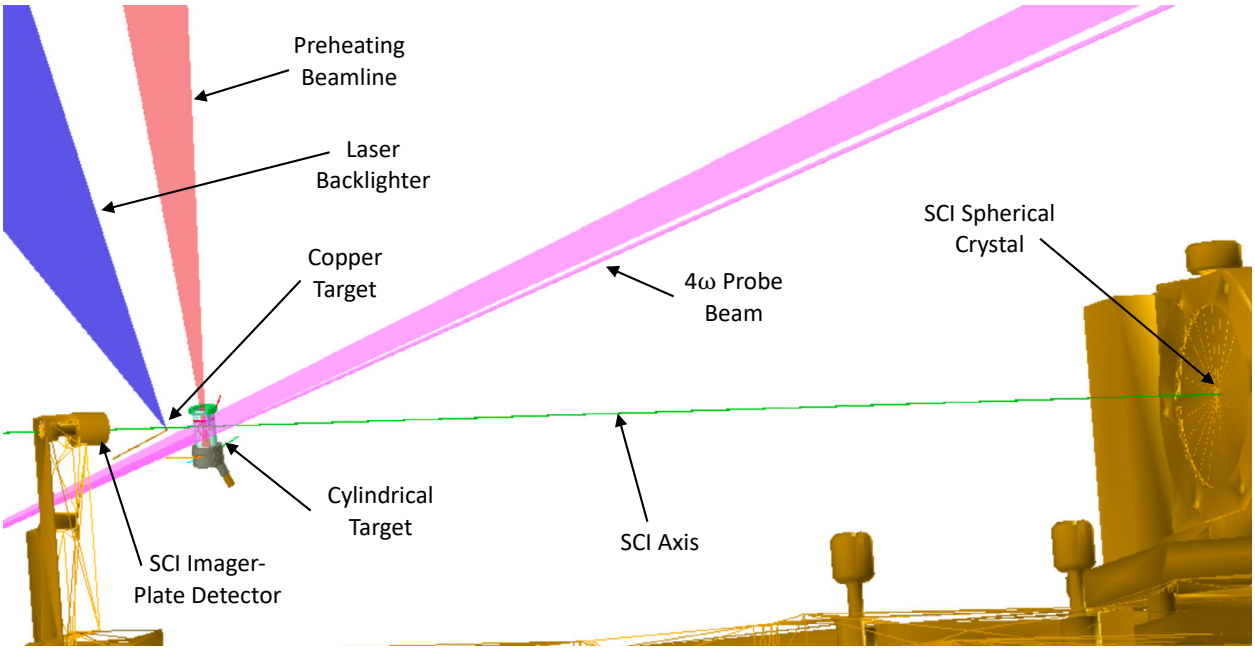

Figure 4.1: VisRad schematic of the experimental setup at Omega EP with the cylindrical target (cyan), the preheating beamline (shown in red), the 4ω probe beam (shown in magenta), and the crystal imager radiography (gold) with its laser backlighter (shown in blue).

4.1.1 4ω Probe Optical Diagnostic

To track the movement of the liner's outer surface, a diagnostic called a 4ω probe was used. The 4ω probe for Omega EP was established in 2012 [5]. It is a 10 ps, 20 mJ, 5 mm spot size, 4ω probe laser designed to image long length scale plasmas over a field of view that is several millimeters in diameter. A ten inch manipulator (TIM) that attaches to the target chamber contains most of the probe components, as shown in Fig. 4.2. The diagnostic can be configured for schlieren/shadowgraphy, grid-imaging refractometry, and interferometry. For these experiments, it was used in the schlieren/shadowgraphy configuration. In this configuration, an image of the target plane is formed on the charge-coupled-device (CCD) imaging plane. This diagnostic is similar to the schlieren/shadowgraphy setup used in Sec. 3.1.2. Schlieren/shadowgraphy is ideal for imaging refracted or diffracted light from large density gradients. In this setup, it is used for edge tracking of a solid material, so the produced images show a sharp wall edge. The 4ω probe imaging system has a 2.5 mm field of view with a 13.5 micron pixel resolution in the imaging plane.

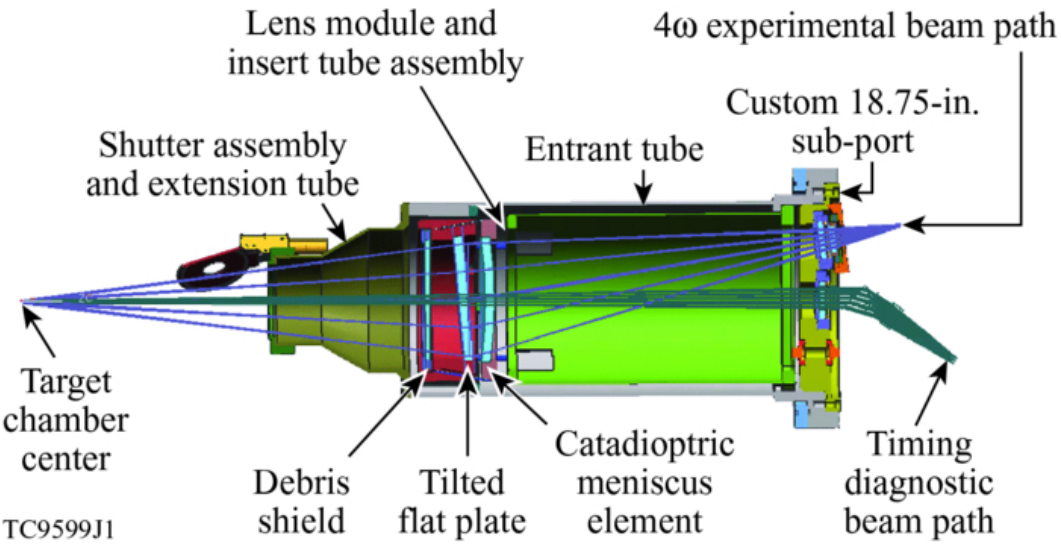

Figure 4.2: Most of the 4ω diagnostic components are contained in a TIM that attaches to the target chamber. Some prominent features include the beam path, shutter, timing diagnostic, and debris shield [5].

The diagnostic viewing window is shown in relation to the target body in Fig. 4.3. The gold circle shows the field of view captured in the experiment relative to the rest of the experimental setup. Here, the preheating laser beam (red) enters the target (cyan) from the top of the target at the LEH window. An example of the resulting experimental image is shown in Fig. 4.4. There are two 4ω probe images from each shot: a preshot image and an image after the preheating laser has entered the target. Wall movement is found by subtracting the location of the wall in the preshot image from the location of the wall in the laser heated image. From the known timing delay of the shot, the velocity of the wall movement can be calculated.

4.1.2 Spherical Crystal Imager (SCI) for Radiography

A transmission radiography diagnostic was used to analyze the density of the liner wall in time as the wall expands. This was done using a spherical crystal imager (SCI). Omega EP's SCI is a narrowband imager for the Cu K-α emission line at about 8 keV [6]. These emission lines are produced from a 1 kJ laser irradiating a copper target. This SCI uses a spherically bent quartz crystal and a Bragg angle of 88.7°. The main system components are housed in two ten-inch manipulators (TIMs). One TIM houses the crystal and the other houses the image-plate detector. Figure 4.5 shows

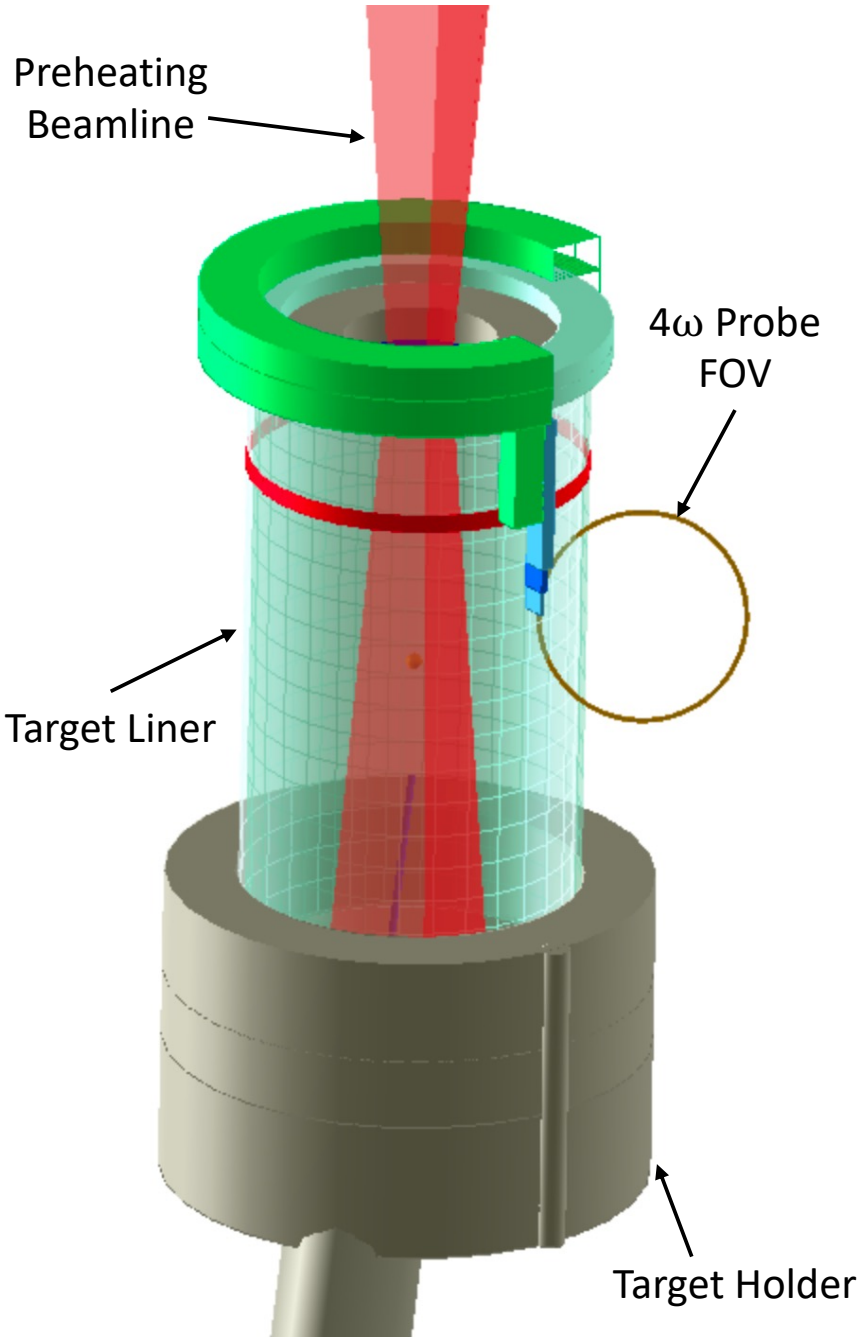

Figure 4.3: VisRad illustration of the experimental configuration. The 4ω probe's field of view is shown with the gold circle. This demonstrates which part of the target wall this diagnostic is capable of imaging.

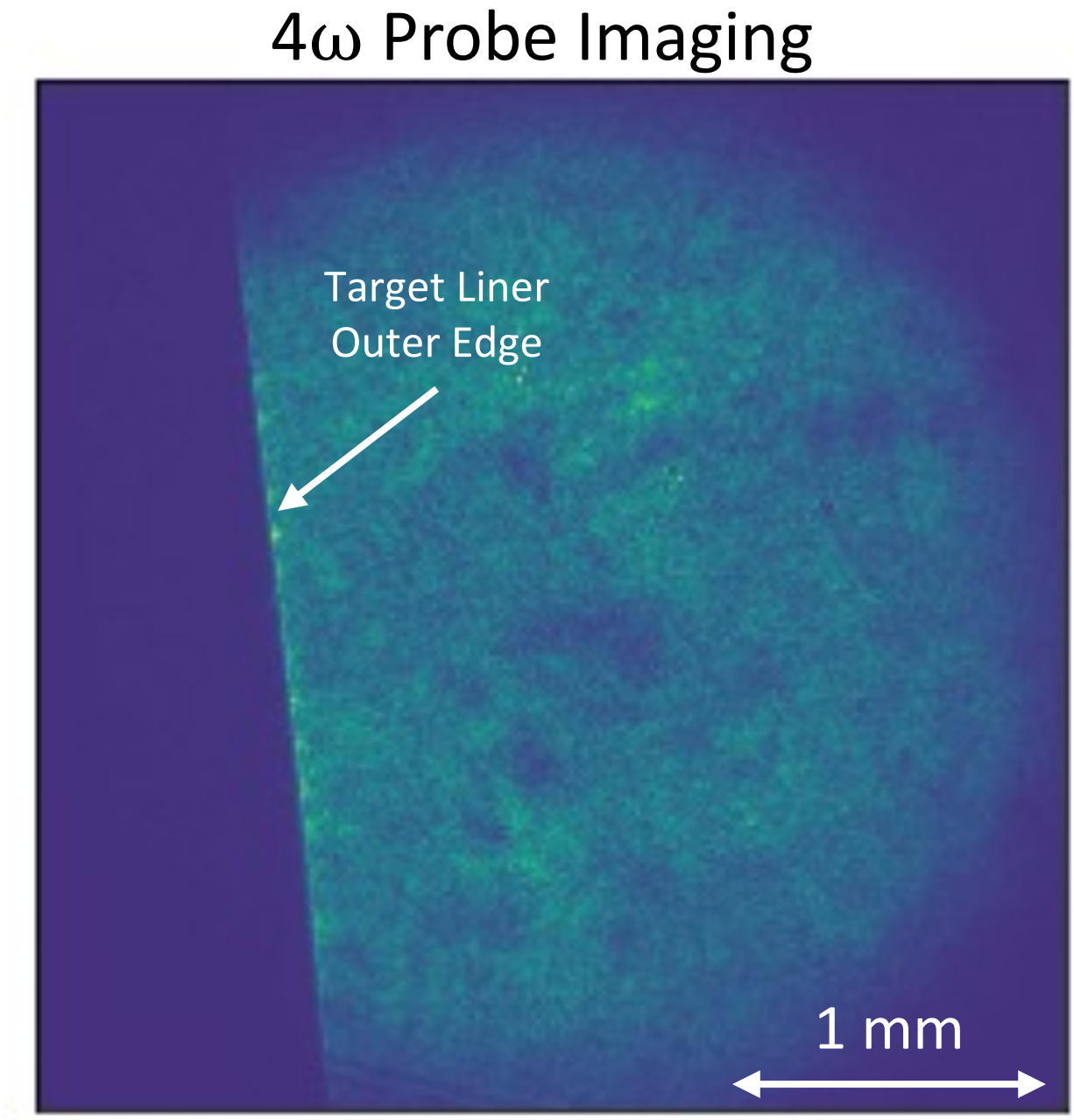

Figure 4.4: An example image produced form the 4ω probe (from Omega EP shot 36784). This field of view is associated with the gold viewing window shown in Fig. 4.3.

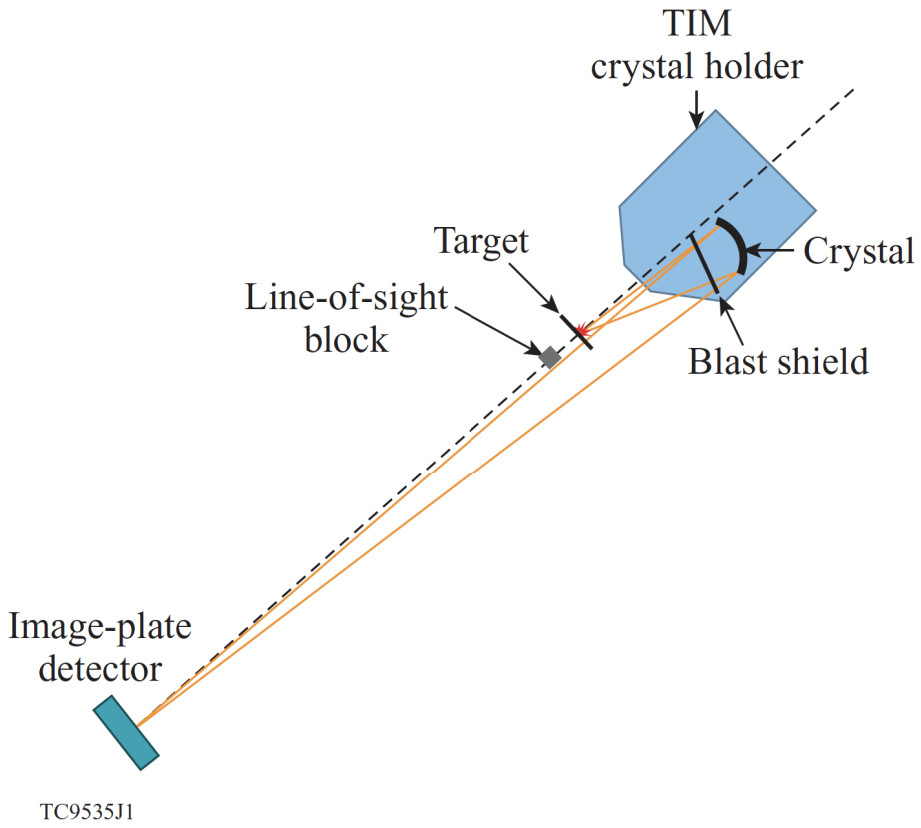

Figure 4.5: A schematic of the spherical crystal imager used to capture radiographs of the liner wall. The components are held mainly in two ten-inch manipulators (TIMs). One TIM houses the crystal while the other houses the image-plate detector. The emitted x-rays pass through the liner wall, reflect off the crystal, and then land on the image-plate detector [6].

the configuration of the SCI's components. This setup is used to obtain radiographs of the edge of the target wall. Figure 4.6 shows the field of view (gold circle) obtained during these experiments in relation to the target body (cyan) and aluminum strip fiducial (blue). An example radiograph is shown in Fig. 4.7.

As the Cu K-α x-rays are attenuated by the liner wall and fiducial. This signal attenuation can be used to determine the density of the liner. Conducting many experiments at various timing delays can provide an understanding of the liner density movement over time. The diagnostic spatial resolution is quoted to be 10 μm [43]. However, the configuration used for these experiments differed from the setup used to obtain the optimal system resolution. Mainly, the distances between the corresponding diagnostic elements were shifted to account for the desired viewing window

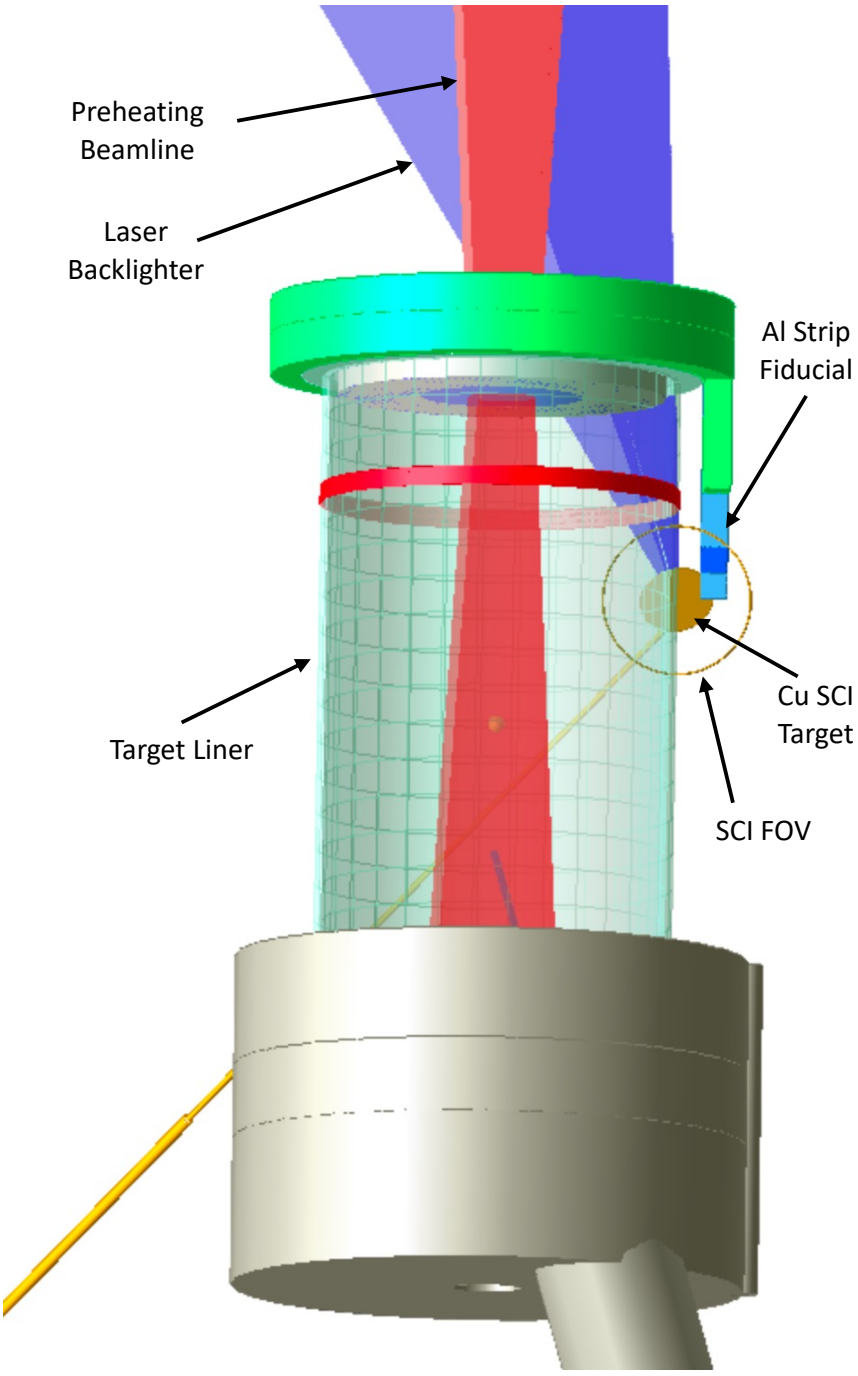

Figure 4.6: VisRad illustration of the experimental configuration. The gold circle represents the field of view of the liner wall and fiducial as the preheating laser (shown red) heats the target fuel causing movement in the liner. A second laser beam (shown in blue) hits a copper foil to produce the x-rays needed for the radiography diagnostic.

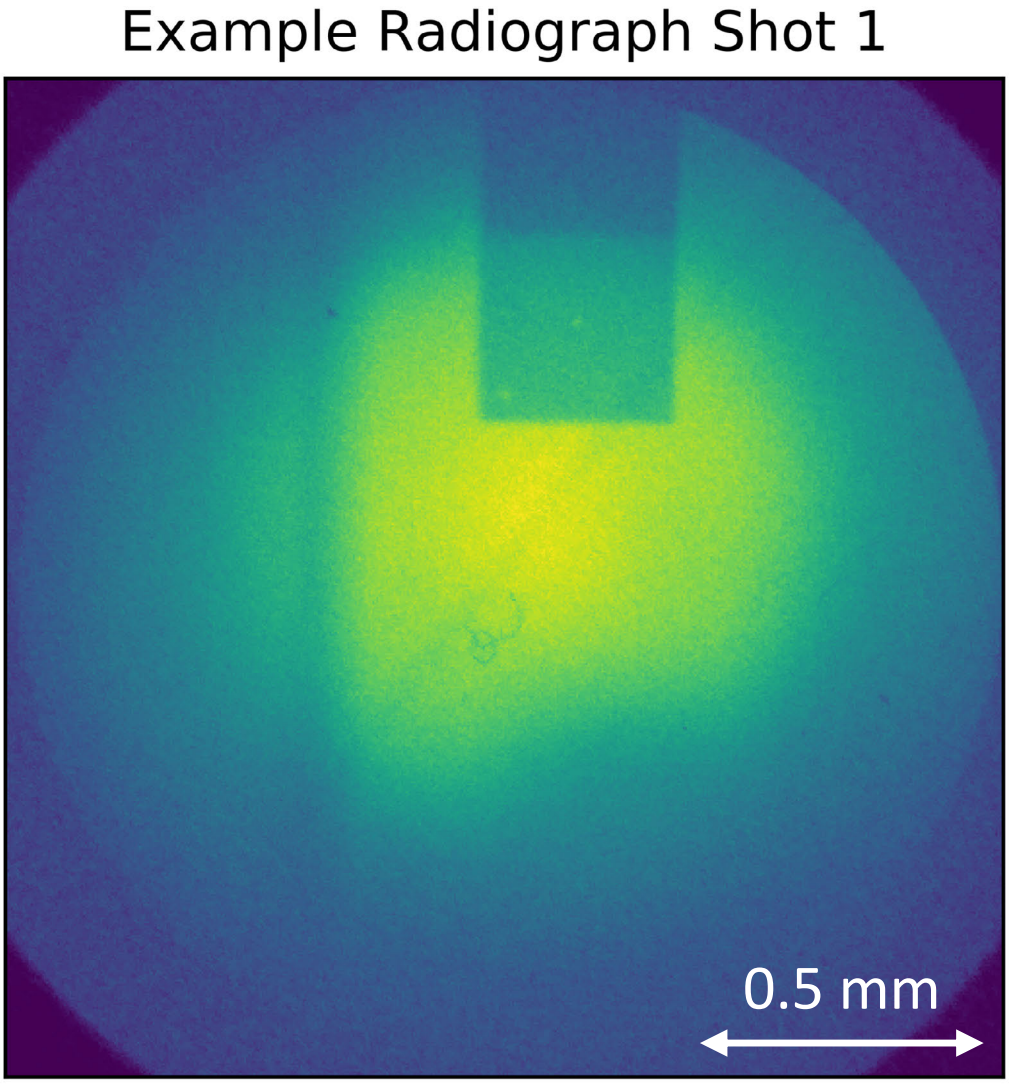

Figure 4.7: An example image produced from the spherical crystal imager. This image is associated with the field of view shown in Fig. 4.6. The liner wall (left) and fiducial (top) are both visible in this configuration.

and size. Resolution calculations were performed for this experiment using a mesh grid resolution target. The target design is discussed in Sec. 4.2 and the resolution calculation process is shown in Appendix A.

4.2 Target Design

While the MagLIF platform is primarily studied on the Z Machine at SNL, there are benefits to studying this concept at other facilities. As mentioned in the above diagnostics section, there is an already established and robust diagnostic suite for laser-driven experiments at the Omega EP facility. Additionally, Omega EP can support multiple shots per day, whereas the Z facility is limited to one shot per day. However, there are two key differences in the facilities to consider. First, Omega EP is primarily a laser facility, so there are no pulsed power capabilities to compress the liner. This means that only the laser preheating stage (and not the compression stage) of MagLIF is studied in these Omega EP experiments. Second, the laser beam parameters are slightly different, so the Omega EP experiment (mainly the target parameters) must be scaled to keep the physics of the experiments relevant to the preexisting MagLIF experimental platform.

The liners for the Omega EP experiments were designed to be similar to the MagLIF liners used for implosion experiments on the Z Machine. The liner radius was fixed to match the MagLIF liners. The Omega EP laser is frequency tripled (λ = 351 nm) with a super Gaussian spacial profile (FWHM = 1.1 mm). The key scaling parameter chosen to be equivalent between the platforms was the laser energy deposition per unit length inside the target. This parameter was chosen to scale the experiment because the physics of the preheating laser beam depositing energy into the target and the corresponding target wall movement is the focus of these studies. Fixing the energy deposition per unit length left the fuel density as the remaining scalable parameter which is calculated, from Ref. [44], to be:

$$\rho_{\mathrm{DD}}\left(\mathrm{mg/cm^3}\right) \simeq \left(\frac{3.47N^{4/5}\left[\,E_{\mathrm{preheat}}\,(\mathrm{kJ})\right]^{3/5}}{z_{\mathrm{p}}\,(\mathrm{mm})\left[\,R_{\mathrm{spot}}\,(\mathrm{mm})\right]^{6/5}}\right)^{5/7} \tag{4.1}$$

Table 4.1: Comparison of Omega EP and SNL MagLIF target and laser parameters used to determine the energy deposition per length scaling parameter.

Target Parameters	Omega EP Targets (LLE)	MagLIF Targets (SNL)
Target Radius (mm)	2.4	2.4
Target Fuel Density ($\mathrm{mg/cm^3}$)	1.62	1.05
Beam Frequency	3ω	2ω
Beam Spot Size (mm)	1.1	1.5
Preheat Energy (kJ)	~ 1	~ 1

where z_{p} is the propagation distance, $N = 1.054/\lambda_{\mu\mathrm{m}}$ is the laser harmonic, $\lambda_{\mu\mathrm{m}}$ is the laser wavelength in microns, E_{preheat} is the energy of the preheating laser beam in kilojoules, ρ_{DD} is the mass density of the deuterium fuel in milligrams per cubic centimeter, and R_{spot} is the spotsize of the laser beam in millimeters.

To hold the preheating energy per unit length constant while using the parameters listed in Table 4.1, the fuel density needed to be $\rho_{\mathrm{DD}} = 1.73$ mg/cm^3. However, the actual density of the fuel right before the experiments was 1.62 mg/cm^3. This reduction in density would result in about a 10% increase in penetration depth and a 10% reduction in energy deposition per unit length. Note that the MagLIF parameters chosen for the Omega EP scaling, shown in Table 4.1, come from the highest energy deposition per unit length case that has been fielded for MagLIF at Sandia.

In addition to the target itself, fiducials were included to gain additional insight into the experiment. There were two fiducials included on each target, a "band" and a "strip", both shown in Fig. 4.8. The band fiducial is a 10 μm thick copper piece that wraps around the majority of the target near the LEH. The band was an important fiducial in another experimental campaign not covered here and was intended to be used in the 4ω probe diagnostic to align the target and get a sense of spatial scale. However, this band fiducial did not end up being in the field of view for the 4ω probe. The known field of view size was used instead to get a sense of spatial scale. The strip fiducial is a layered aluminum strip with three different thicknesses: 50, 100 and 200 microns. This was designed to help calculate the transmission through the different thicknesses and provide additional certainty to the target density calculations. However, the radiography diagnostic's field of

view was not large enough to capture the full fiducial in each shot. So, for consistency, only the 50 μm thick portion of the fiducial was used for the density calculations. The radiography field of view was aligned to image a section of the liner that was not near the fiducial. This was done so that images of the wall movement were not affected by the presence of the fiducial.

Finally, a separate copper mesh target was designed and implemented to calculate the resolution of the radiographs. One shot from the campaign was allotted for this resolution target. This copper mesh target, shown in Fig. 4.9, was designed to have strips in both the horizontal and vertical directions to calculate the resolution capabilities of the radiography diagnostic (see Appendix A for more details). Each strip is 0.08 mm wide and 0.02 mm thick. The distance between the midline of each strip is 0.42 mm. Additionally, with a known mesh structure that allowed a lot of the unattenuated Cu K-α x-rays to reach the detector, a beam profile could be determined. It is crucial to account for the shape of the beam profile when calculating the density of the liner wall. The attenuation of the beam is necessary and thus the unperturbed beam profile must be normalized to obtain this attenuation.

The fiducials were critical to diagnosing the experiments. However, modifications to the existing fiducials and/or the inclusion of additional fiducials would be helpful in future studies. These recommendations are presented in Ch. 5.

4.3 Results

4.3.1 Wall Edge Movement from 4ω Probe

Once the preheating laser enters the target and heats the fuel, it creates shock waves that accelerate the liner wall radially outward from the cylindrical axis. To track the wall movement, the outer "edge" of the liner is located before and after the preheating laser enters the target. There are five experimental shots used for the following analysis. Each experiment acquired a "preshot" image of the target before the laser had entered the target and an image of the wall in motion after the laser had heated the fuel. The image times were varied by adjusting the time delay (offset) between when the preheating laser fired and when the diagnostic lasers fired (where the diagnostic lasers included

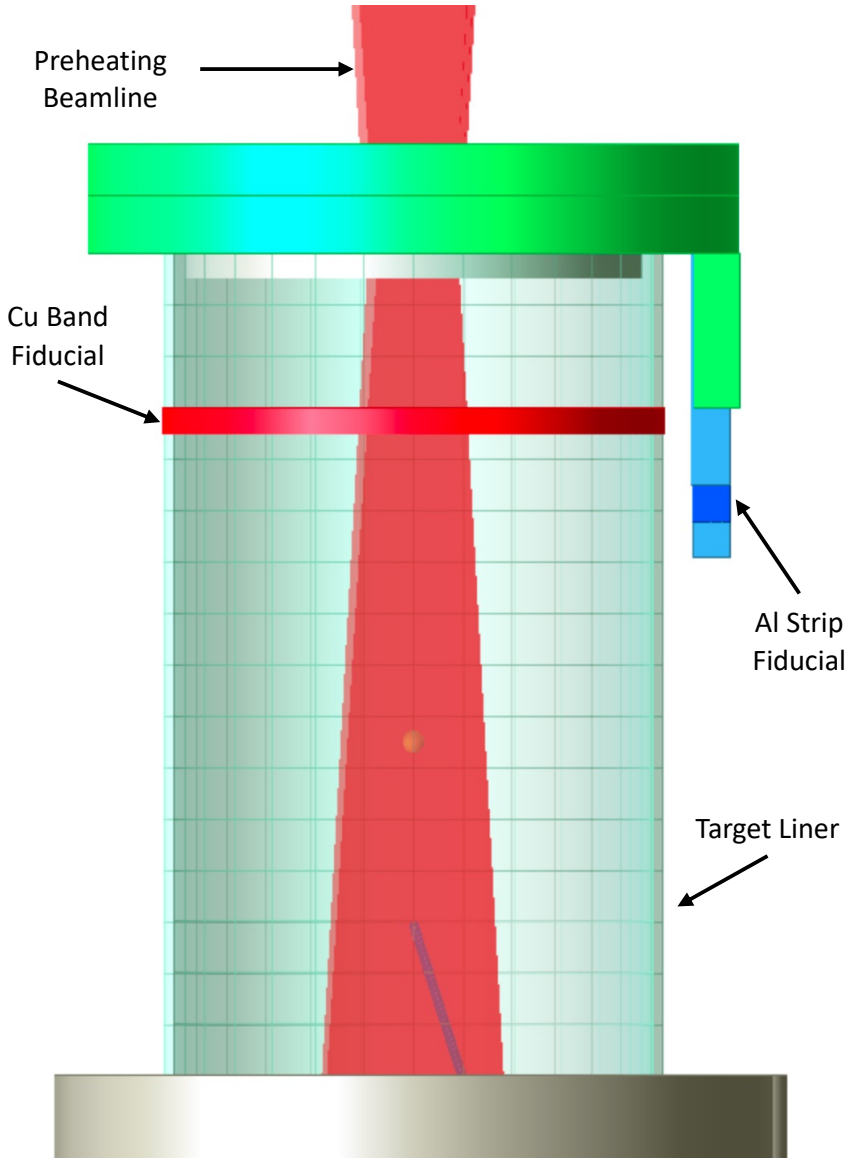

Figure 4.8: VisRad illustration of the experimental configuration. A side-on view of the target is shown. The light red shows the preheating laser beam entering the target. The dark red ring near the top of the target is the copper "band" fiducial. The blue strip to the right of the target is the aluminum "strip" fiducial. The strip fiducial has three thicknesses: 50, 100, and 200 microns.

Figure 4.9: VisRad illustration of the configuration used for experimental calibration. A copper mesh target was used to determine the resolution of the radiography setup. The mesh strips are 0.08 mm wide and 0.02 mm thick.

both the 4ω laser probe and the radiography laser). The delay times (offsets) were set to 25, 30, 35, and 40 ns. Note that two shots were acquired with the 25-ns offset. The 4ω probe described in Sec. 4.1.1 was used to image this wall movement. The location of the outer surface of the wall in the preshot images is subtracted from the location of the outer surface in each time-delayed image. This difference represents how far the wall has moved in the given amount of offset time.

Figure 4.10 shows the 4ω laser probe data for Omega EP shot 6, which used a time offset of 15 ns. In this figure, subfigure (a) shows the preshot image, with the edge tracking locations indicated by the black dots. Subfigure (b) the shot image while the wall is in motion, with the edge tracking indicated by the white dots. Subfigure (c) presents an overlay of the preshot and shot images. Subfigure (d) presents the same overlay with the edge tracking locations indicated. There is a bump on the liner present in the preshot image (Fig. 4.10a), and some additional streaks near this bump in the $t = 40$ ns shot images (Fig. 4.10b). These are only visible on the $t = 40$ ns radiographs. This is thought to be either debris on the target or on the optics.

For each experiment, the wall edge is located as a function of axial position for both the preshot image and the shot image. This edge tracking considers the edge to be the location where the intensity from the schlieren/shadowgraphy image drops to half of the max intensity. As shown in Sec. 2.3, the density of the target is expected to have a large low-density tail region in later times. This low density tail is expected to introduce extra error in the edge detection, especially at later time offsets. The wall location is the difference between the wall positions in the shot and preshot images plus the outer radius (2.425 mm). Wall edge location (radial distance from the target center) is plotted as a function of distance from the LEH (depth into the target) in Fig. 4.11. The target length from the bottom of the LEH to the end of the wall region is 10 mm. In these experiments, the field of view of the 4ω probe shows the target from about 3 to 4.5 mm from the LEH, capturing a 1.5 mm region just above the axial midpoint of the 10 mm long target.

Based on simulations, the lowest offset of 25 ns was selected to capture signs of outer wall movement. A small amount of wall movement can be seen in the shot with the 25 ns offset (shown in Fig. 4.11). This indicates that the $t = 25$ ns case did capture the first signs of wall movement. As

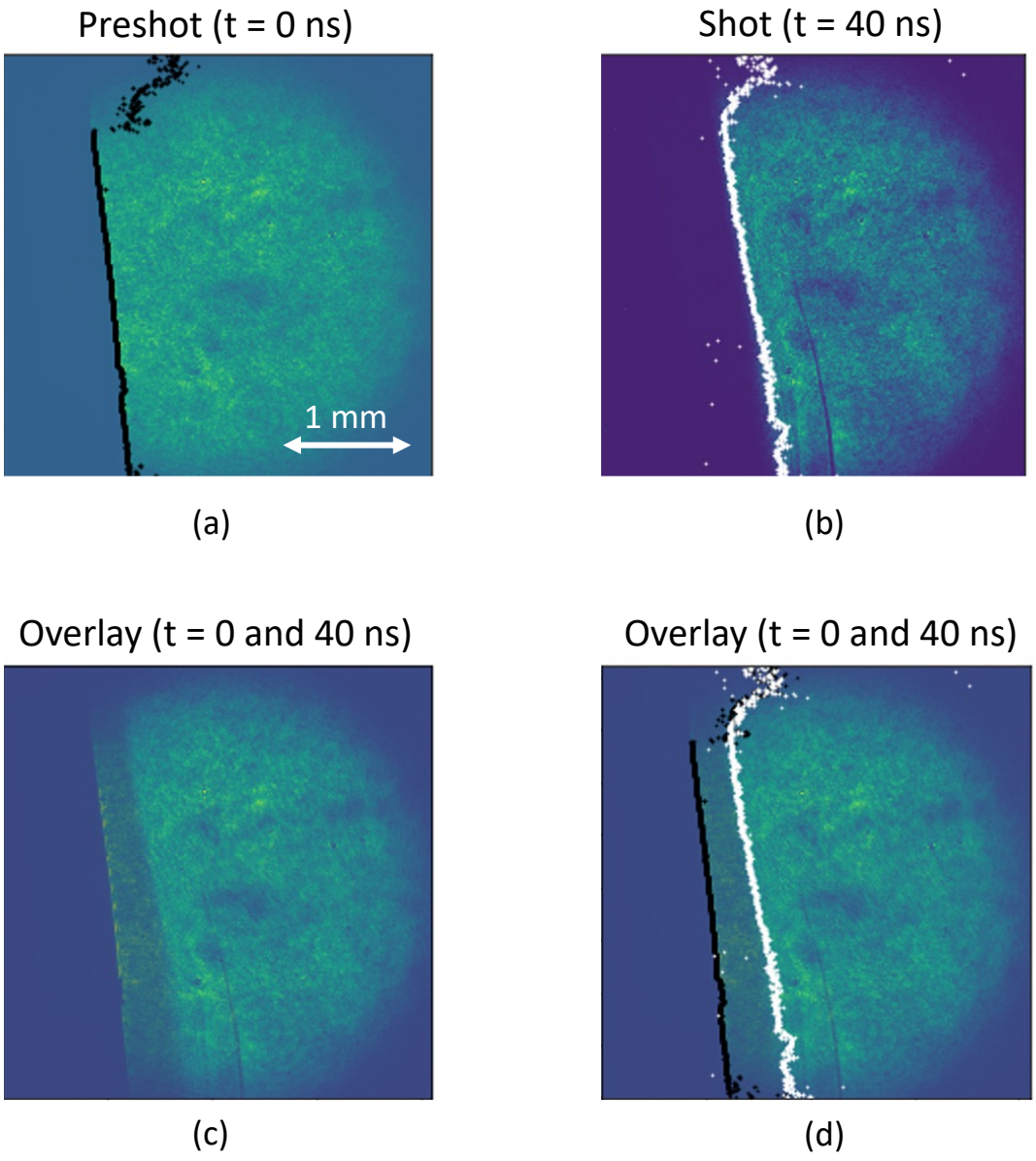

Figure 4.10: Data from the 4ω laser probe on Omega EP shot 6, which had a time offset of 40 ns. Two images are captured for each time offset in the series. Preshot image with edge tracking indicated by the black dots (a). Shot image (while the wall is in motion) with edge tracking indicated by the white dots (b). Overlay of preshot and shot images (c). Overlay of preshot and shot images with edge tracking locations shown (d).

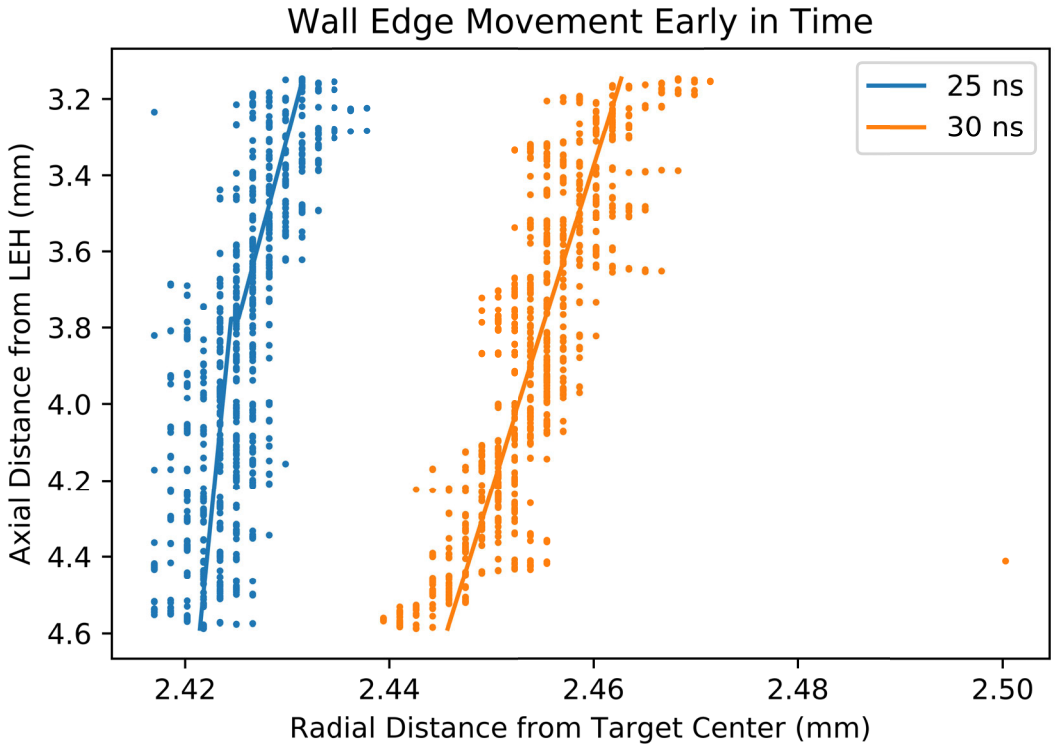

Figure 4.11: As the preheating laser enters the target, the liner walls begin to move. Early in time, there is more wall displacement closer to the LEH. The outer surface of the wall has begun to move at 25 ns and by 30 ns has moved up to about 40 microns. The experimental field of view spans 3–4.5 mm from the LEH.

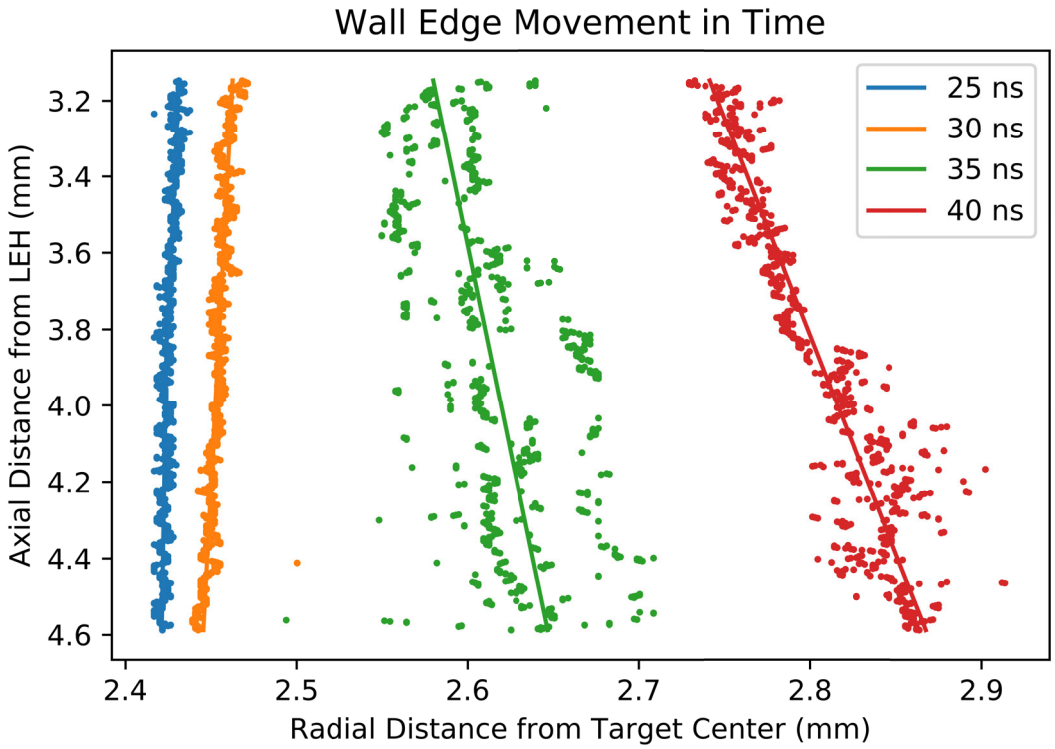

Figure 4.12: As the preheating laser enters the target, the liner walls begin to move. At 25 and 30 ns, there is more wall displacement near the LEH. At 35 and 40 ns, there is more wall displacement farther from the LEH. The increase of displacement deeper into the target at later times was not predicted by simulations.

the outer surface begins to move, an interesting dynamic is observed. Figure 4.12 shows that around the beginning of wall movement, the wall axially closer to the LEH has a greater displacement, then later in time, the wall movement is greatest deeper into the target. The HYDRA simulations, shown in Fig. 2.8, do show an axial dependence of wall movement. However, Fig. 4.12 shows the opposite dependence at later times of what is predicted in the simulations.

From the simulation data presented in Fig.2.8 (courtesy of HYDRA simulations from M. Weis at SNL), the wall movement is plotted as a function of time in Fig. 4.13 for five different cases including two axial positions of simulated displacement, the maximum simulated wall movement, and two axial positions of experimental displacement. Figure 4.13 shows the non linear relationship of outer surface movement in time. The wall movement in the experiment starts out less than simulated then quickly moves beyond the corresponding simulated axial location displacements

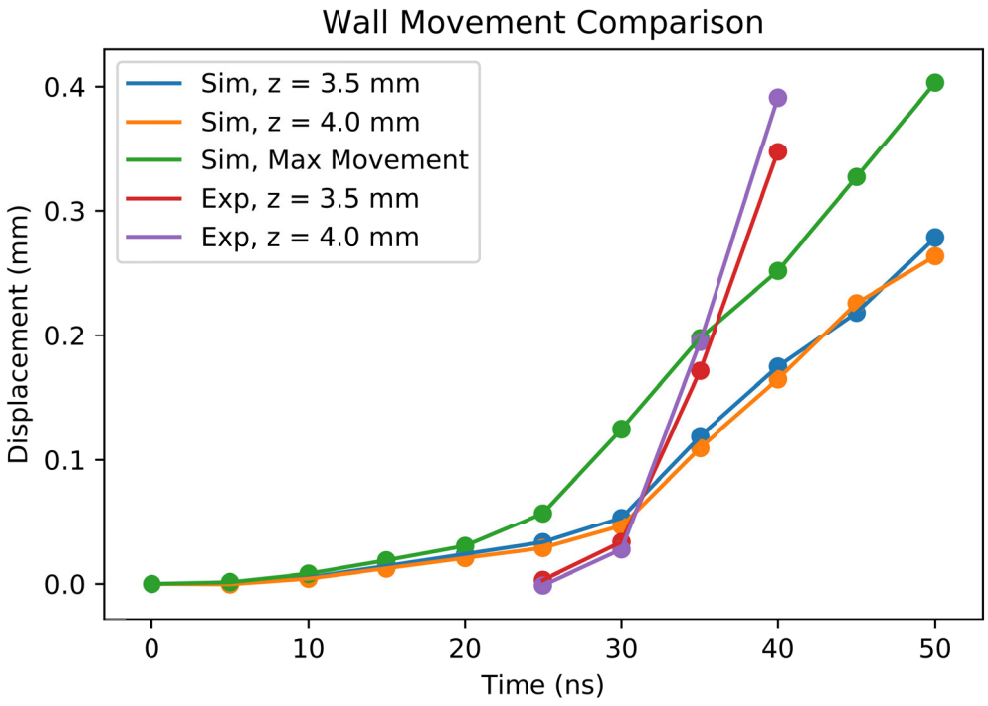

Figure 4.13: Wall displacement as a function of time is shown for $z = 3.5$ mm and $z = 4.0$ mm for both simulated and experimental data as well as the maximum displacement simulated. The wall displacement increases (and accelerates) in time, but the experimental wall location is moving and accelerating much faster than simulated.

at $t = 35$ ns and beyond the maximum simulated displacement at $t = 40$ ns. This indicates the experimental wall is moving much faster than simulated. This could mean the physical shock waves are stronger than simulated.

All of the experimental wall movement is compared to simulated movement in Fig. 4.14. The experimental locations are much closer to the simulated locations early in time at 25 and 30 ns. Then, later in time the difference grows. Later in time, the experimental locations are closest to the simulated locations closer to the LEH (at axial position $z = 3.25$ mm). Then, deeper into the target, the experimental wall locations diverge even further from the simulated locations. In future experiments, it would be beneficial to study this further especially by probing the entire axial length of the target to see if the displacement peaks deeper into the target than predicted, or continues to increase down the entire length of the target. These experiments suggest the wall is moving faster than predicted.

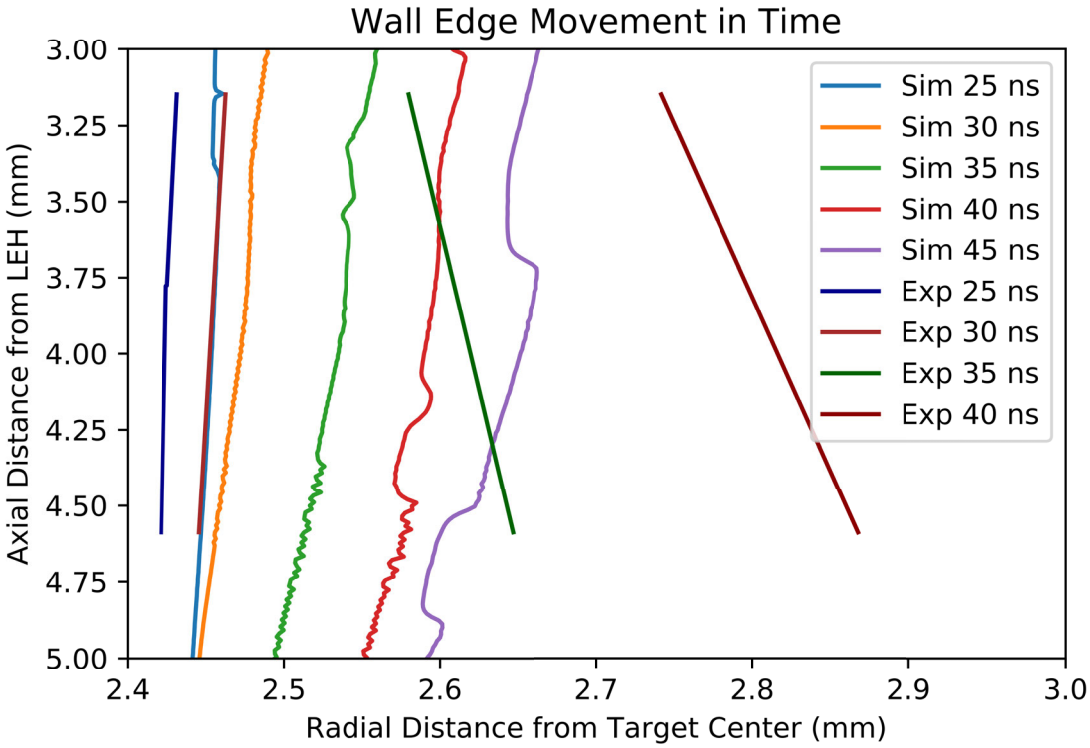

Figure 4.14: The simulated and experimental wall edge movement is shown from 3 to 4 mm from the LEH for different times. Early in time (25 and 30 ns), the wall experimentally moves closer to predicted than at later times (35 and 40 ns). The wall is also experimentally moving more deeper into the target, the opposite of the predictions.

It is important to note that each image comes from a series of separate experiments. However, the target pressures, target dimensions, and laser energy depositions were all very similar. The target pressure at shot time varied by 1.2%. Finally, the laser energy across the shots varied by 1.3%. This high precision in experimental specifications allows for these series of individual experiments to be analyzed as a collective.

4.3.2 Radiography

As described in Sec. 4.1.2, a spherical crystal imager (SCI) was used to capture radiographs for each experiment. Each radiograph is used to determine the liner density as a function of radial and axial location. This allows for a more in-depth analysis than the simple edge tracking of the 4ω probe data. As the preheating laser heats the target fuel, it creates a shock wave that moves through the target. As the shock hits the liner wall, the wall first compresses and then spreads out. This compression and expansion can be analyzed through density measurements with the SCI diagnostic. As described in Sec. 2.3, it appears there are two separate compression waves that move through the liner wall.

The SCI diagnostic generates one radiograph per experiment. Each radiograph was taken at a different timing offset to capture the liner movement as a function of time. From the radiographs, densities plots and liner mass conservation were determined. To determine the density profile, the radiographs are processed and converted to transmission profiles. Then, areal density is calculated from transmission values. Finally, an Abel inversion is used to transform areal density to density. First, the raw radiographs, shown in Fig. 4.15, must be rotated and cropped. Then, the determined beam profile, shown in Fig. A.9(a), is used to correct the radiograph for the shape of the beam. This flattened field is shown in Fig. 4.16. An aluminum strip fiducial with known thicknesses is in the field of view of the radiograph (located at the bottom). The fiducial information allows for intensity to be converted to transmission values. A background correction factor is found from,

$$\tau_{Al50} = \frac{I_1 - b}{I_0 - b} \tag{4.2}$$

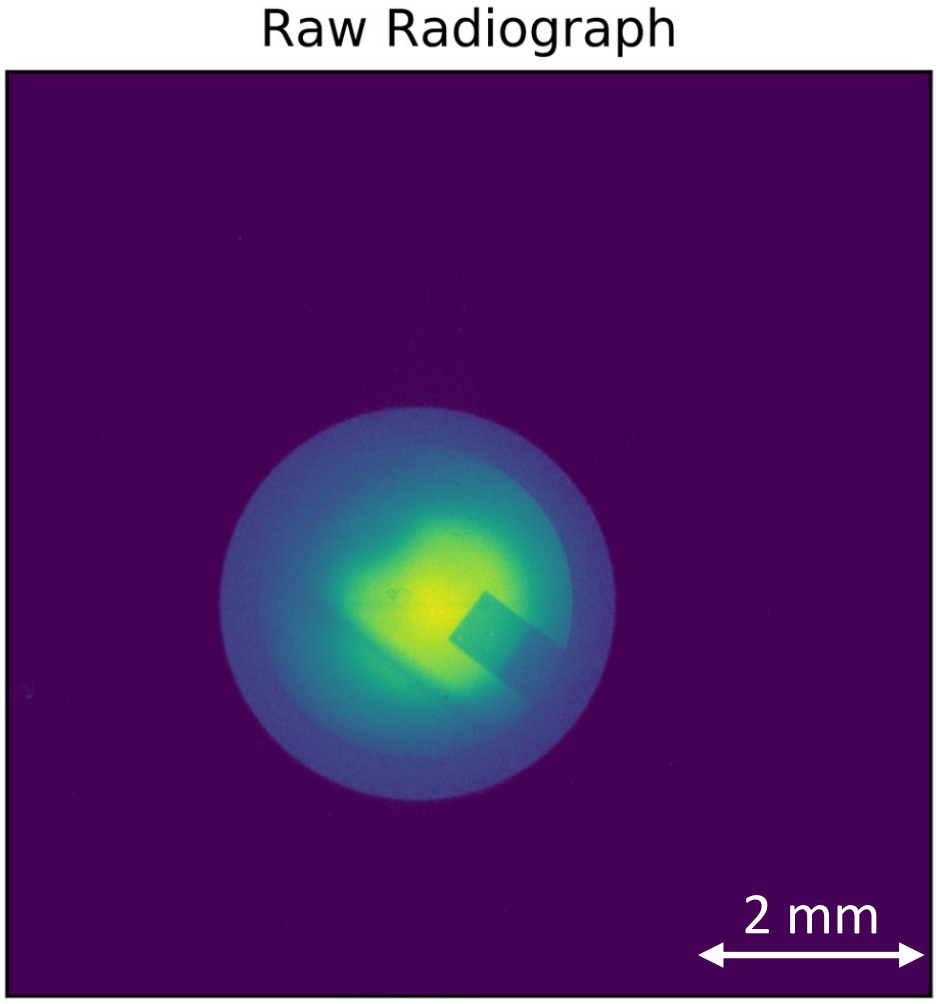

Figure 4.15: Raw data radiograph of the Parylene-N liner wall and aluminum fiducial. One radiograph, like this one, was taken for each experimental shot. This radiograph is from Omega EP shot 36785, and it used a timing offset of $t = 35$ ns.

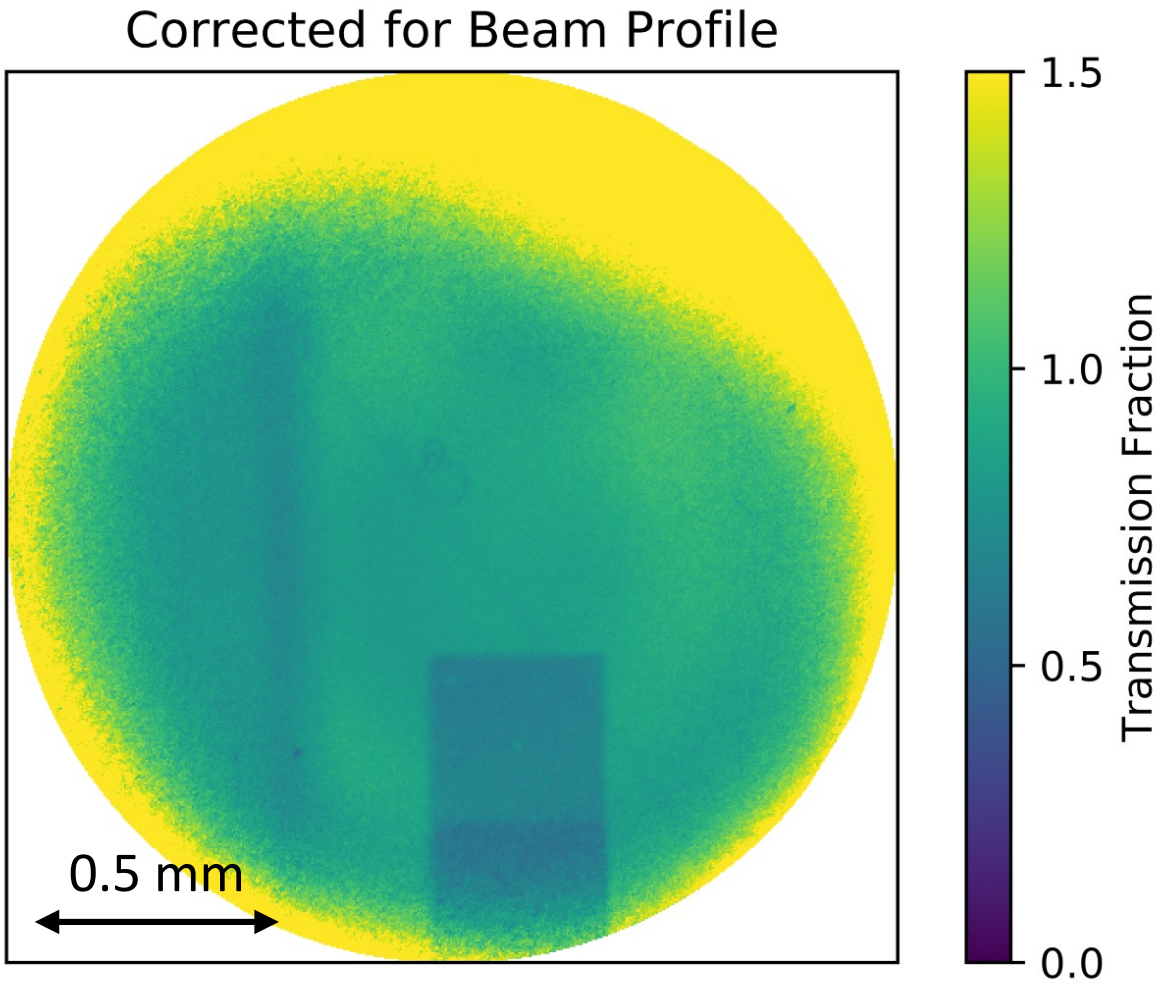

Figure 4.16: Radiograph from Omega EP shot 36785, with a timing offset of 35 ns, after being rotated, cropped, and normalized to flatten out the associated beam profile. The beam profile used to normalize the image data is shown in Fig. A.9(a).

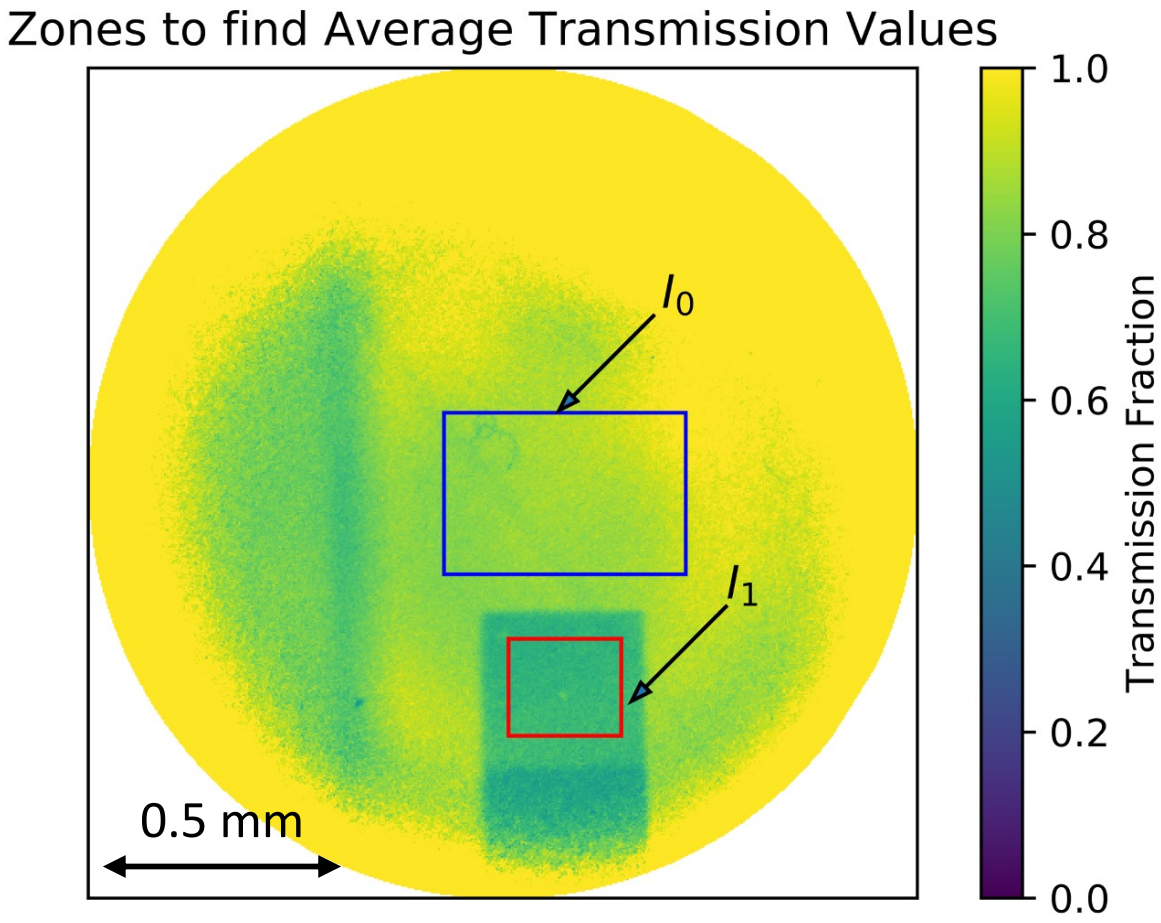

Figure 4.17: Partially processed radiograph from Omega EP shot 36785. The boxes correspond to the regions used to convert the radiograph intensity to transmission. The blue rectangle outlines the unattenuated signal and the red rectangle outlines the signal attenuated by the 50 micron thick aluminum fiducial.

Solving for the background signal gives,

$$b = \frac{\tau_{Al50} * I_0 - I_1}{\tau_{Al50} - 1} \tag{4.3}$$

where b is the background signal, $\tau_{Al50} = 0.53$ is the transmission through the 50 micron thick aluminum fiducial from the Henke tables [45], I_1 is the intensity in the region of the fiducial, and I_0 the intensity in the unattenuated region. The intensities are uncorrected fractional transmission values. Regions for I_0 and I_1 are shown in Fig. 4.17.

This background value is subtracted from the intensity and then, to find the transmission, the

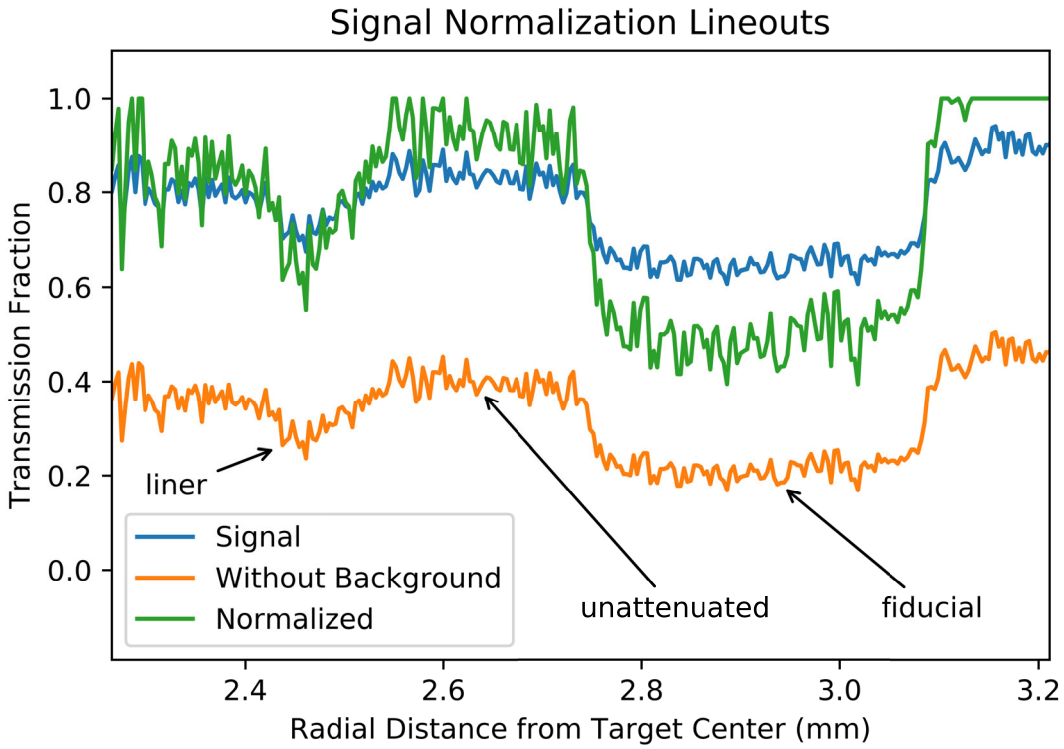

Figure 4.18: Radiograph lineouts at various stages in processing. The process to convert intensity to transmission includes finding and subtracting a background signal, then normalizing such that the unattenuated signal is equal to one. The transmission through the 50 micron aluminum fiducial is 0.53. The final corrected signal shows the unattenuated transmission is $T = 1$ and the fiducial transmission is $T = 0.53$

signal is divided by the value of the unattenuated region with the background correction. Figure 4.18 shows a lineout of signals through this correction process.

The result of this correction process yields a transmission signal, shown in Fig. 4.19. Due to the cylindrical symmetry, an Abel inversion can be used to calculate the density of the liner wall. However, the transmission values must first be converted to areal density (kg/m^2) through,

$$\rho_{\text{areal}} = -\frac{ln(T)}{\kappa} \tag{4.4}$$

where T is the transmission, and κ is the opacity of the liner material (Parylene-N) to the 8040 eV photons. Averaging across multiple pixels in the axial direction is done to reduce noise in the areal density and ultimately the noise in density after applying the Abel inversion. The result of

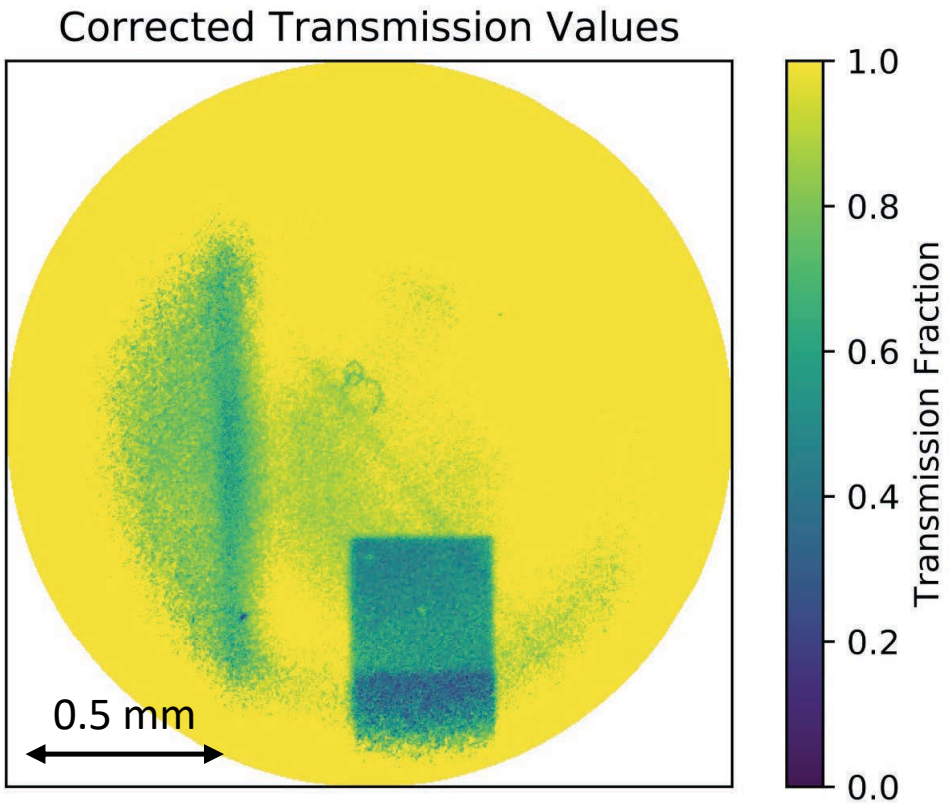

Figure 4.19: Radiographic image converted to transmission for Omega EP shot 36785. The wall liner material (Parylene-N) and the fiducial material (Al) act to block photons and reduce the signal. This reduction in transmission is shown here for the wall on the left and fiducial jutting out from the bottom.

this smoothing is shown in Fig. 4.20. Once the areal density is calculated using Eq. 4.4, an Abel inversion is applied determine the volume mass density of the liner wall as a function of radius.

The radial distance from the target is determined using the location of puncture holes in the fiducials that are at a known distance from the liner. The fiducial holes were not visible in the radiograph at $t = 10$ ns. This is likely due to the target being rotated a bit from the intended location, causing the fiducial to be out of focus. Instead, the radial position is determined by setting the outer edge of the density profile to the location of the outer surface of the initial target wall. The outer edge of the target is not expected to have moved much in 10 ns, and the width of the experimental density curve matches the expected target wall thickness of 0.1 mm. Lineouts from the $t = 10$ ns case is shown in Fig. 4.21.

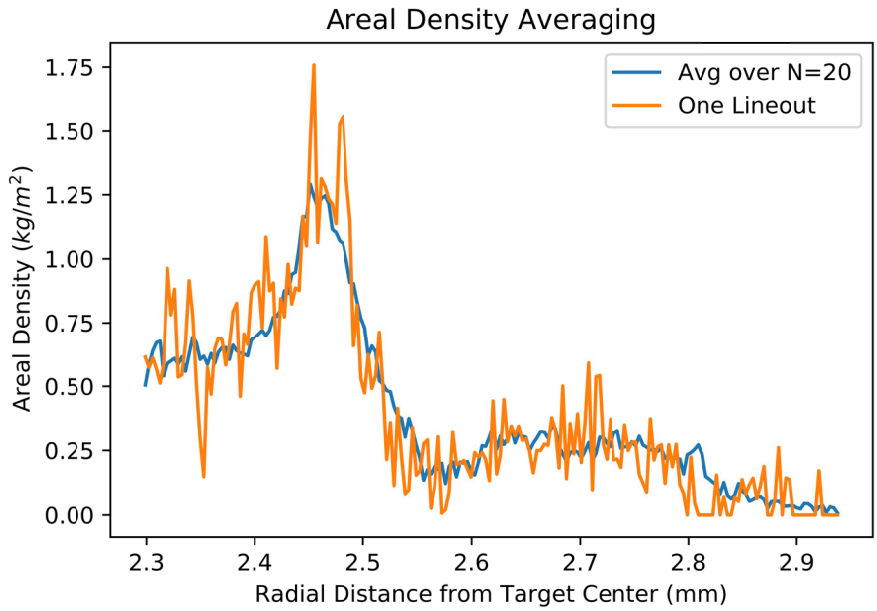

Figure 4.20: To reduce the noise in the areal density and ultimately the noise in the density calculated from the Abel inversion, the areal density is averaged across 20 pixels axially.

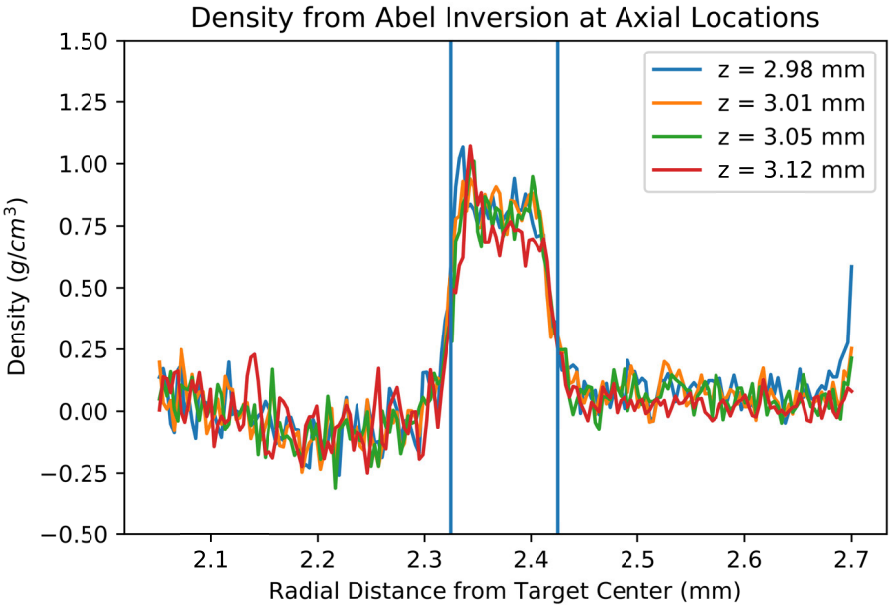

Figure 4.21: Radial lineouts of the liner density taken at various axial locations. The distance between the two vertical blue lines is 0.1 mm. This corresponds to the original wall thickness. The offset timing for this plot is 10 ns. This agrees with the 4ω probe data that says the liner has yet to move at 10 ns.

There are a few important things to note from Fig. 4.21. First, the distance between the two vertical blue lines is 0.1 mm. This is equal to the initial target wall thickness. Second, the offset timing for this shot is 10 ns. This agrees with the 4ω probe data that says the outer surface has barely begun to move at 25 ns. If the outer surface has barely moved at 25 ns, it should have moved even less in 10 ns. Third, the density found here is roughly the density of the wall material. Here, the density in the plateau of the curve (where the density of the wall is yet to be impacted by the shock/compression wave) is 0.8 g/cm^3, while the density of the Parylene-N wall material is quoted to be 1.01 g/cm^3. This difference between the density found from the radiograph processing and the actual density corresponds to an error of roughly 8%. So, there is about a +/-20% uncertainty in these density calculations. There are many steps to convert the radiograph signal intensity to density. Sources of error likely come from converting the intensity to transmission. While the shape of the Cu K-α x-ray beam profile is corrected for, in the majority of the radiographs, the fiducial is located outside the peak of the beam profile, in regions of low signal level, where the correction factor and error are higher.

Plots of the liner density as a function of radial distance from the axis of the cylindrical target for all shots in this campaign are shown in Fig. 4.22. These profiles can be integrated in the radial direction to test how well the liner mass was conversed in the radiographic processing.

For the initial conditions of the experiment, the mass of the liner is calculated to be 15.7 mg. The mass of the liner determined from the density profiles in Fig. 4.22 is 12.9, 14.5, 16.1, and 11.4 mg for the shots with timing offsets of 10, 20, 30, and 35 ns, respectively. The density profiles were cropped to just what is shown in Fig. 4.22 to reduce the impact of the nonphysical negative density tails. These negative densities could explain some of the observed reduction in experimentally calculated mass. The only case with elevated mass is at $t = 30$ ns. Further analysis shows that this case appears shifted in radial space. This would increase the calculated mass because the experimental mass is calculated from,

$$M = \int_{r_i}^{r_o} \rho(r) \cdot L \cdot 2\pi r \cdot dr, \tag{4.5}$$

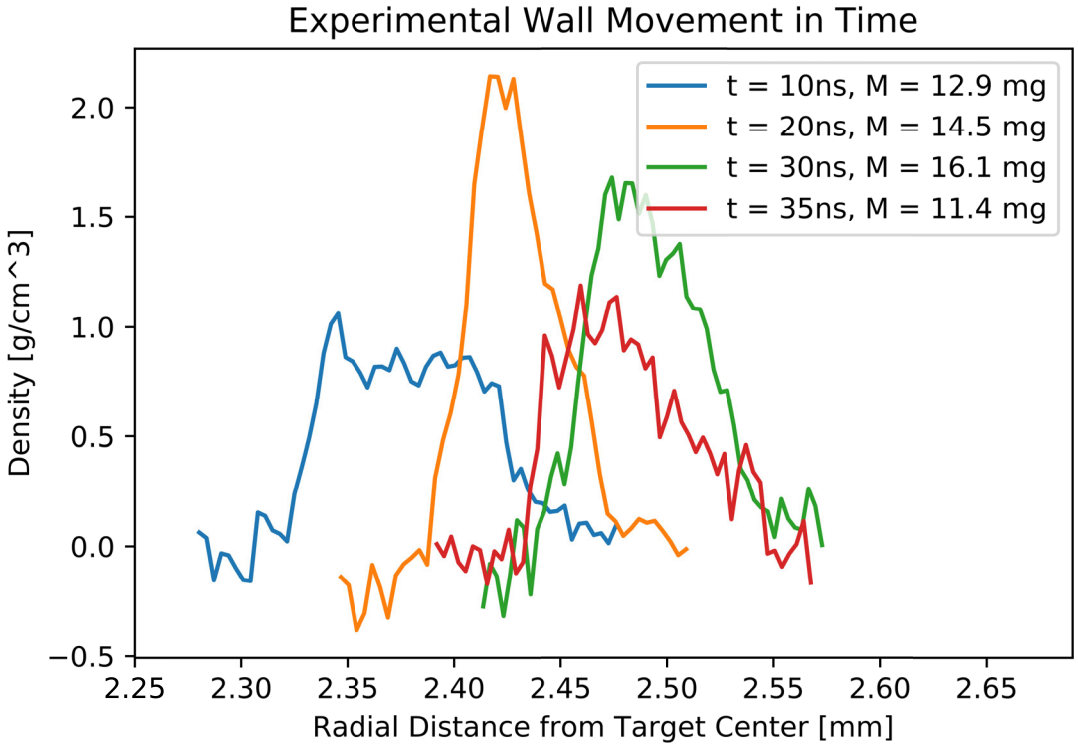

Figure 4.22: Radial density profiles extracted from the radiographs of Omega EP shots 36794, 36790, 36792, and 36785. As the shocks move through the wall, they compress the liner (resulting in increased density). After the shocks pass through the wall, the material begins to spread out away from the target axis. The masses calculated from the experimental density profiles are shown. Note that the resolution of the experimental system was calculated to be 50 μm, which factors into the radial distance of these density profiles.

where $\rho(r)$ is the density of the liner, L is the target length (10 mm), and r is the radial location. For this $t = 30$ ns case, puncture holes in the fiducial (intended to determine the experimental location for the experiment) were not visible in the radiograph. Therefore, the edge of the fiducial had to be used to relate the radiograph to a radial position. However, there is a 50 μm resolution associated with the radiography setup (see Appendix A for more details of this calculation). Thus, there is a 50 μm uncertainty in determining the absolute position of the fiducial edge. The density profile can be shifted along the radial axis to allow for mass conservation as shown in Fig. 4.23. Using the conservation of mass to adjust the radial location of the density profile shifts the $t = 30$ ns curve radially inward towards axis of the target. Before shifting the location based on mass conservation (shown in Fig. 4.22) the wall material appears to expand radially outward from $t = 20$ ns to $t = 30$ ns. Then the wall appears to move radially back towards the target center from $t = 30$ ns to $t = 35$ ns. The wall is expected to continue expanding outwards. There is still some error in this mass conservation method as shown by the lack of wall expansion from the $t = 20$ ns to $t = 30$ ns case. However, using the mass conservation instead of the fiducial edge placement seems to produce a more physical result.

The experimental density profiles can be compared with corresponding density profiles from the HYDRA simulations (courtesy of M. Weis at SNL). Figure 4.24 shows the liner density at $t = 10$ ns. The experimental density profile at $t = 10$ ns matches the shape of the HYDRA simulation at $t = 10$ ns. The density peak at the inner surface of the wall is experimentally observed. This is from the initial shock entering the wall. There is a discrepancy of amplitude between the experimental and simulated density for this $t = 10$ ns case. As mentioned above, this is likely due to the many steps involved to convert the raw radiographs to density profiles. The lower density amplitude, determined experimentally, corresponds to the lower than expected integrated mass amounts shown in Fig. 4.22.

As time progresses, the wall begins to compress and move further radially outward. Figure 4.25 shows the liner density at $t = 20$ ns. The experimental profile does not show as sharp of a density jump (in the middle of the wall) as that seen in the simulated profiles at 20 and 22.5 ns. There

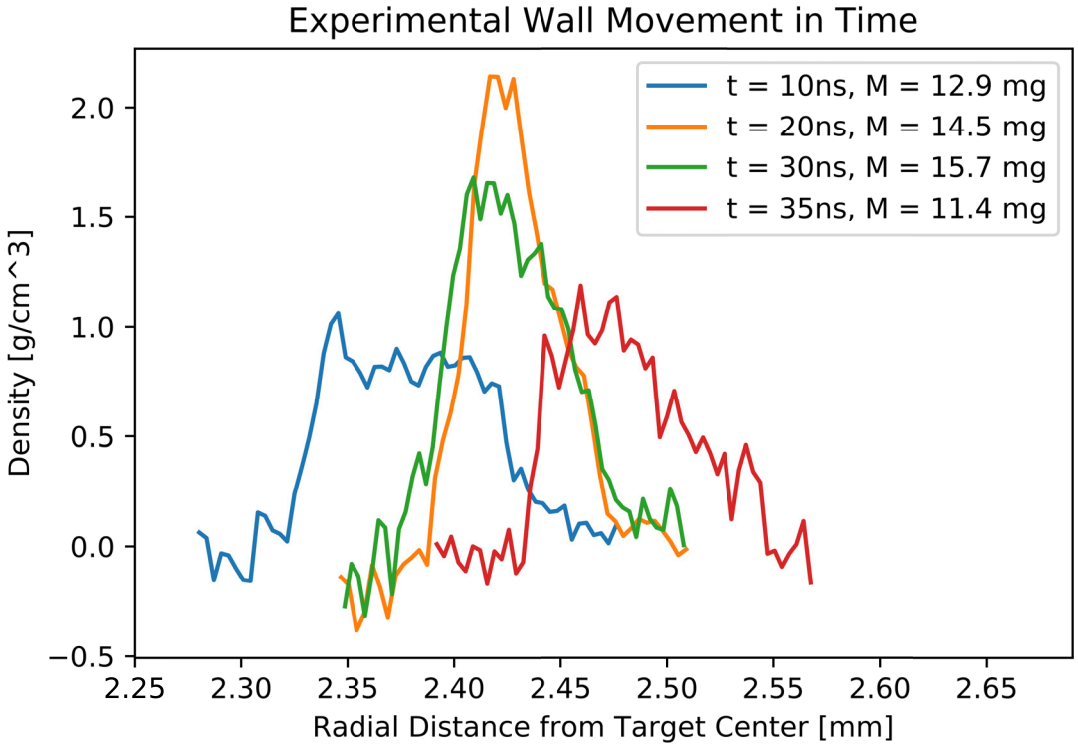

Figure 4.23: Radial density profiles extracted from the radiographs of Omega EP shots 36794, 36790, 36792, and 36785. In Fig. 4.22, the fiducial edge to determine the location of the $t = 30$ ns case. Here, the wall mass conservation is used to determine the location of the $t = 30$ ns case. Using this mass conservation provides a more physical result than the fiducial method used in Fig. 4.22that seems to have the wall moving back towards the target axis rather than continuous expansion as expected.

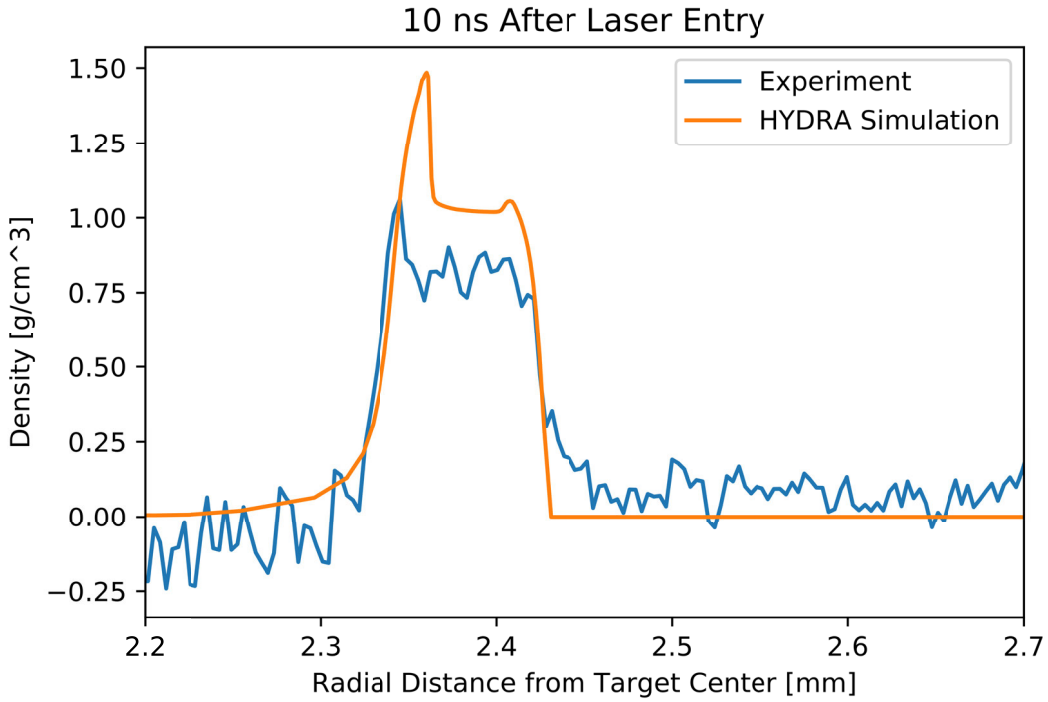

Figure 4.24: Radial density profile extracted from the radiograph of Omega EP shot 36794 (with a time offset of 10 ns) compared with radial density profiles from a HYDRA simulation The initial liner density was 1.01 g/cm^3 for the experimental liner material and the simulation. The experimentally produced density profile is about 20% less than expected density. This is likely due to the many steps involved to convert the raw radiographs to density profiles. Note that the the initial wall compression near the inner surface of the liner is observed in both the experiment and in the simulation.

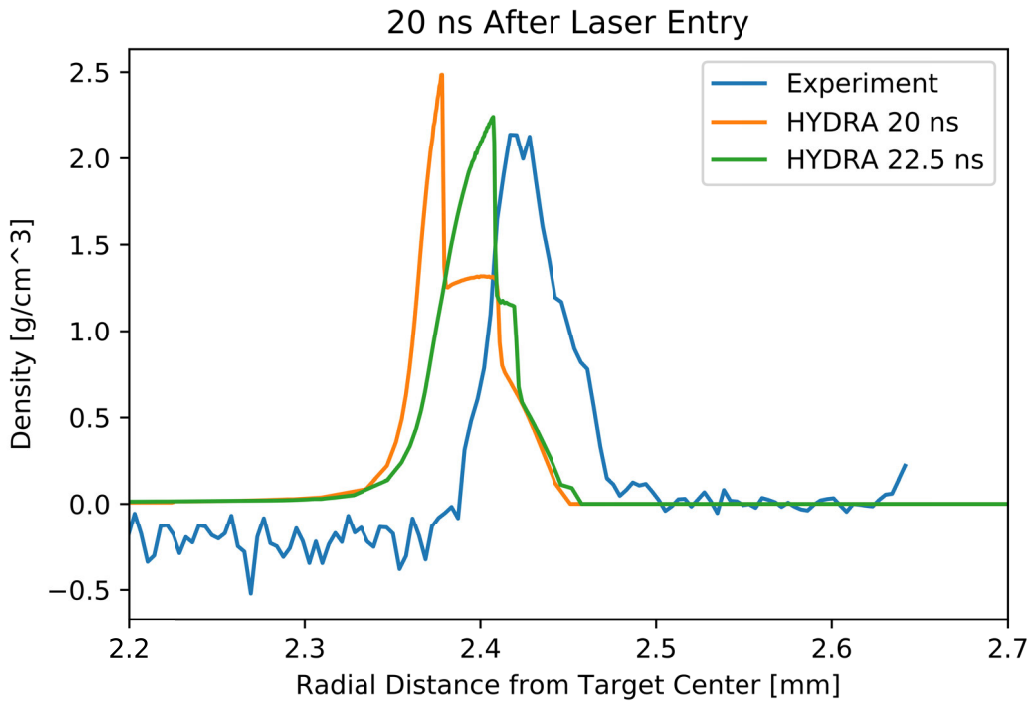

Figure 4.25: The radial density profile extracted from the radiograph of Omega EP shot 36790 (with a time offset of 20 ns) compared with radial density profiles from a HYDRA simulation (with time offsets of 20 and 22.5 ns). The experimental profile best matches the 22.5 ns simulated profile. This indicates the experimental wall could be moving faster than simulated. This could potentially be from a stronger experimental second shock or a smaller experimental mass than simulated/predicted. The compressed liner can been seen reaching a peak density of 2 times the original liner density in both the experiment and in the simulation.

does appear to be a roughly half-peak density region towards the outer edge of the liner wall in the experimental density profile. This is similar to the simulated profile at 22.5 ns. This indicates the experimental wall is moving faster than predicted in simulations. This could be due to the second shock being stronger than predicted, or if the mass of the target was lower than calculated from the given density of the wall material used. The experimentally calculated wall mass from Eqn. 4.5 (shown in Figs. 4.22 and 4.23 indicate the experimental mass might be lower. If the mass is lower, the wall would expand quicker. A peak density of 2 times the initial liner density is observed in both the experimental and simulated profiles as the second shock moves through the compressed liner wall.

Figure 4.26 compares the experimental density profiles for $t = 30$ ns with profiles from the

HYDRA simulation and includes a black vertical line at the location of the edge of the wall experimentally determined using the 4 ω probe measurements. Originally using the edge of the fiducial to determine the radial position of the curve produced a substantial radial offset observed between the experimental and simulated profiles. The radial offset in the profiles extracted from other radiographs (taken from other Omega EP shots with different offset times) is not as severe. However, as in the $t = 10$ ns case, the holes in the fiducial were not visible in the $t = 30$ ns radiograph. Therefore, the edge of the fiducial had to be used to relate the radiograph to a radial position. However, there is a 50 μm resolution associated with the radiography setup. Thus, there is uncertainty in determining the absolute position of the fiducial edge. So, the discrepancy in the radial distance between the experimental profile and the simulated profiles is likely from this resolution limitation. However, as shown in Fig. 4.23, the radial position can also be determined using the mass conservation of the wall material. Figure 4.26 shows that the mass conservation method of determining the radial position matches closely to the predicted density profile position. It appears the 2.5 ns offset observed in the $t = 20$ ns case is not present in the $t = 30$ ns case. Additionally, as shown in Fig. 4.26, the experimental wall has a higher density and is more compressed. This could mean the second shock is stronger than simulated. Also, the location of the edge of the wall found experimentally from the 4ω probe measurements aligns closer to the experimental wall edge than the simulated wall edge. The consistency amongst the two types of experimental results could indicate a discrepancy between experiment and simulation.

Figure 4.27 shows the experimental density profile at $t = 35$ ns. It is even more apparent in this case that there is a sharp density jump at the inner surface of the liner. This jump is also present in the $t = 30$ ns case of Fig. 4.26. The black vertical line shows the location of the wall edge determined experimentally using the 4ω probe. This lines up with the experimental and simulated wall edges. The peak experimental liner density is higher than the peak simulated liner density (the same as in the $t = 30$ ns case. This result is significant because the sharp jump and higher density at $t = 30$ and 35 ns could mean that the second shock wave in the experiment is stronger than simulated/predicted. A stronger shock wave could affect the amount of material ejected from

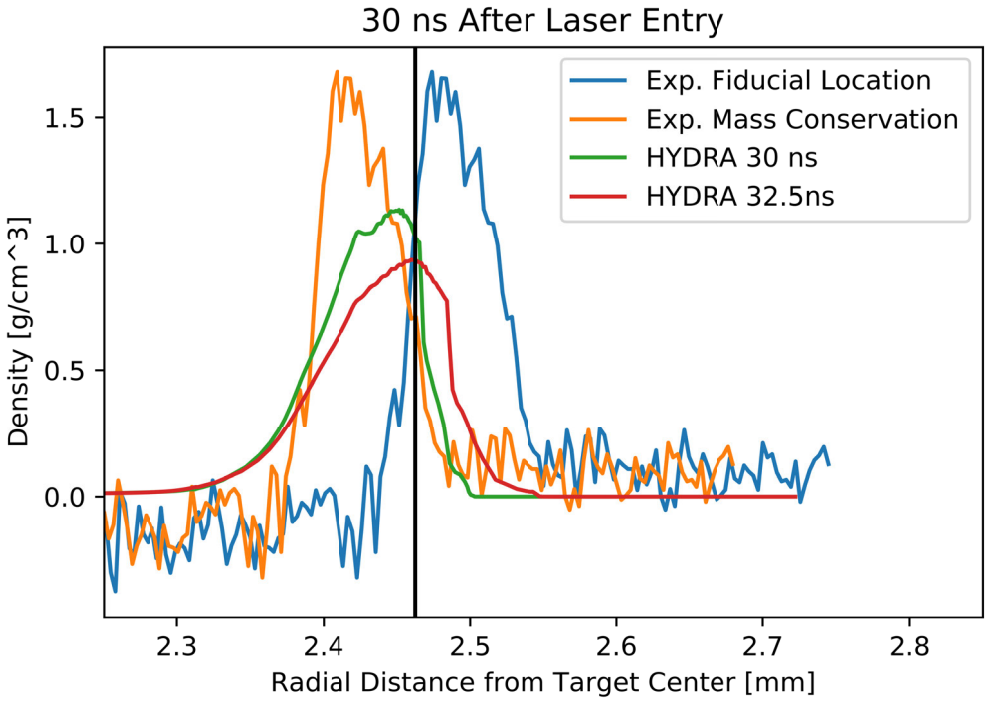

Figure 4.26: Two radial density profiles extracted from the radiograph of Omega EP shot 36792 (with a time offset of 30 ns) compared with radial density profiles from a HYDRA simulation (with time offsets of 30 and 32.5 ns). The radial position of the experimental profiles were determined using a fiducial edge tracking method and a wall mass conservation method. The mass conservation method produces a density profile more similar to the simulated density profile. The black vertical line represents the experimentally determined wall edge from the 4ω probe measurements. This 4ω edge aligns closer to the experimental wall edge than the simulated wall edge shown here. Additionally, the peak density is larger in the experimental profile than in the simulated profiles.

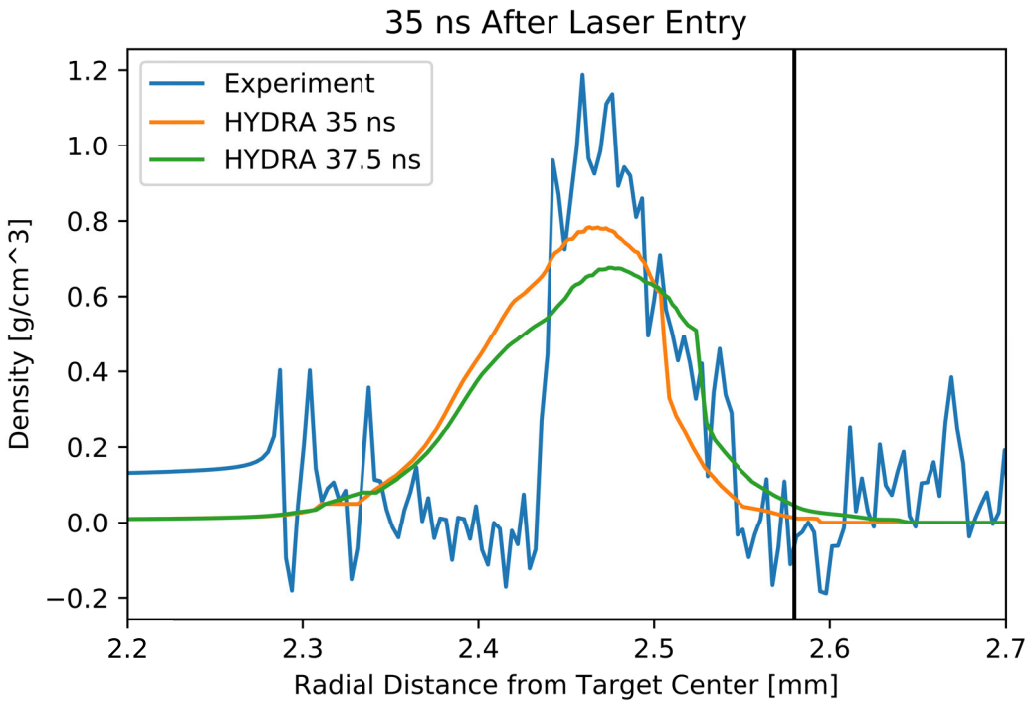

Figure 4.27: The target liner density at 35 ns is compared to HYDRA simulations. The black vertical line shows the location of the wall edge determined experimentally using the 4ω probe. This agrees with the experimental and simulated wall edge locations. This experimental density continues to decrease in peak value and spread out away from the target axis. However, there is a sharp density jump at the inner liner not seen in the simulation. The experimental liner appears to be more compressed and less spread than predicted. This density jump coupled with the lower than actual mass calculated for this time could mean that lower density material from the inner liner has been kicked off from the wall and is mixing into the fuel.

the liner's inner surface and mixed with the fuel. If true, this could impact MagLIF performance.

In closing this chapter, in the early-time case of $t = 10$ ns (see Fig. 4.24) the wall density is lower than expected from the reported liner density of the wall material and the simulated density. However, at later times ($t = 30$ and 35 ns), the compressed liner density has become higher in the experiments than in the simulation (see Figs. 4.26 and 4.27). It appears that the liner material is not spreading out as much in the experiments as in the simulations. These observations are important as the amount and location of the wall material can impact MagLIF performance. Additional experiments and simulations could provide more insight into this discrepancy. Resolving these discrepancies is important, as the amount and location of wall material could potentially impact

MagLIF performance.

CHAPTER 5

Conclusions

Two studies pertaining to the laser preheating stage of MagLIF were undertaken for this dissertation: a Laser Gate proof-of-concept demonstration and a liner wall movement study conducted on the Omega EP laser at the University of Rochester's Laboratory for Laser Energetics.

The Laser Gate method aims to remove the LEH window from a MagLIF target just before the preheating laser beam is applied. The idea is to increase the energy coupling from the preheating laser to the fuel, thereby increasing MagLIF fusion yield. This dissertation demonstrated a proof-of-concept for the laser gate platform and design work for a platform to complete further studies (see Appendix E). This work demonstrated the LEH window moving up and out of what would be the MagLIF preheating laser path on the time scales predicted by a simple model of window opening dynamics. The window appeared to have opened cleanly, with no apparent debris, and remained as one piece throughout the experiment. The nichrome wire used to weaken the window material remained in place long enough for it to not interfere with the laser entrance path and thus be compatible with integrated MagLIF experiments. Efforts at SNL continue to study the removal of the LEH window [19].

To study liner wall movement during the laser preheating stage, an experimental platform was developed for Omega EP. This platform was used to track the liner material as the target fuel heats and sends shock waves through the liner walls. A 4ω probe tracked the outer surface of the liner wall as a function of time, and a spherical crystal imager (SCI) captured radiographs that were used to track the density profile of the liner wall as a function of time.

From tracking the outer surface, it was found that earlier in time, the liner had greater displace-

ment closer to the LEH. As time increased, the displacement deeper into the target (farther from the LEH) was greater. The outer surface moved roughly as predicted by HYDRA simulations, however, the experimental axial location dependence on wall movement was opposite from predicted. The wall is expected to move less deeper into the target, but in the experiment, the wall moved more deeper into the target. Also, the wall moved more and faster than predicted. However, the $t = 30$ ns and $t = 35$ ns wall edge locations found from the 4ω probe agreed with the edge of the wall locations in the corresponding density plots from the radiographs.

The density profile of the liner wall was experimentally determined from radiographs and compared with simulations. The wall was seen compressing and expanding mostly as predicted. However, questions about the lack of a lower density region at the inner surface of the liner remain. This is critical to understanding the potential for wall material to mix into the fuel and degrade fusion yield. Something like a coating on the inner surface of the target might aid in understanding more about this mix and the sharp density jump observed at the inner liner surface.

The platform for studying the laser preheating stage of MagLIF on the Omega EP facility has now been established. The encouraging results obtained from this work help motivate the continued development and expansion of this platform. Future studies are ongoing, and the following recommendations could allow for even more meaningful data collection moving forward.

A few simple target and fiducial modifications could improve the analysis. The 4ω probe could use a more robust fiducial to determine scale size. In this work, the copper ring fiducial was only slightly visible. The wall movement is very important to understand so a simple scale size fiducial visible in the 4ω field of view would allow better accuracy of wall movement. Additionally, the presence of the aluminum strip fiducial did not seem to have an impact on wall movement at the times considered. Therefore, the viewing window could be adjusted to include more of the fiducial to provide more input for the transmission calculations. Additionally, methods could be incorporated to better handle the rotation and/or tilt introduced by the viewing angle. For example, it may be possible to include a spherical fiducial to determine the scale size. This way, regardless of how the target is rotated or tilted, the scale size can still be easily determined. Additionally, the rotation/tilt

of the target could be better understood and characterized.

Finally, the field of view available in the diagnostics is very limited when compared to the size of the targets. Finding a way to size down the experiment might prove beneficial. While it is important to consider the physics of the laser depositing energy into the target on scales relevant to current MagLIF experiments at the Z Machine, smaller targets would considerably increase the amount of information gained from these experiments. The target chamber size puts a limit on the maximum field of view for the diagnostics. So the best way to view more of the target would be to decrease the target size. This would allow for the full length of the target to be seen by the 4ω probe and potentially help probe why the target wall moves differently at different axial positions. Also, it would be beneficial to see at least half if not the whole width of the target in the radiographs. This would allow for better density calculations from the Abel inversion and could also tell us more about the symmetry of the expansion.

If scaling the size of the experiment down proves to be difficult, future studies should consider probing other locations along the target wall to determine if the trends in behavior of target movement in relation to axial position occur at the midpoint of the target or at the end of the target body. Building upon the data could help understand some of the additional radial and axial variations in the wall movement.

It is important to understand the behavior of target components in the laser preheating stage of MagLIF. Target design improvements can be made to increase laser energy coupling to the fuel and reduce mix of target body material into the fuel. Additionally, understanding the physics of this preheating process becomes increasingly important when using simulations to scale the MagLIF platform to the larger facilities and higher yields necessary for ignition.

APPENDIX A

Radiograph Processing Beam Signal

Before the experimental radiographs can be used determine wall density and movement, the images must be analyzed to find the intensity profile of the imaging Cu K-α x-rays beam and spatial resolution of the diagnostic setup. A radiograph resolution image shown in Fig. A.1 was taken of a 20 micron thick gold mesh shown to scale in Fig. A.2. To correct for the profile of the beam, a spatial intensity map of the laser was created and then used as a correction in the experimental radiographs. Mesh edge assessment from this resolution image was also used to calculate the resolution capabilities for the system.

First, the resolution radiograph is rotated and cropped as shown in Fig. A.3. The resolution radiograph is shown with the scale cartoon in Fig. A.4 to demonstrate the field of view of the system. It is important to note that the field of view only includes the center of the mesh and the variance of the laser intensity profile is clearly visible in the field of view showcasing the importance of correcting for the beam profile.

The, size scale of the image is found. The coordinates of the center of the mesh strips are located (Fig. A.5) and compared to the known distance between the mesh strips of 0.75 mm. The distance between the the center of the strips is 154 pixels. This means that each pixel corresponds to 0.75mm/154 = 4.9 μm.

To find the laser intensity profile, first the mesh elements are removed from the image and just the unattenuated signal is considered Fig. A.6. Then, a line signal is fit to the remaining profile. Fig.A.7 shows lineouts of the resolution radiograph and its corresponding profile fit in both the vertical and horizontal direction. The fit must be done in one direction first then the other direction

second to fill the gaps from the wire removal in both directions. The first fitting is just in the vertical direction or just the horizontal direction as shown in Fig.A.8. Then the fitting in repeated in the opposite direction to the first fitting. This gives a total beam profile fit for each method of vertical then horizontal and horizontal then vertical. Fig.A.9 shows a complete beam profile correction for both methods. These methods produce very similar results, shown in Fig.A.10. The difference is calculated from the difference in methods divided by the average of methods then multiplied by 100 to find the percentage difference. Because the methods produce such similar results, the fit in the vertical and then horizontal direction is used in later analysis of experimental radiographs. The fit can also be used to normalize the original resolution mesh radiograph, shown in Fig.A.11. The result of this normalization is as expected. The beam profile is flattened such that the unattenuated signal corresponds to a transmission value around 1.

The radiograph of the mesh can also be used to find the resolution of the system. Fig.A.12 shows the locations of the lineouts shown in Fig.A.13 used to calculate the system resolution. The colors of the lineouts correspond to location lines. Each lineout is split into two lines corresponding to the resolution across each mesh element either to the right and left or top and bottom depending on the strip of mesh orientation. The resolution is determined by the distance it takes the intensity signal to rise from 10% to 90% of its peak value. The resolution is 50 μm in the vertical direction and 60 μm in the horizontal direction. Now, the beam intensity profile and the resolution can be used in the analysis of the experimental radiographs.

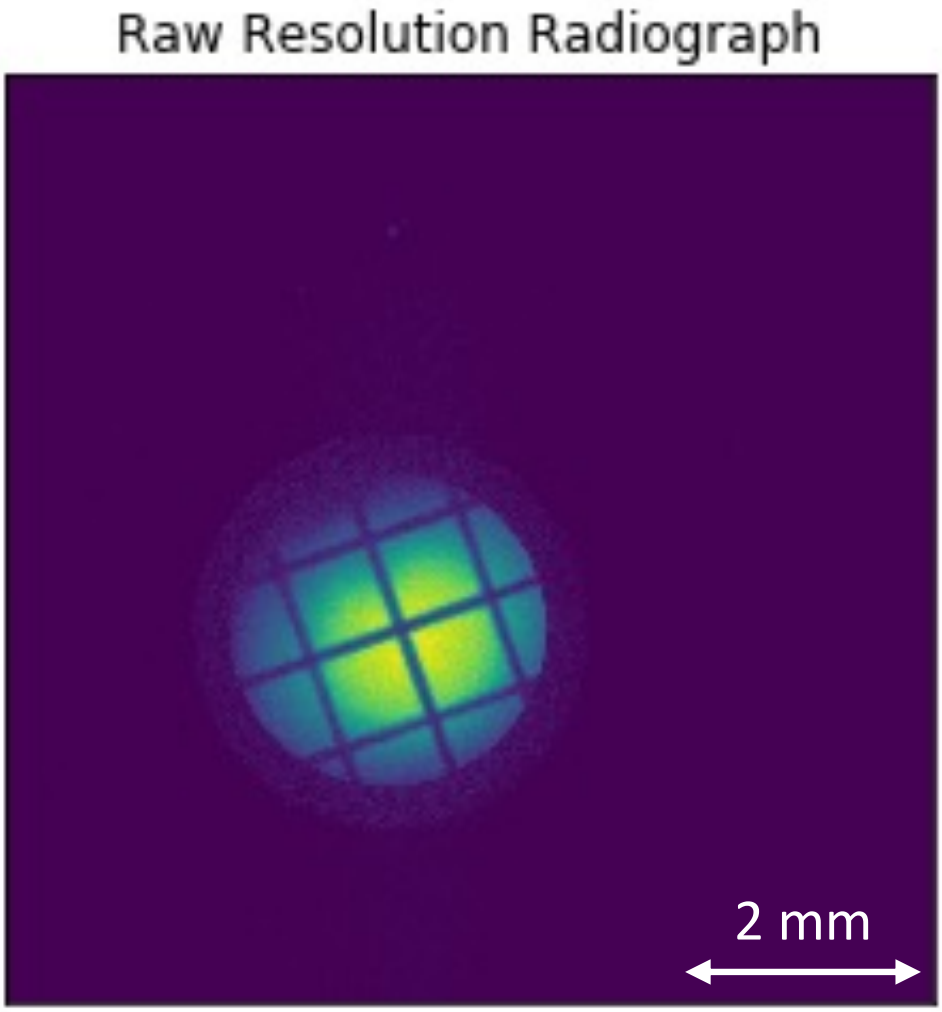

Figure A.1: The raw radiograph of the of a gold mesh resolution target of known thickness 0.02 mm and strip thickness 0.08 mm.

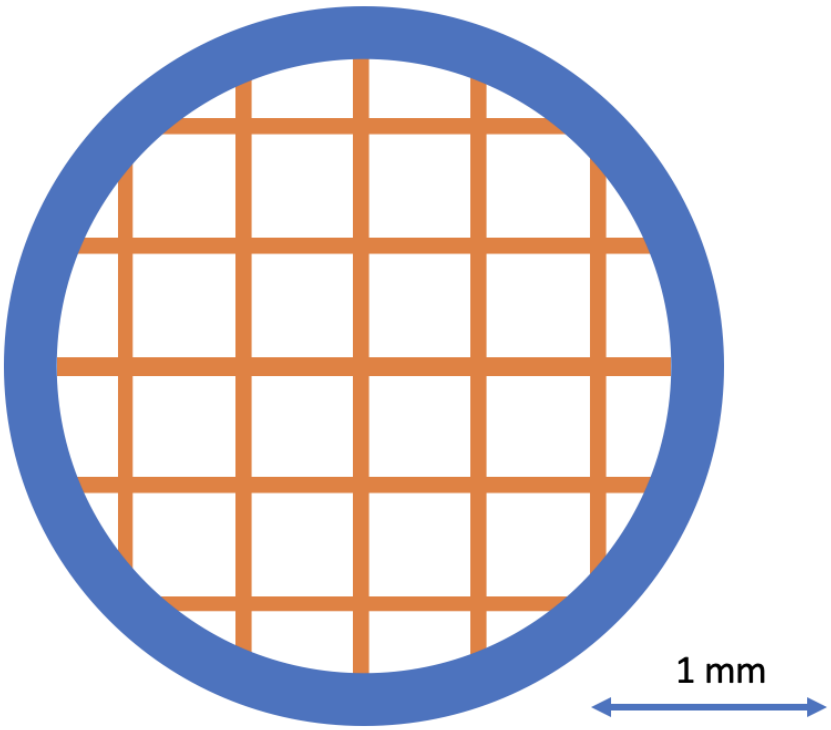

Figure A.2: A cartoon to scale representation of the gold mesh is shown. The dimensions are as follows: outer diameter of the ring is 3.05 mm, inner diameter 2.6 mm, mesh strip width 0.08 mm, mesh thickness 0.02 mm.

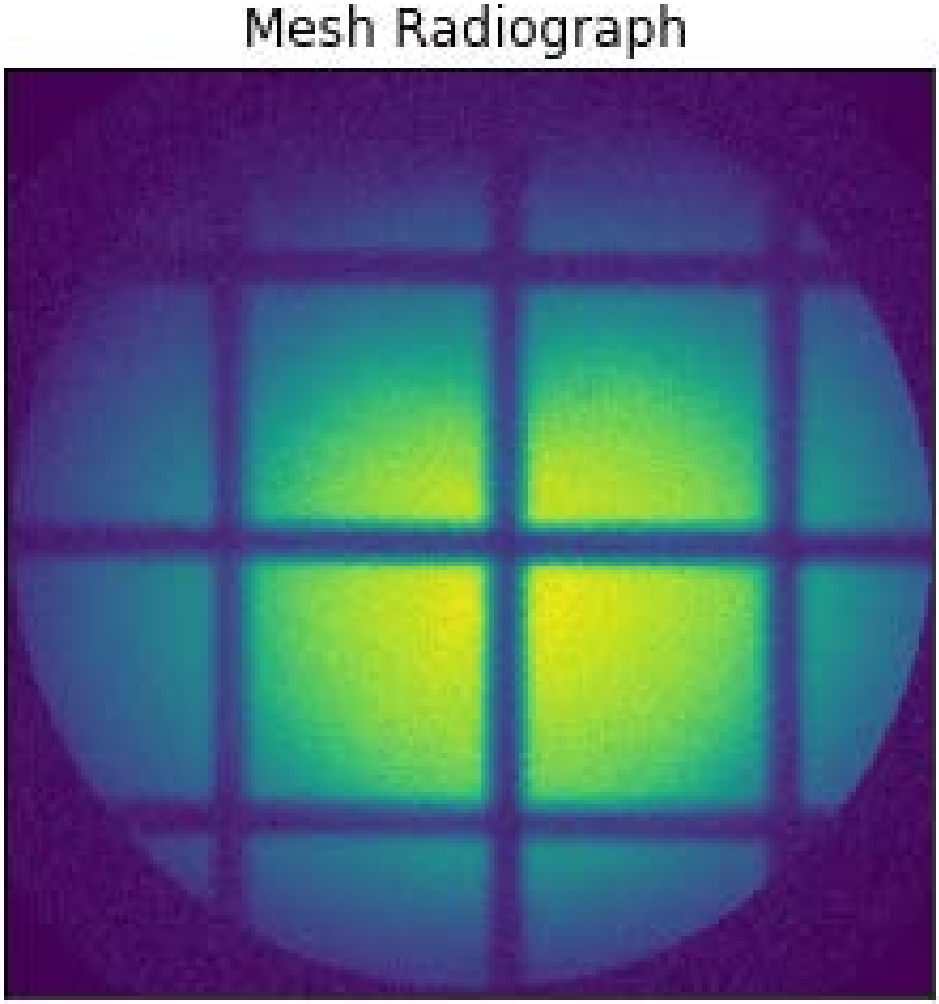

Figure A.3: The cropped and rotated radiograph of a gold mesh used to calculate the spatial resolution and the intensity profile of the system used to image the full integrated experimental radiographs.

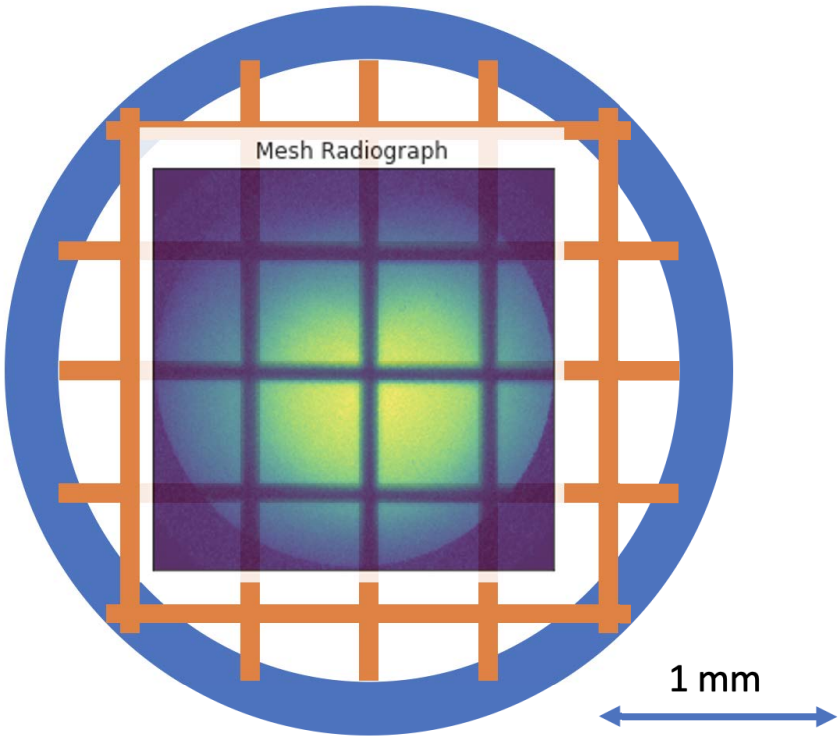

Figure A.4: The resolution radiograph is shown with the mesh target overlay. Note, the radiograph only captures the center of the mesh target and the beam intensity peaks sharply near the center of the mesh.

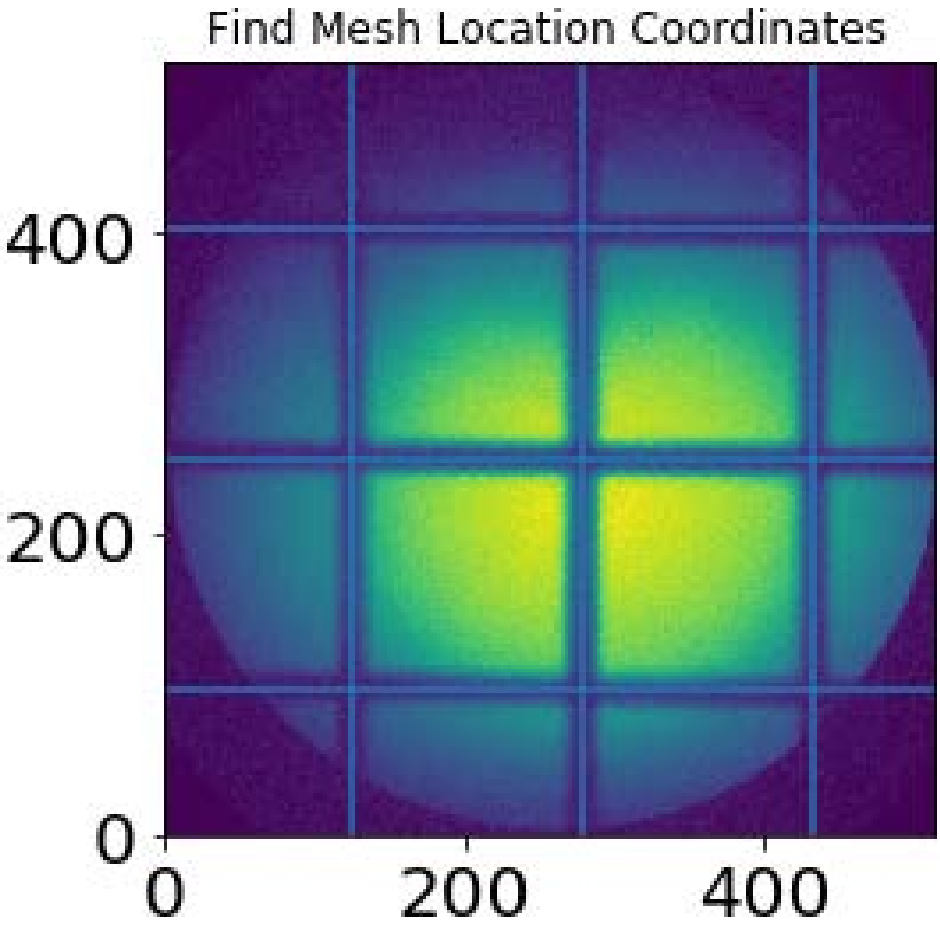

Figure A.5: The mesh location are at pixels x = 125, 279, and 433 and y = 96, 250, and 404. The distance between each mesh strip is 154 pixels. This value is used to spatially scale the radiograph.

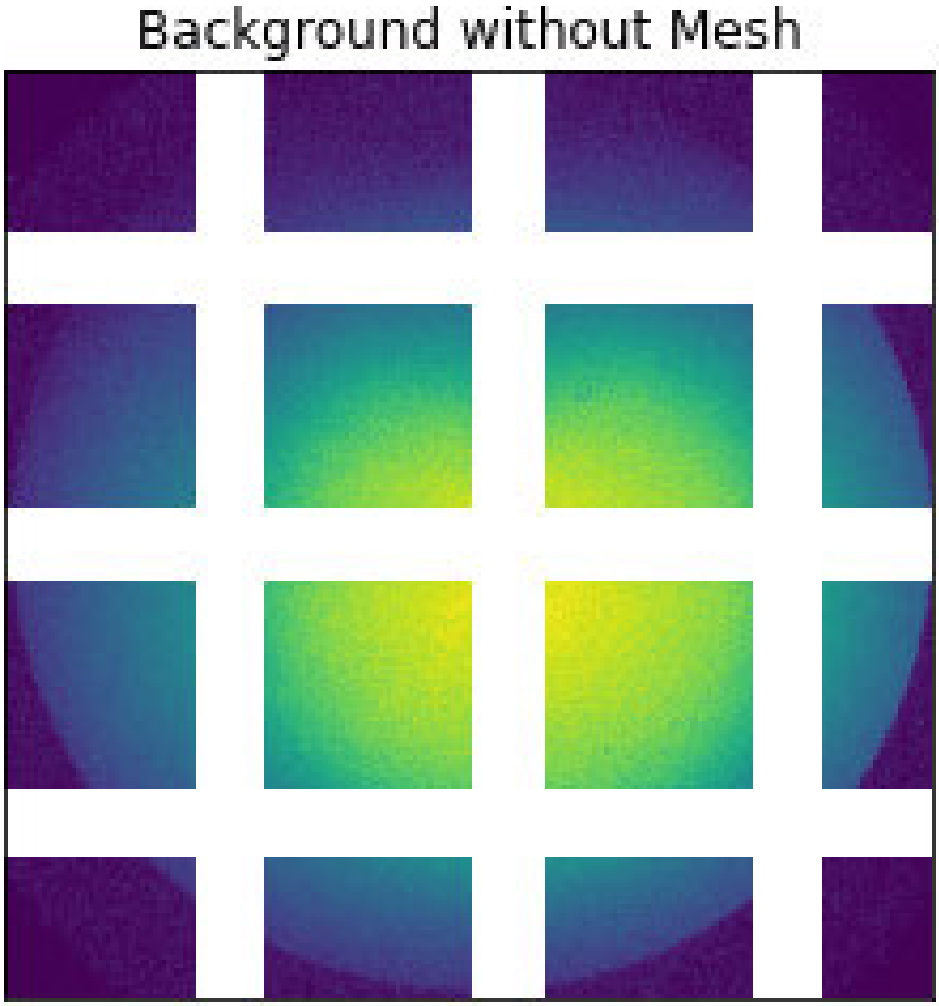

Figure A.6: The background mesh has been removed to analyze just the unattenuated laser signal.

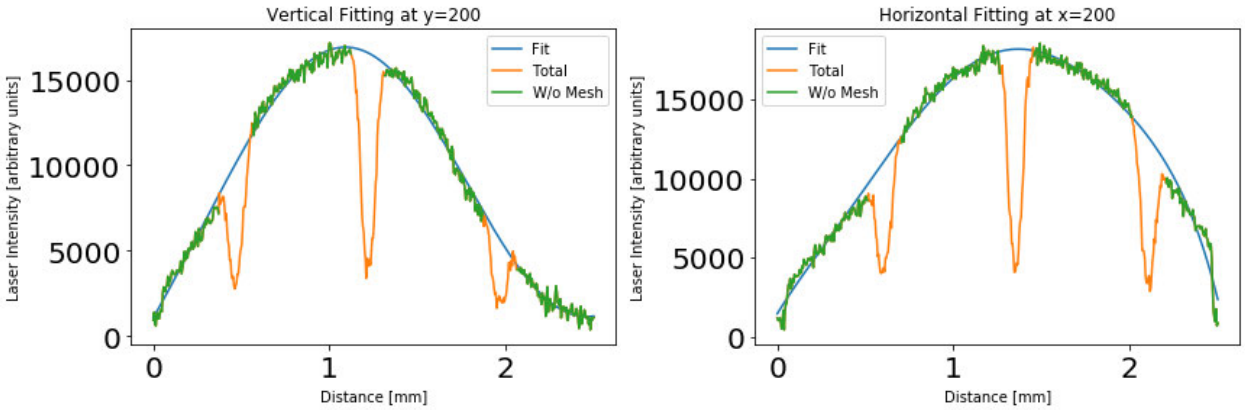

(a) (b)

Figure A.7: Lineout examples comparing calculated fits to raw data of the beam profile in both the vertical (a) and horizontal (b) directions.

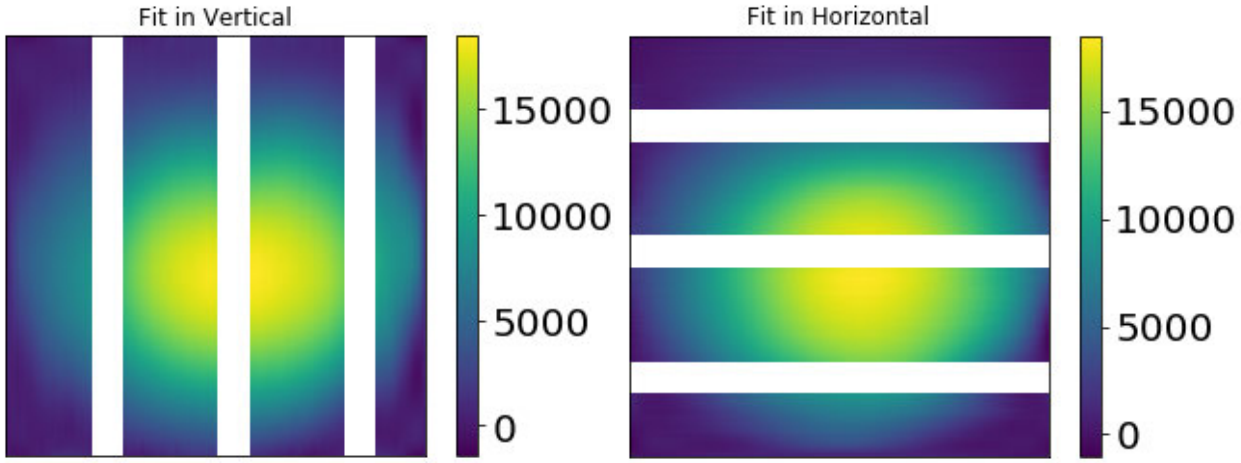

(a) (b)

Figure A.8: Fitting is done one direction at a time. This shows the first directional fitting in both the vertical (a) and horizontal (b) directions.

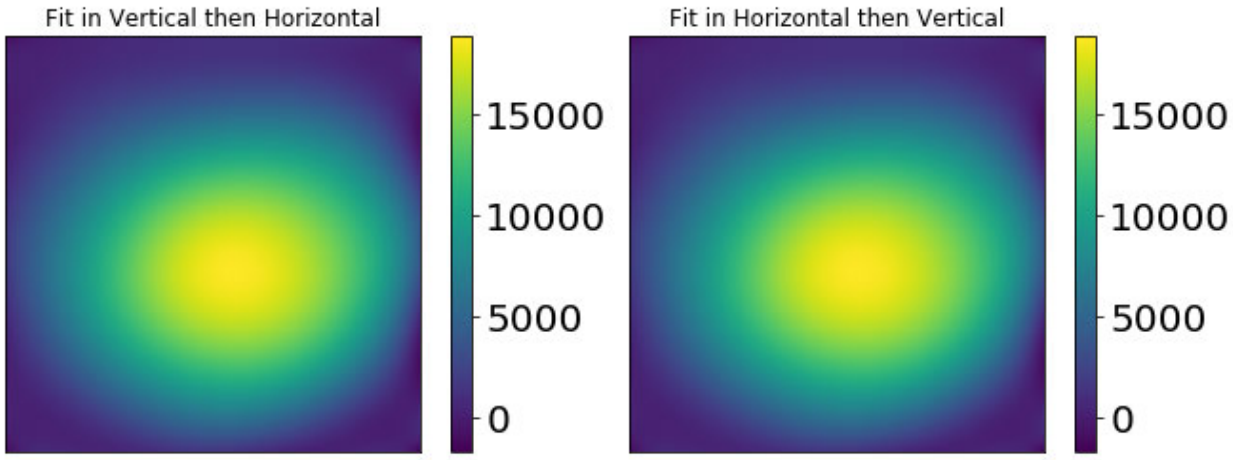

(a) (b)

Figure A.9: Fitting for the beam profile in both the vertical (a) and horizontal (b) directions is done to assess the beam profile.

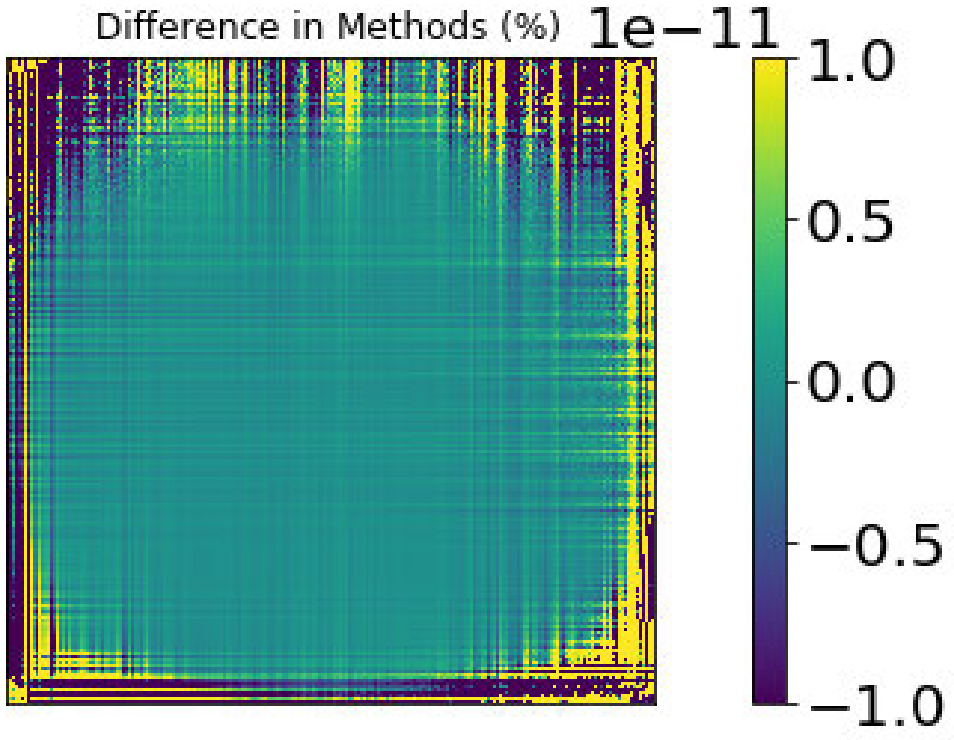

Figure A.10: The difference between the methods of fitting vertical then horizontal versus horizontal then vertical is shown to be very low. The percentage difference is on the order of 1^{-13}

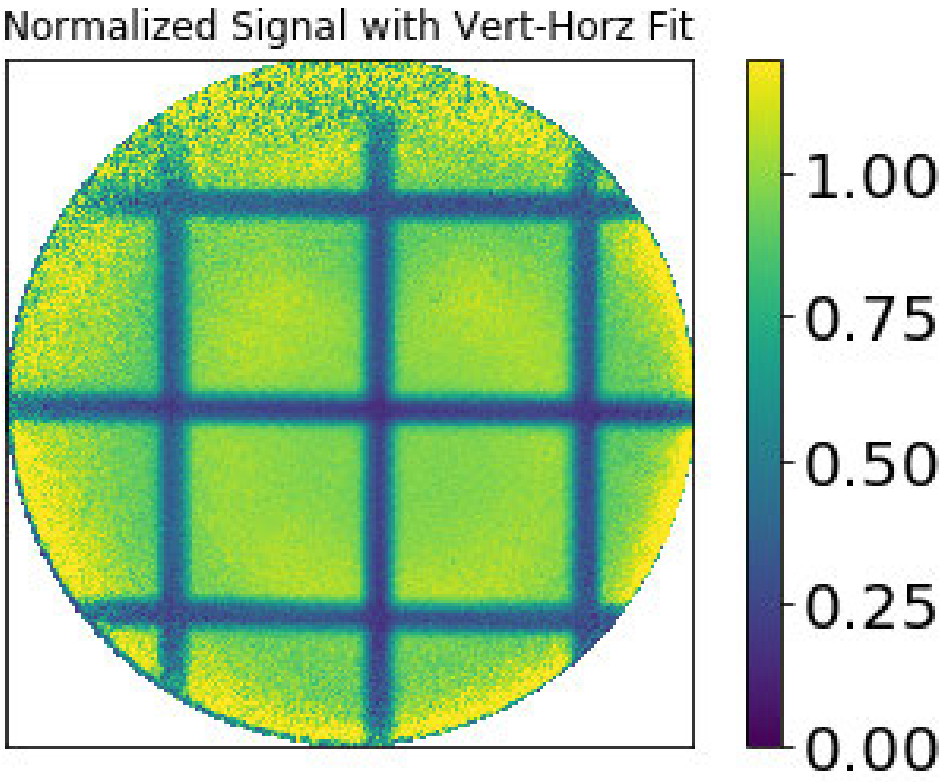

Figure A.11: The fit from Fig.A.9 (a) is used to normalize the original mesh radiograph resulting in a smoothed beam profile with a transmission near 1 of the unattenuated signal.

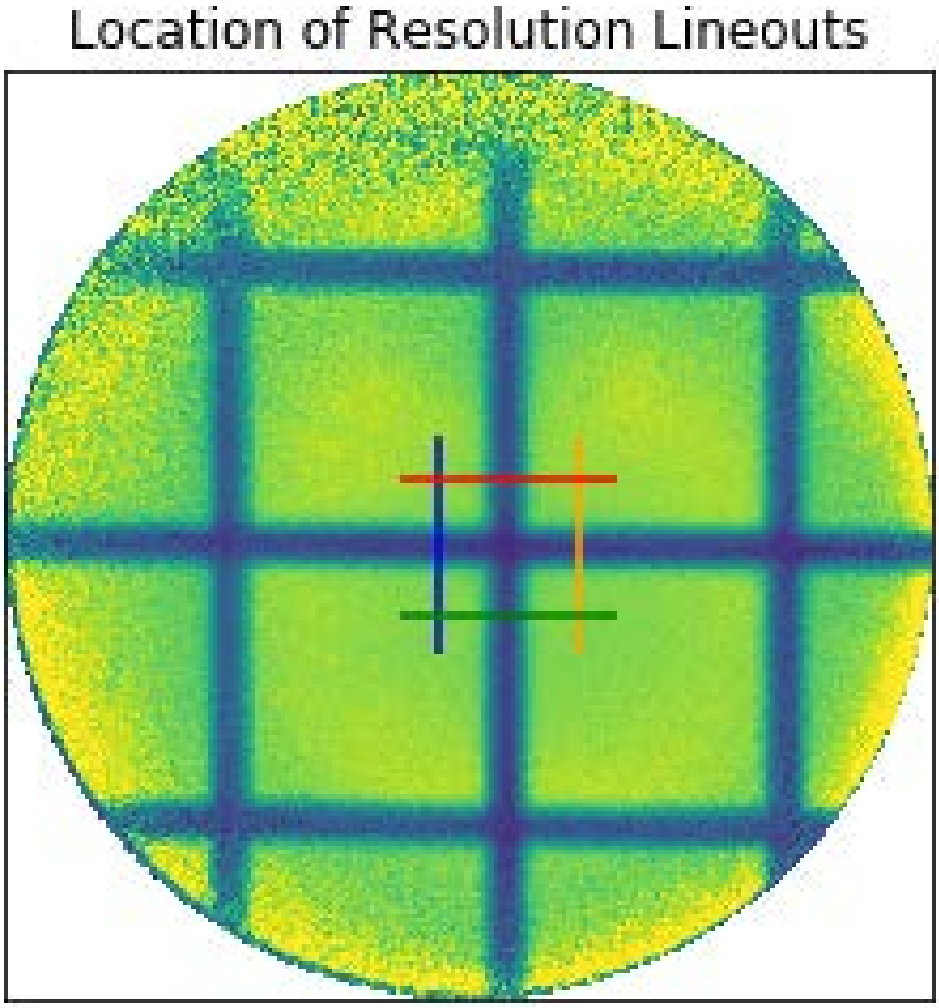

Figure A.12: Lineouts from normalized mesh are used to determine the system resolution.

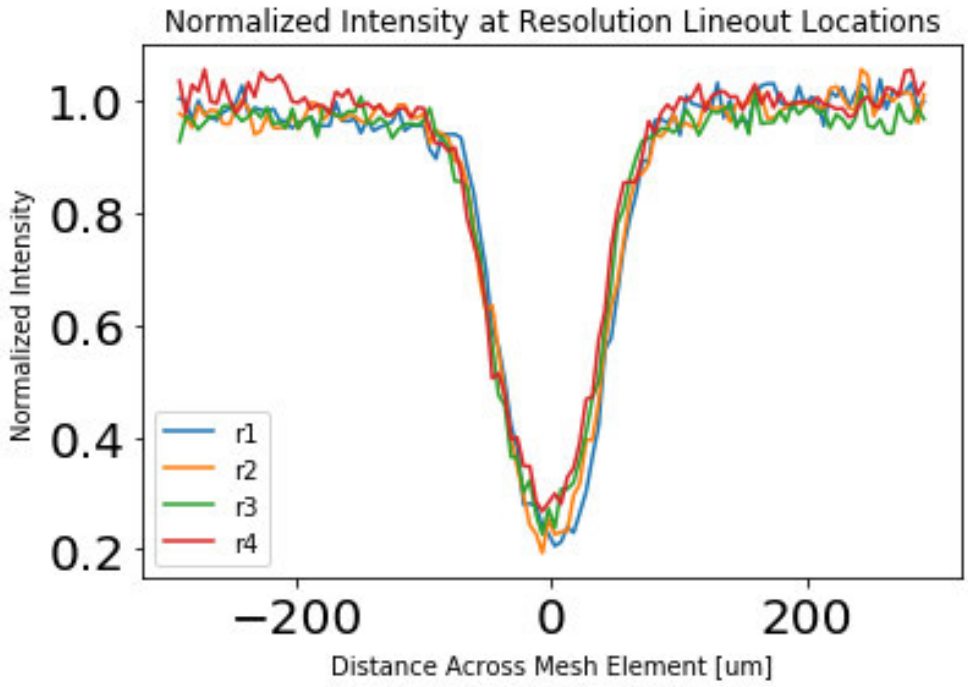

Figure A.13: The colors in these lineouts across mesh elements correspond to the color markings in Fig.A.12 with red and green being in the horizontal direction and blue and orange in the vertical direction.

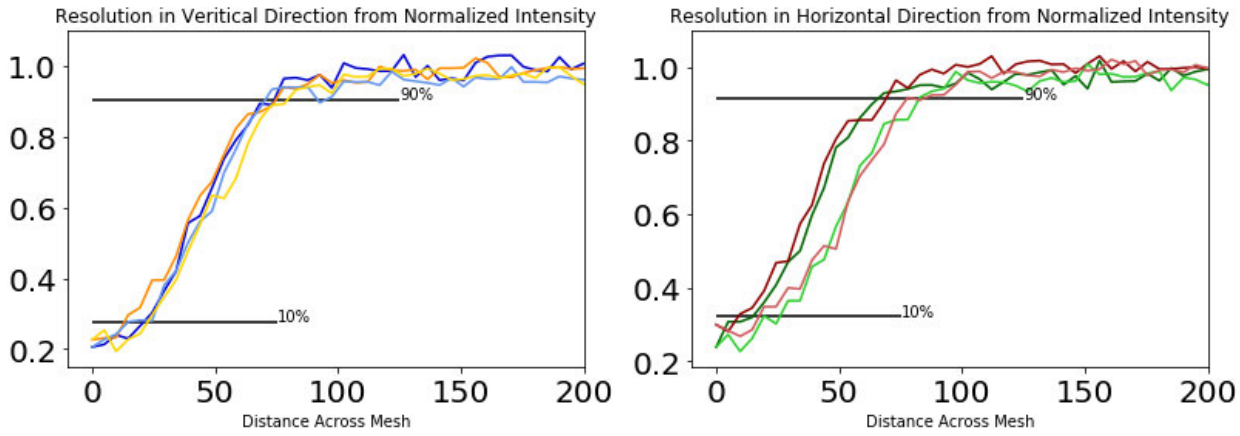

(a) (b)

Figure A.14: Lineouts across the edge of the mesh at different locations. The intensity rises from 10 % to 90% in 50 microns in the vertical direction (a) and 60 microns in the horizontal direction (b).

APPENDIX B

Omega EP Campaign Shot Parameters and Identifications

Shot Number	Omega EP: Shot ID	Omega EP: RID	Omega EP: Target ID	Shot Type	Configuration
1 (preshot)	36784	87063	MAGLIF-3Q22-MG23	4w preshot	primary
1	36785	85253	MAGLIF-3Q22-MG23	full	primary
2 (preshot)	36786	87062	MAGLIF-3Q22-MG29	4w preshot	secondary
2	36787	86332	MAGLIF-3Q22-MG29	full	secondary
3	36788	86623	MAGLIF-3Q22-MG35	resolution	primary
4 (preshot)	36789	87175	MAGLIF-3Q22-MG28	4w preshot	primary
4	36790	87078	MAGLIF-3Q22-MG28	full	primary
5 (preshot)	36791	87176	MAGLIF-3Q22-MG27	4w preshot	primary
5	36792	87096	MAGLIF-3Q22-MG27	full	primary
6 (preshot)	36793	87178	MAGLIF-3Q22-MG26	4w preshot	primary
6	36794	87097	MAGLIF-3Q22-MG26	full	primary

Figure B.1: Omega EP campaign data for shot type and identification information.

Shot Number	Beam 2/1 Offset (ns)	Beam 4/3 Offset (ns)	Beam 5 Offset (ns)	Rad Timing Delay (ns)	4w Timing Delay (ns)
1	40	5	30	35	25
2	40	15	40	25	25
3	40				
4	40	20	55	20	35
5	40	10	40	30	30
6	40	30	70	10	40

Figure B.2: Omega EP campaign data for laser beam timings.

Shot Number	Shot Pressure (psi)	2/1 IR Beam Energy (J)	4/3 UV Beam Energy (J)	Requested 2/1 Beam Energy (J)	Requested 4/3 Beam Energy (J)	Pulse Shape 2/1 (ns)	Pulse Shape 4/3 file type
1	140.91	666.2	3341.8	668	3300	15	ESS6010v001
2	141.94	446.3	3150.3	445	3300	10	ESS6010v001
3		1333.2		1323			
4	139.94	1337.8	3356.3	1323	3300	15	ESS6010v001
5	143.35	1347.5	3346.2	1323	3300	15	ESS6010v001
6	140.43	1331.8	3266.5	1323	3300	15	ESS6010v001

Figure B.3: Omega EP campaign relevant shot parameters.

Shot Number	Stalk Angle	Distance: fiducial to LEH flange (μm)	Distance: bottom hole to wall (μm)	Distance: bottom hole to LEH flange (μm)	Distance: top hole to wall (μm)	Distance: top hole to LEH flange (μm)
1	23.7	1584	366	2866	491	2738
2	24.3	1269	305	3411	426	3285
4	24.2	1497	331	2913	455	2784
5	22.6	1457	339	2931	460	2799
6	22.8	1612	354	2879	479	2752

Figure B.4: Omega EP campaign target holder stalk angle and relevant aluminum fiducial location information.

APPENDIX C

Raw 4 Omega Probe

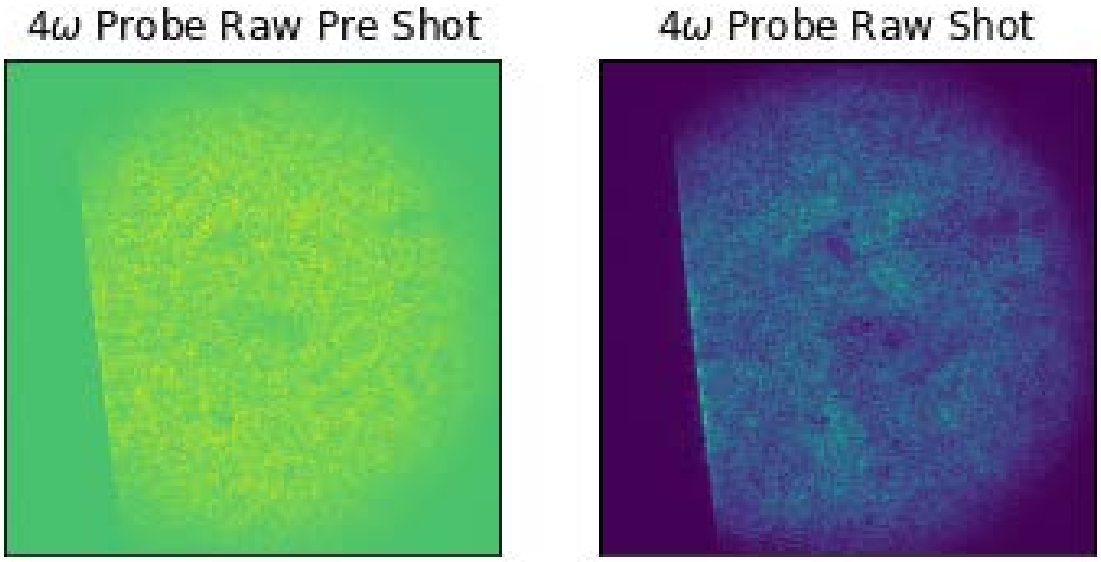

Figure C.1: Omega EP shot nums = 36784, 36785, t = 25 ns

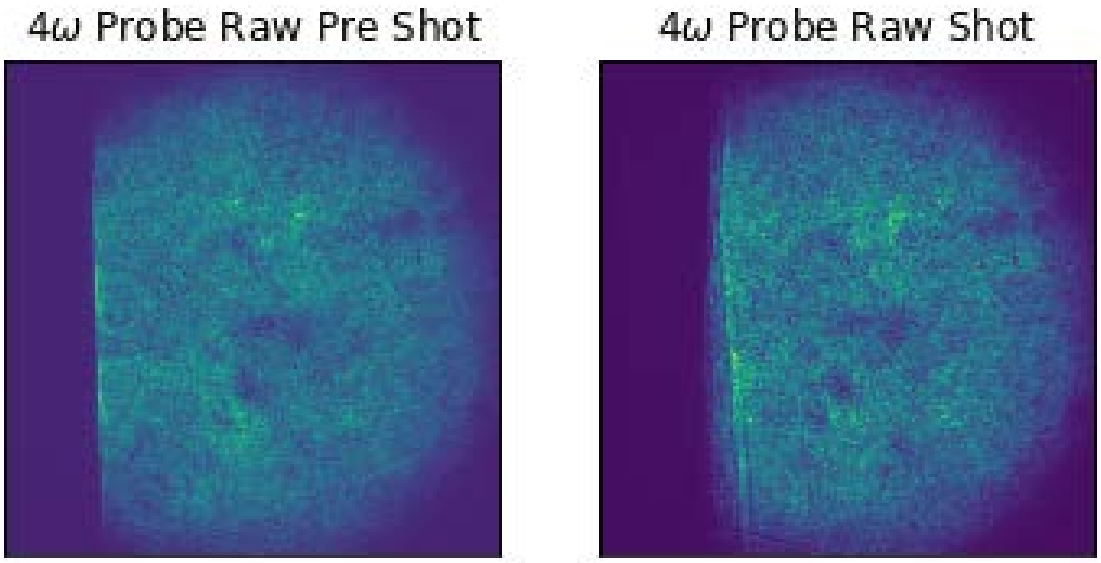

Figure C.2: Omega EP shot nums = 36789, 36790, t = 35 ns

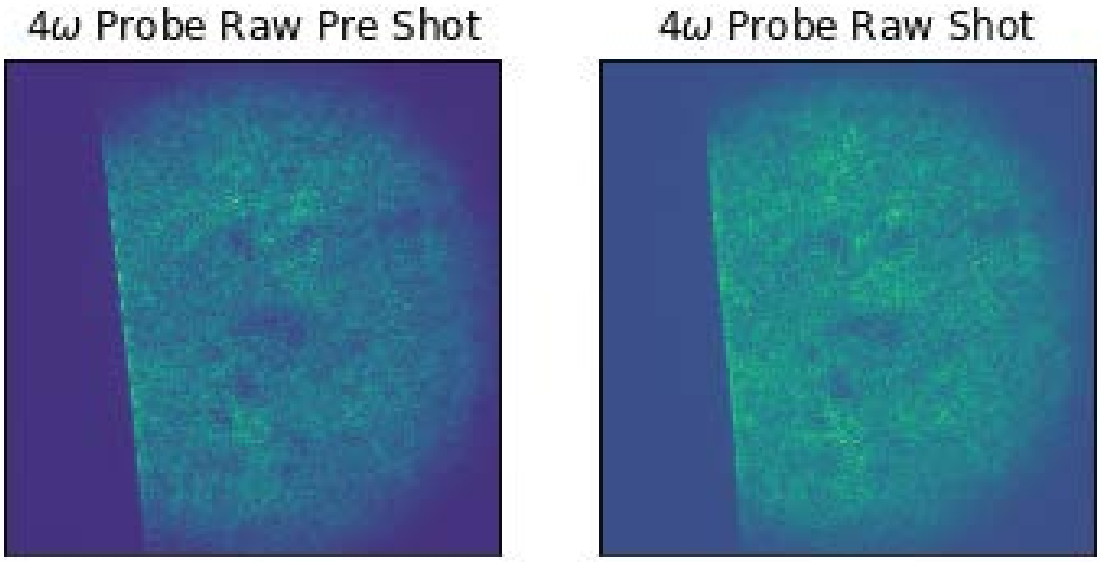

Figure C.3: Omega EP shot nums = 36791, 36792, t = 30 ns

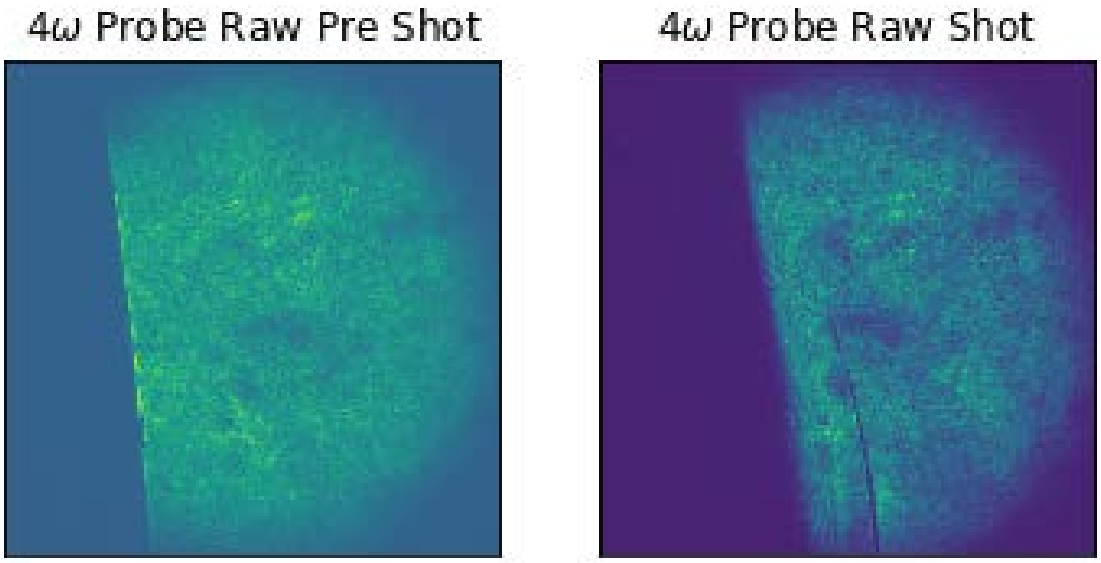

Figure C.4: Omega EP shot nums = 36793, 36785, t = 40 ns

APPENDIX D

Raw Radiographs

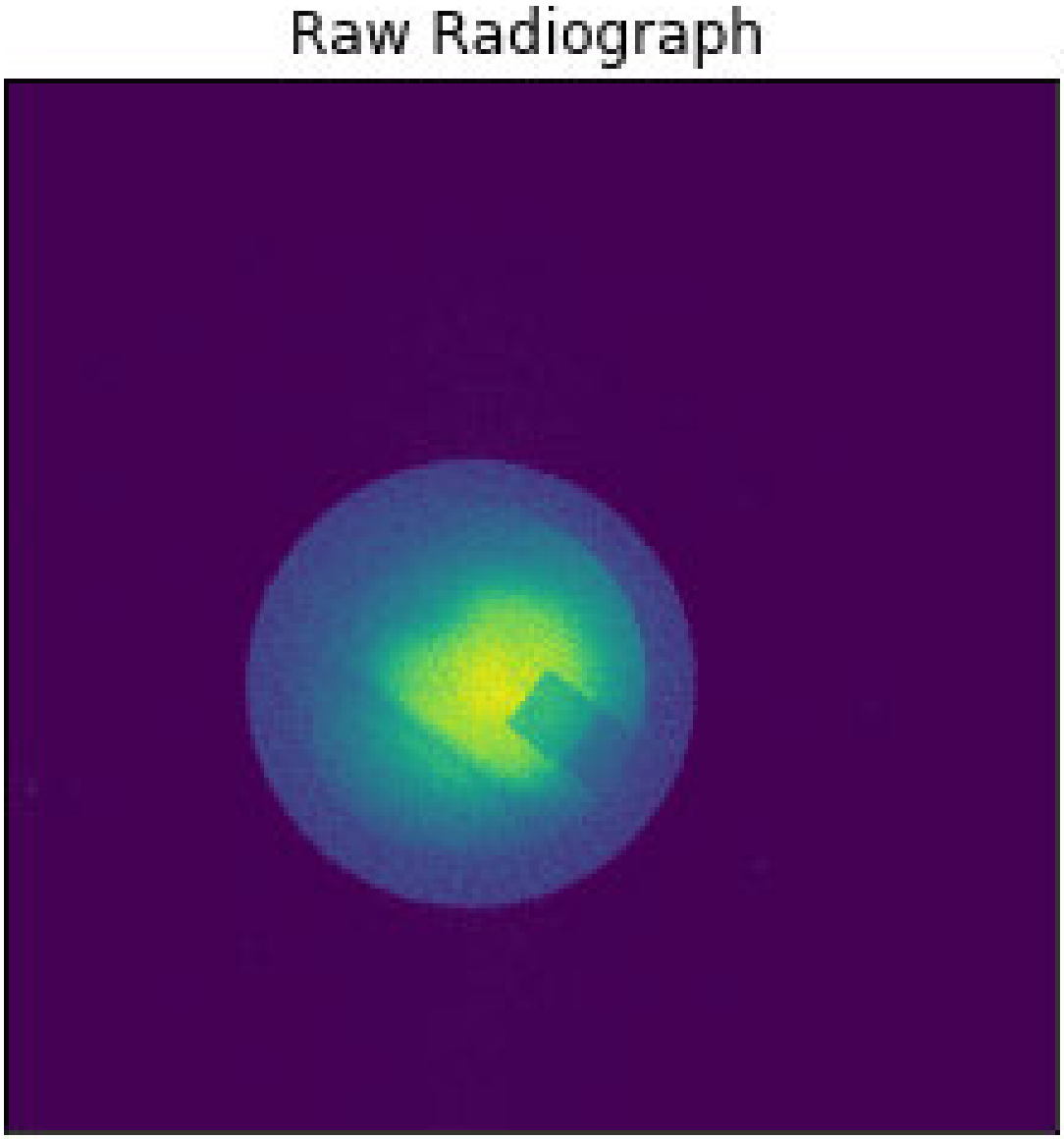

Figure D.1: Omega EP shot num = 36785, t = 35 ns

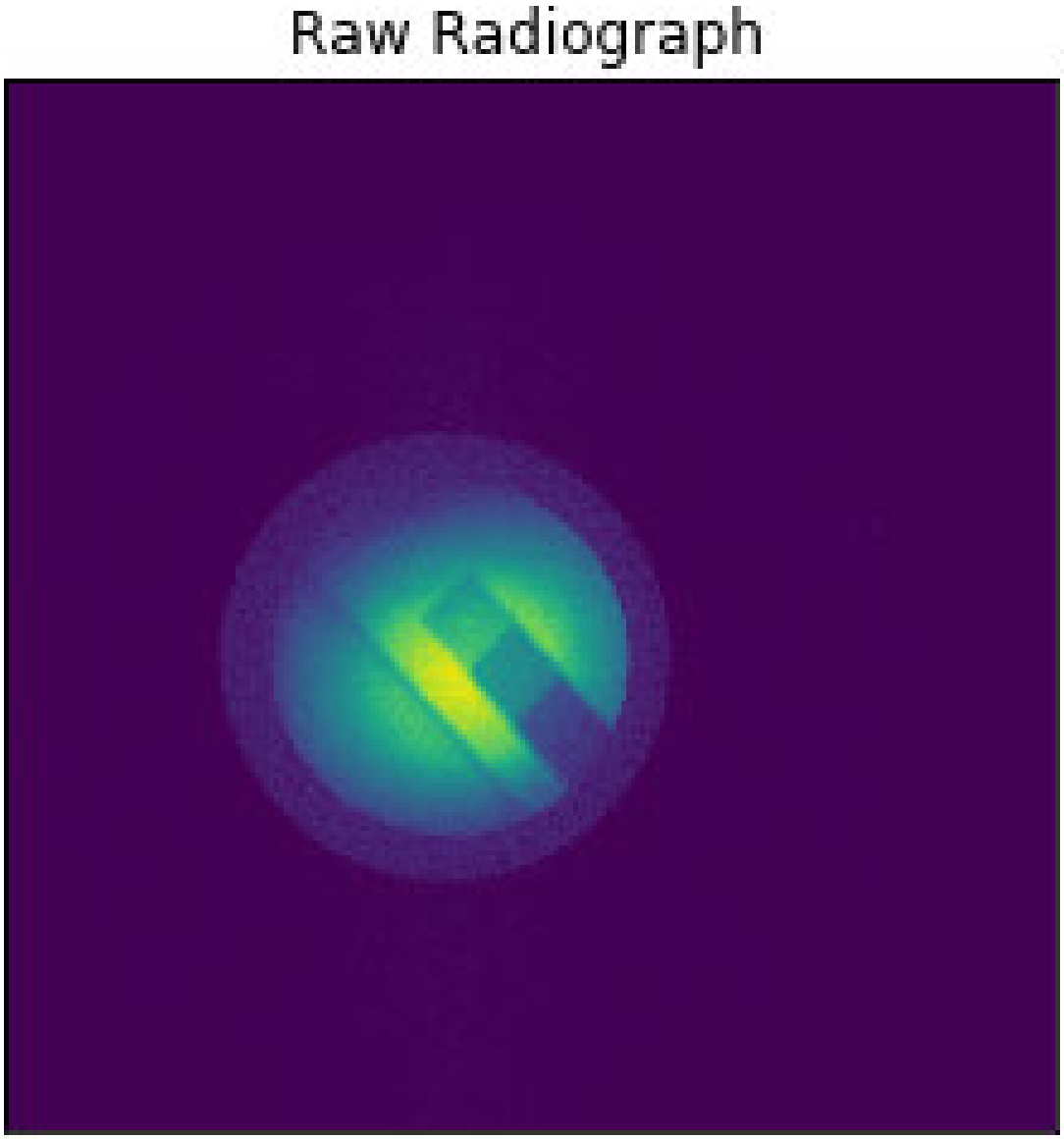

Figure D.2: Omega EP shot num = 36790, t = 20 ns

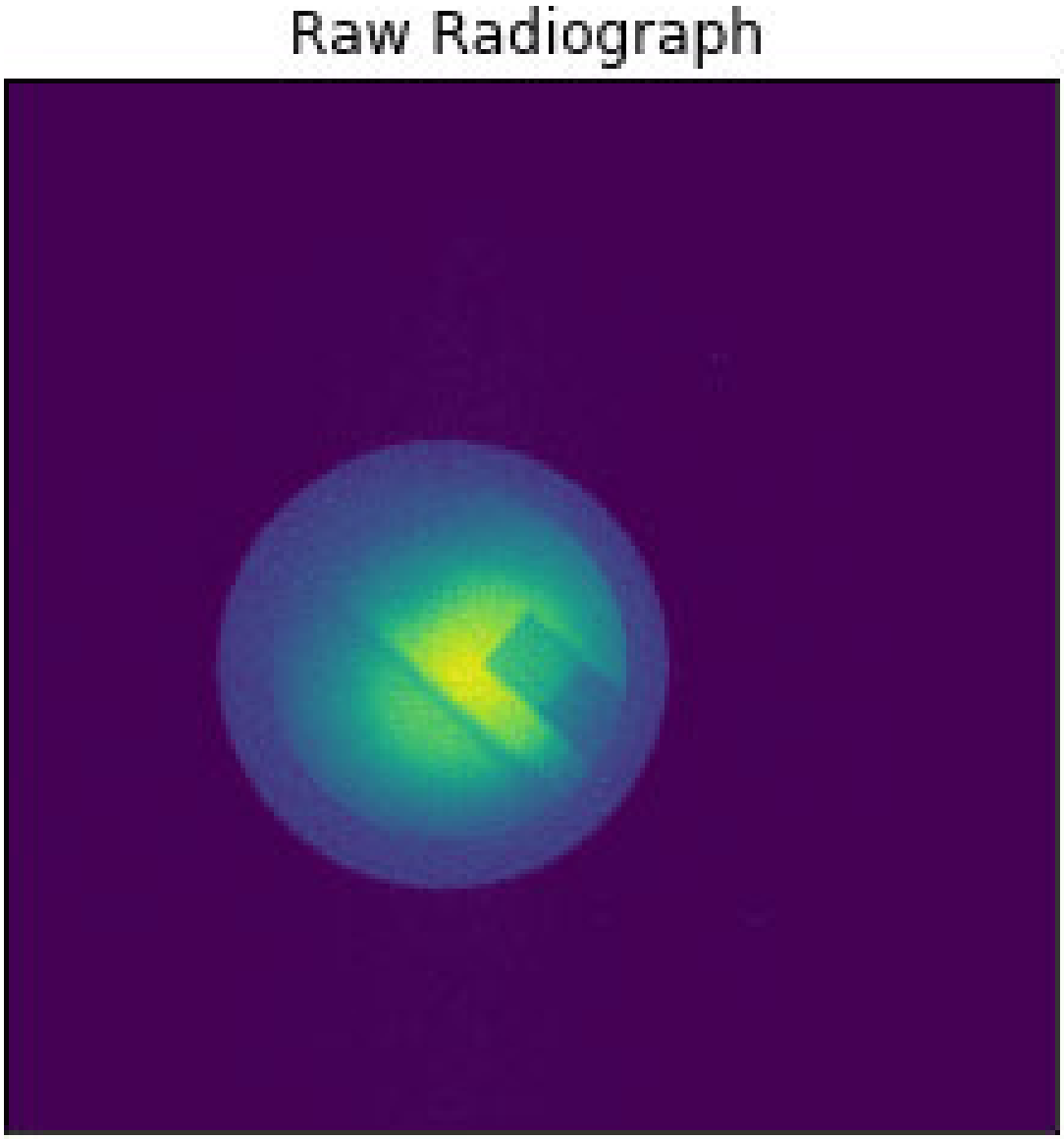

Figure D.3: Omega EP shot num = 36792, t = 30 ns

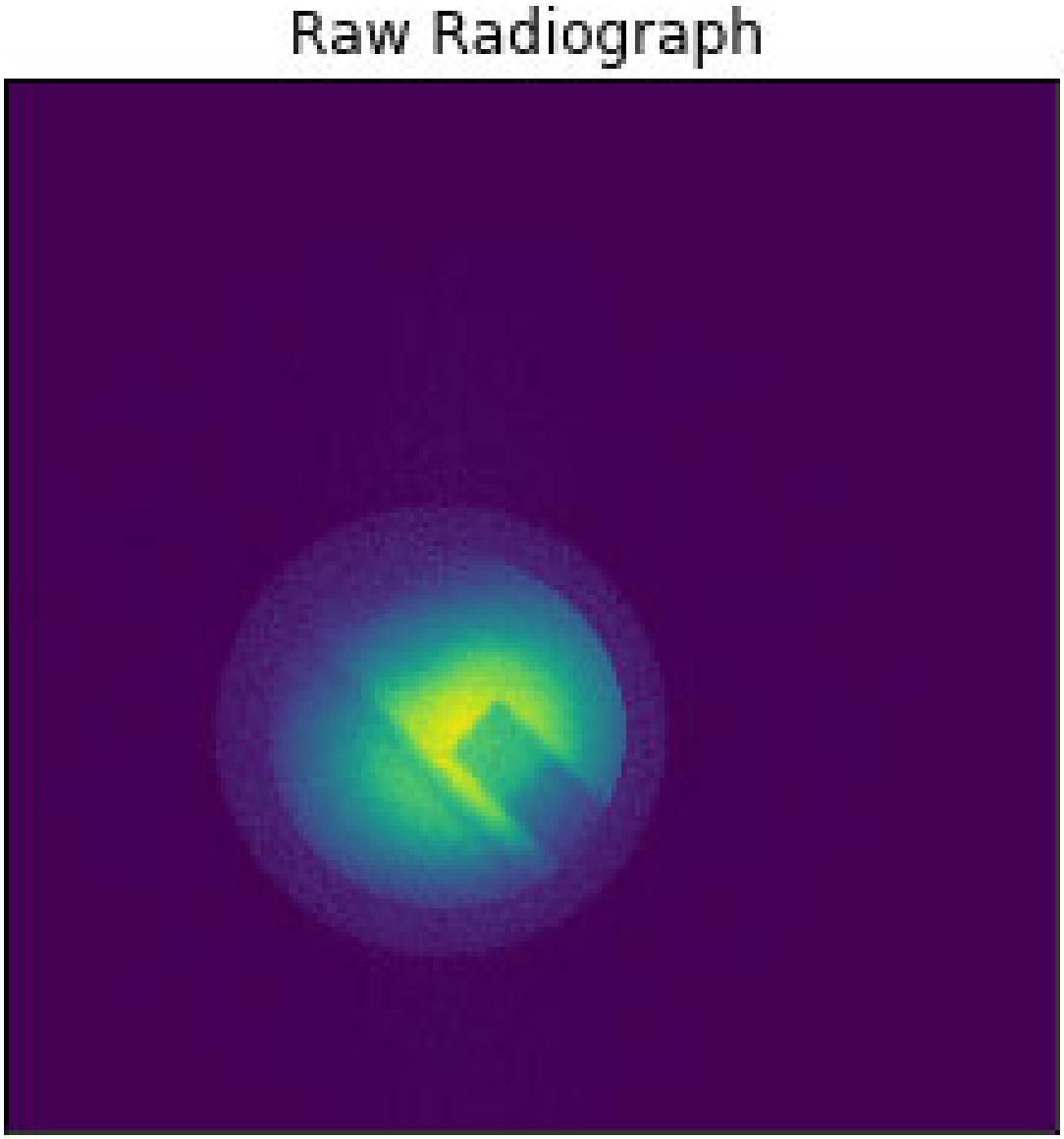

Figure D.4: Omega EP shot num = 36794, t = 10 ns

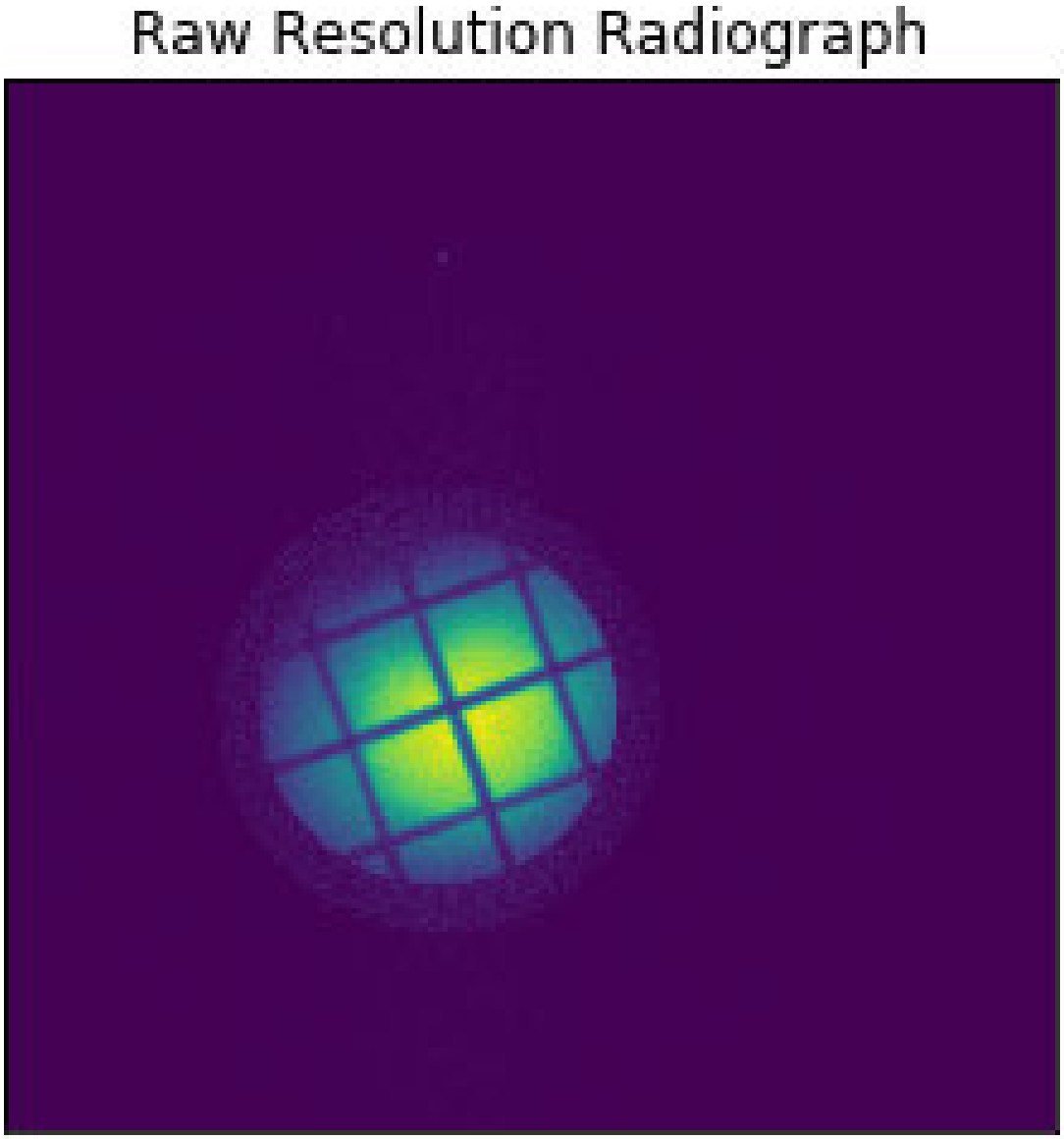

Figure D.5: Omega EP shot num = 36788

APPENDIX E

UofM Laser Gate Facility Upgrades and Potential Future Work

An updated test facility was designed and built to include a vacuum chamber to enclose the target and a Mach-Zehnder interferometer to calculate the density of the escaping gas.

The vacuum chamber has two window ports to allow entrance and exit of one of the interferometer beamlines, one port connected to the turbo pump to evacuate the chamber, one port for the target fill tube to fill the target in situ, and one port to supply current to the target's nichrome wire. The other end of the nichrome wire is attached to the inner chamber wall that is grounded. Fig. E.1 shows the target inside of the vacuum chamber.

A Mach-Zehnder interferometer produces a pattern of fringes when a laser beam is split, passed through a target and reference path, and recombined creating interference fringes. Figure E.2 shows the overview of the optical setup for the interferometer.

A sample of the fringes produced are shown in Figure E.3.

This facility could be used to perform detailed experiments into the current threshold needed to break the LEH window. To date, the current pulse used to remove the window was chosen to be one that would remove the window in air (not vacuum) but was not optimized. Now this experiment can be conducted in vacuum and optimization studies can be done. Additionally, opening dynamics are thought to slightly change in vacuum. This can be studied on the updated facility. Also, the interferometer would allow for detailed calculations of the density of the escaping target fuel. This project could be picked up by a future student. The results found in these detailed studies would inform potential design efforts to implement the pulsed power driven version of Laser Gate on fully integrated MagLIF experiments at SNL¿

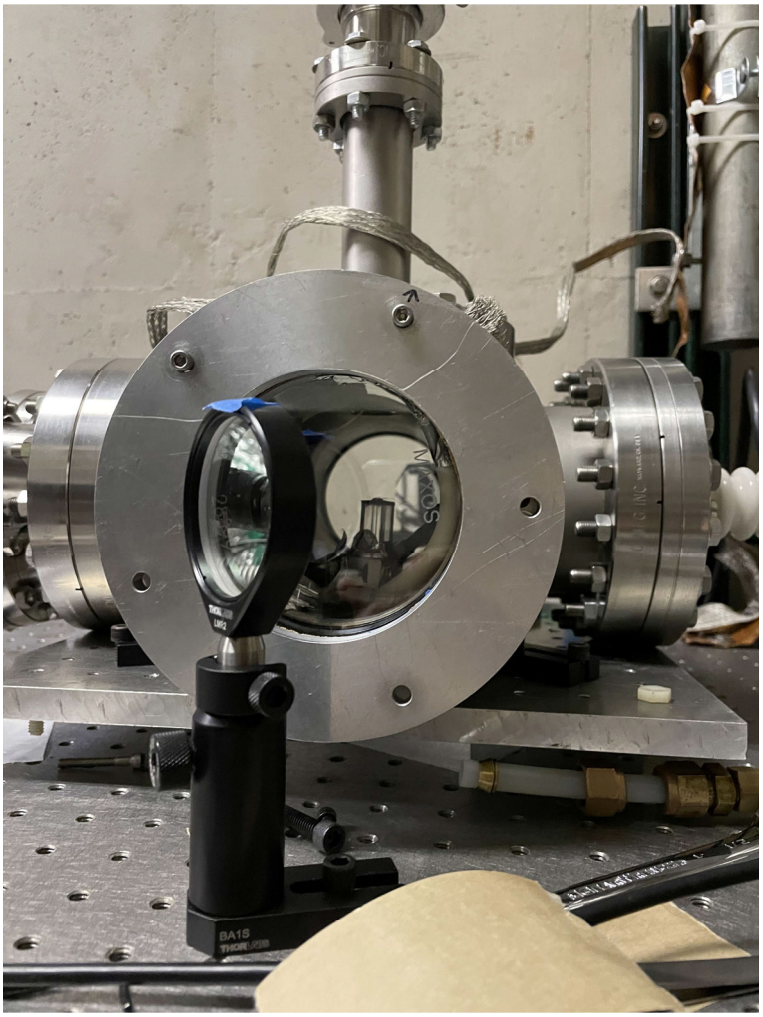

Figure E.1: target in chamber front and back windows for interferometry beam

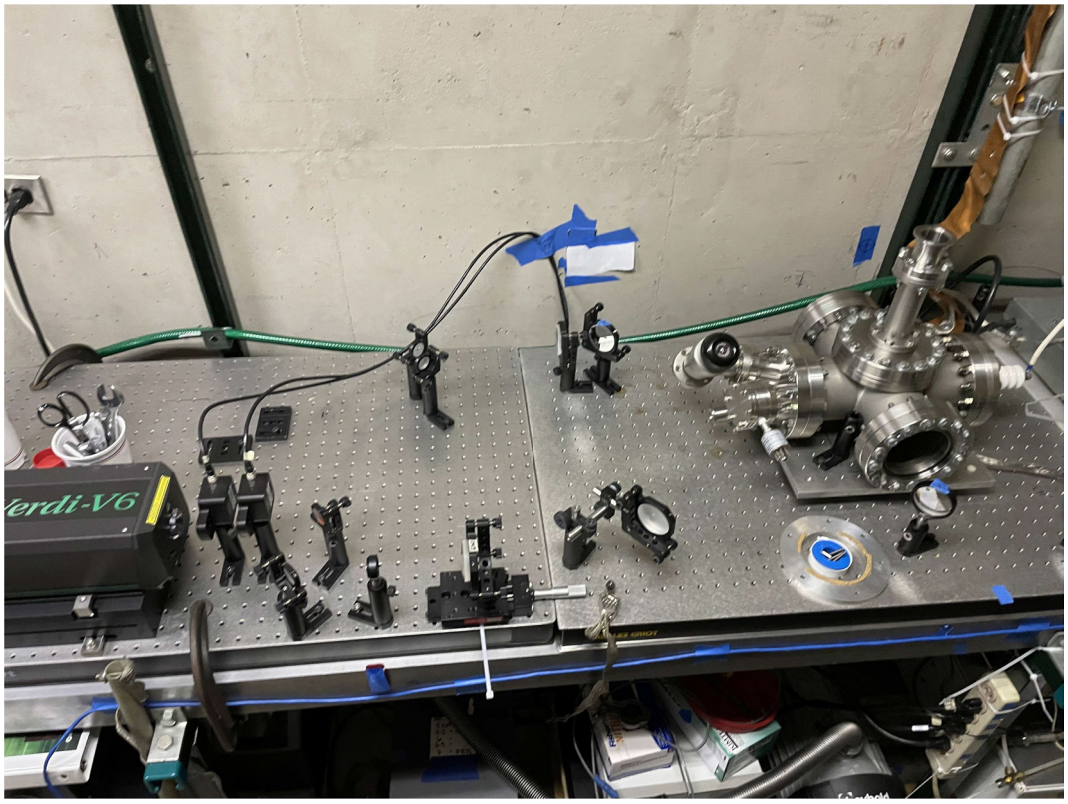

Figure E.2: overview of optical setup for interferometer

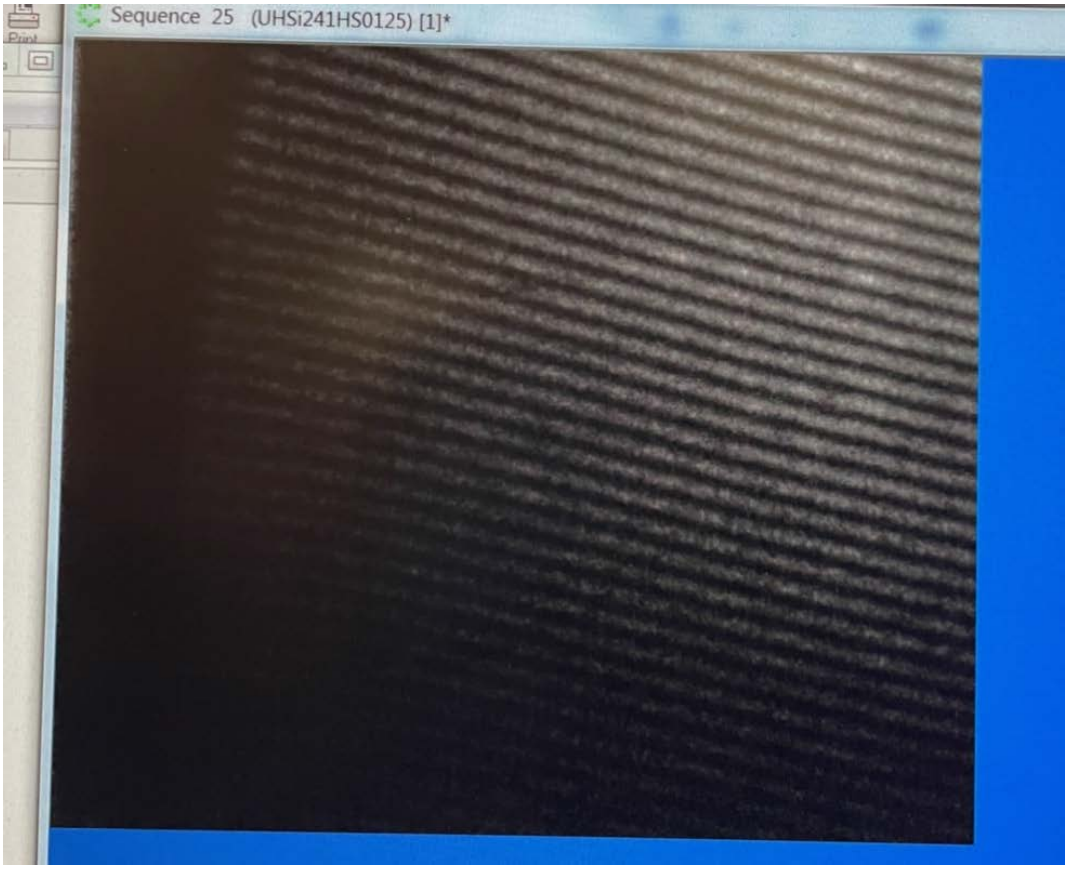

Figure E.3: target in chamber front and back windows for interferometry beam

BIBLIOGRAPHY

[1] M. R. Gomez, S. A. Slutz, A. B. Sefkow, D. B. Sinars, K. D. Hahn, S. B. Hansen, E. C. Harding, P. F. Knapp, P. F. Schmit, C. A. Jennings, T. J. Awe, M. Geissel, D. C. Rovang, G. A. Chandler, G. W. Cooper, M. E. Cuneo, A. J. Harvey-Thompson, M. C. Herrmann, M. H. Hess, O. Johns, D. C. Lamppa, M. R. Martin, R. D. McBride, K. J. Peterson, J. L. Porter, G. K. Robertson, G. A. Rochau, C. L. Ruiz, M. E. Savage, I. C. Smith, W. A. Stygar, and R. A. Vesey. Experimental demonstration of fusion-relevant conditions in magnetized liner inertial fusion. *Phys. Rev. Lett.*, 113:155003, Oct 2014.

[2] R. D. McBride, S. A. Slutz, R. A. Vesey, M. R. Gomez, A. B. Sefkow, S. B. Hansen, P. F. Knapp, P. F. Schmit, M. Geissel, A. J. Harvey-Thompson, C. A. Jennings, E. C. Harding, T. J. Awe, D. C. Rovang, K. D. Hahn, M. R. Martin, K. R. Cochrane, K. J. Peterson, G. A. Rochau, J. L. Porter, W. A. Stygar, E. M. Campbell, C. W. Nakhleh, M. C. Herrmann, M. E. Cuneo, and D. B. Sinars. Exploring magnetized liner inertial fusion with a semi-analytic model. *Physics of Plasmas*, 23(1):012705, 2016.

[3] S. A. Slutz, M. C. Herrmann, R. A. Vesey, A. B. Sefkow, D. B. Sinars, D. C. Rovang, K. J. Peterson, and M. E. Cuneo. Pulsed-power-driven cylindrical liner implosions of laser preheated fuel magnetized with an axial field. *Physics of Plasmas*, 17(5):056303, 2010.

[4] Ryan D. McBride and Stephen A. Slutz. A semi-analytic model of magnetized liner inertial fusion. *Physics of Plasmas*, 22(5):052708, 05 2015.

[5] D. H. Froula, R. Boni, M. Bedzyk, R. S. Craxton, F. Ehrne, S. Ivancic, R. Jungquist, M. J. Shoup, W. Theobald, D. Weiner, N. L. Kugland, and M. C. Rushford. Optical diagnostic suite (schlieren, interferometry, and grid image refractometry) on OMEGA EP using a 10-ps, 263-nm probe beama). *Review of Scientific Instruments*, 83(10):10E523, 07 2012.

[6] C. Stoeckl, G. Fiksel, D. Guy, C. Mileham, P. M. Nilson, T. C. Sangster, III Shoup, M. J., and W. Theobald. A spherical crystal imager for OMEGA EP. *Review of Scientific Instruments*, 83(3):033107, 03 2012.

[7] A. B. Zylstra, O. A. Hurricane, J. E. Ralph H. F. Robey J. S. Ross C. V. Young K. L. Baker D. T. Casey T. Döppner L. Divol M. Hohenberger S. Le Pape A. Pak P. K. Patel R. Tommasini S. J. Ali P. A. Amendt L. J. Atherton B. Bachmann D. Bailey L. R. Benedetti L. Berzak Hopkins R. Betti S. D. Bhandarkar J. Biener R. M. Bionta N. W. Birge E. J. Bond D. K. Bradley T. Braun T. M. Briggs M. W. Bruhn P. M. Celliers B. Chang T. Chapman H. Chen C. Choate A. R. Christopherson D. S. Clark J. W. Crippen E. L. Dewald T. R. Dittrich M. J. Edwards W.

A. Farmer J. E. Field D. Fittinghoff J. Frenje J. Gaffney M. Gatu Johnson S. H. Glenzer G. P. Grim S. Haan K. D. Hahn G. N. Hall B. A. Hammel J. Harte E. Hartouni J. E. Heebner V. J. Hernandez H. Herrmann M. C. Herrmann D. E. Hinkel D. D. Ho J. P. Holder W. W. Hsing H. Huang K. D. Humbird N. Izumi L. C. Jarrott J. Jeet O. Jones G. D. Kerbel S. M. Kerr S. F. Khan J. Kilkenny Y. Kim H. Geppert Kleinrath V. Geppert Kleinrath C. Kong J. M. Koning J. J. Kroll M. K. G. Kruse B. Kustowski O. L. Landen S. Langer D. Larson N. C. Lemos J. D. Lindl T. Ma M. J. MacDonald B. J. MacGowan A. J. Mackinnon S. A. MacLaren A. G. MacPhee M. M. Marinak D. A. Mariscal E. V. Marley L. Masse K. Meaney N. B. Meezan P. A. Michel M. Millot J. L. Milovich J. D. Moody A. S. Moore J. W. Morton T. Murphy K. Newman J.-M. G. Di Nicola A. Nikroo R. Nora M. V. Patel L. J. Pelz J. L. Peterson Y. Ping B. B. Pollock M. Ratledge N. G. Rice H. Rinderknecht M. Rosen M. S. Rubery J. D. Salmonson J. Sater S. Schiaffino D. J. Schlossberg M. B. Schneider C. R. Schroeder H. A. Scott S. M. Sepke K. Sequoia M. W. Sherlock S. Shin V. A. Smalyuk B. K. Spears P. T. Springer M. Stadermann S. Stoupin D. J. Strozzi L. J. Suter C. A. Thomas R. P. J. Town E. R. Tubman C. Trosseille P. L. Volegov C. R. Weber K. Widmann C. Wild C. H. Wilde B. M. Van Wonterghem D. T. Woods B. N. Woodworth M. Yamaguchi S. T. Yang D. A. Callahan, A. L. Kritcher, and G. B. Zimmerman. Burning plasma achieved in inertial fusion. *Nature*, 601:542–548, 2022.

[8] David Kramer. National ignition facility surpasses long-awaited fusion milestone, 2022.

[9] M. E. Cuneo, M. C. Herrmann, D. B. Sinars, S. A. Slutz, W. A. Stygar, R. A. Vesey, A. B. Sefkow, G. A. Rochau, G. A. Chandler, J. E. Bailey, J. L. Porter, R. D. McBride, D. C. Rovang, M. G. Mazarakis, E. P. Yu, D. C. Lamppa, K. J. Peterson, C. Nakhleh, S. B. Hansen, A. J. Lopez, M. E. Savage, C. A. Jennings, M. R. Martin, R. W. Lemke, B. W. Atherton, I. C. Smith, P. K. Rambo, M. Jones, M. R. Lopez, P. J. Christenson, M. A. Sweeney, B. Jones, L. A. McPherson, E. Harding, M. R. Gomez, P. F. Knapp, T. J. Awe, R. J. Leeper, C. L. Ruiz, G. W. Cooper, K. D. Hahn, J. McKenney, A. C. Owen, G. R. McKee, G. T. Leifeste, D. J. Ampleford, E. M. Waisman, A. Harvey-Thompson, R. J. Kaye, M. H. Hess, S. E. Rosenthal, and M. K. Matzen. Magnetically driven implosions for inertial confinement fusion at sandia national laboratories. *IEEE Transactions on Plasma Science*, 40(12):3222–3245, 2012.

[10] S. A. Slutz, M. R. Gomez, S. B. Hansen, E. C. Harding, B. T. Hutsel, P. F. Knapp, D. C. Lamppa, T. J. Awe, D. J. Ampleford, D. E. Bliss, G. A. Chandler, M. E. Cuneo, M. Geissel, M. E. Glinsky, A. J. Harvey-Thompson, M. H. Hess, C. A. Jennings, B. Jones, G. R. Laity, M. R. Martin, K. J. Peterson, J. L. Porter, P. K. Rambo, G. A. Rochau, C. L. Ruiz, M. E. Savage, J. Schwarz, P. F. Schmit, G. Shipley, D. B. Sinars, I. C. Smith, R. A. Vesey, and M. R. Weis. Enhancing performance of magnetized liner inertial fusion at the z facility. *Physics of Plasmas*, 25(11):112706, 2018.

[11] M. R. Gomez, S. A. Slutz, P. F. Knapp, K. D. Hahn, M. R. Weis, E. C. Harding, M. Geissel, J. R. Fein, M. E. Glinsky, S. B. Hansen, A. J. Harvey-Thompson, C. A. Jennings, I. C. Smith, D. Woodbury, D. J. Ampleford, T. J. Awe, G. A. Chandler, M. H. Hess, D. C. Lamppa, C. E. Myers, C. L. Ruiz, A. B. Sefkow, J. Schwarz, D. A. Yager-Elorriaga, B. Jones, J. L. Porter, K. J. Peterson, R. D. Mcbride, G. A. Rochau, and D. B. Sinars. Assessing Stagnation Conditions and Identifying Trends in Magnetized Liner Inertial Fusion. *IEEE Transactions on Plasma Science*, 47(5):2081–2101, May 2019.

[12] S. M. Miller, S. A. Slutz, S. N. Bland, S. R. Klein, P. C. Campbell, J. M. Woolstrum, C. C. Kuranz, M. R. Gomez, N. M. Jordan, and R. D. McBride. A pulsed-power implementation of "Laser Gate" for increasing laser energy coupling and fusion yield in magnetized liner inertial fusion (MagLIF). *Review of Scientific Instruments*, 91(6):063507, 06 2020.

[13] P. F. Knapp, M. R. Gomez, S. B. Hansen, M. E. Glinsky, C. A. Jennings, S. A. Slutz, E. C. Harding, K. D. Hahn, M. R. Weis, M. Evans, M. R. Martin, A. J. Harvey-Thompson, M. Geissel, I. C. Smith, D. E. Ruiz, K. J. Peterson, B. M. Jones, J. Schwarz, G. A. Rochau, D. B. Sinars, R. D. McBride, and P.-A. Gourdain. Origins and effects of mix on magnetized liner inertial fusion target performance. *Physics of Plasmas*, 26(1):012704, 2019.

[14] Matthias Geissel, Adam J. Harvey-Thompson, Thomas J. Awe, David E. Bliss, Michael E. Glinsky, Matthew R. Gomez, Eric Harding, Stephanie B. Hansen, Christopher Jennings, Mark W. Kimmel, Patrick Knapp, Sean M. Lewis, Kyle Peterson, Marius Schollmeier, Jens Schwarz, Jonathon E. Shores, Stephen A. Slutz, Daniel B. Sinars, Ian C. Smith, C. Shane Speas, Roger A. Vesey, Matthew R. Weis, and John L. Porter. Minimizing scatter-losses during pre-heat for magneto-inertial fusion targets. *Physics of Plasmas*, 25(2):022706, 2018.

[15] A. Dunaevsky, A. Goltsov, J. Greenberg, E. Valeo, and N. J. Fisch. Formation of laser plasma channels in a stationary gas. *Physics of Plasmas*, 13(4):043106, 2006.

[16] A. J. Harvey-Thompson, M. Geissel, C. A. Jennings, M. R. Weis, M. R. Gomez, J. R. Fein, D. J. Ampleford, G. A. Chandler, M. E. Glinsky, K. D. Hahn, S. B. Hansen, E. C. Harding, P. F. Knapp, R. R. Paguio, L. Perea, K. J. Peterson, J. L. Porter, P. K. Rambo, G. K. Robertson, G. A. Rochau, C. L. Ruiz, J. Schwarz, J. E. Shores, D. B. Sinars, S. A. Slutz, G. E. Smith, I. C. Smith, C. S. Speas, K. Whittemore, and D. Woodbury. Constraining preheat energy deposition in maglif experiments with multi-frame shadowgraphy. *Physics of Plasmas*, 26(3):032707, 2019.

[17] J. R. Davies, R. E. Bahr, D. H. Barnak, R. Betti, M. J. Bonino, E. M. Campbell, E. C. Hansen, D. R. Harding, J. L. Peebles, A. B. Sefkow, W. Seka, P.-Y. Chang, M. Geissel, and A. J. Harvey-Thompson. Laser entrance window transmission and reflection measurements for preheating in magnetized liner inertial fusion. *Physics of Plasmas*, 25(6):062704, 2018.

[18] Benjamin Galloway. personal communication, 2019.

[19] B. R. Galloway, S. A. Slutz, M. W. Kimmel, P. K. Rambo, J. Schwarz, M. Geissel, A. J. Harvey-Thompson, M. R. Weis, C. A. Jennings, E. S. Field, D. E. Kletecka, Q. Looker, A. P. Colombo, A. D. Edens, I. C. Smith, J. E. Shores, C. S. Speas, R. J. Speas, A. P. Spann, J. Sin, S. Gautier, V. Sauget, P. A. Treadwell, G. A. Rochau, and J. L. Porter. Lasergate: A windowless gas target for enhanced laser preheat in magnetized liner inertial fusion. *Physics of Plasmas*, 28(11):112703, 2021.

[20] S. W. Haan, P. A. Amendt, D. A. Callahan, T. R. Dittrich, M. J. Edwards, B. A. Hammel, D. D. Ho, O. S. Jones, J. D. Lindl, M. M. Marinak, D. H. Munro, S. M. Pollaine, J. D. Salmonson, B. K. Spears, and L. J. Suter. Update on specifications for nif ignition targets. *Fusion Science and Technology*, 51(4):509–513, 2007.

[21] Bruce Lairson, Ryan Smith, Jeff Guckian, Travis Ayers, and Suhas Bhandarkar. Laser entrance hole window burst and pressure deflections at cryogenic temperature. *Fusion Science and Technology*, 59(1):262–266, 2011.

[22] Eleanor R. Tubman, Bradley B. Pollock, David J. Strozzi, Steven Ross, Ryan Lau, John D. Moody, Adam J. Harvey-Thomspon, Matthew R. Weis, Michael E. Glinsky, Stephanie B. Hansen, Evstati G. Evstatiev, David J. Ampleford, and Kristian Beckwith. Measuring mix in maglif experiments at the nif. In *2021 IEEE International Conference on Plasma Science (ICOPS)*, pages 1–1, 2021.

[23] Stephen A. Slutz and Roger A. Vesey. High-gain magnetized inertial fusion. *Phys. Rev. Lett.*, 108:025003, Jan 2012.

[24] S. A. Slutz, T. J. Awe, and J. A. Crabtree. Dense hydrogen layers for high performance MagLIF. *Physics of Plasmas*, 29(2):022701, 2022.

[25] Loren C. Steinhauer and Harlow G. Ahlstrom. Bleaching wave phenomena. *AIAA Journal*, 10(4):429–433, 1972.

[26] Matthias Geissel, Adam J. Harvey-Thompson, Thomas J. Awe, David E. Bliss, Michael E. Glinsky, Matthew R. Gomez, Eric Harding, Stephanie B. Hansen, Christopher Jennings, Mark W. Kimmel, Patrick Knapp, Sean M. Lewis, Kyle Peterson, Marius Schollmeier, Jens Schwarz, Jonathon E. Shores, Stephen A. Slutz, Daniel B. Sinars, Ian C. Smith, C. Shane Speas, Roger A. Vesey, Matthew R. Weis, and John L. Porter. Minimizing scatter-losses during pre-heat for magneto-inertial fusion targets. *Physics of Plasmas*, 25(2):022706, 02 2018.

[27] C. Labaune, E. Fabre, A. Michard, and F. Briand. Evidence of stimulated brillouin backscattering from a plasma at short laser wavelengths. *Phys. Rev. A*, 32:577–580, Jul 1985.

[28] D. H. Froula, L. Divol, N. B. Meezan, S. Dixit, J. D. Moody, P. Neumayer, B. B. Pollock, J. S. Ross, and S. H. Glenzer. Ideal laser-beam propagation through high-temperature ignition hohlraum plasmas. *Phys. Rev. Lett.*, 98:085001, Feb 2007.

[29] R. P. Drake, R. E. Turner, B. F. Lasinski, E. A. Williams, D. W. Phillion, K. G. Estabrook, W. L. Kruer, E. M. Campbell, K. R. Manes, J. S. Hildum, and T. W. Johnston. Studies of Raman scattering from overdense targets irradiated by several kilojoules of 0.53 μm laser light. *The Physics of Fluids*, 31(10):3130–3142, 10 1988.

[30] H. Figueroa, C. Joshi, H. Azechi, N. A. Ebrahim, and Kent Estabrook. Stimulated Raman scattering, two-plasmon decay, and hot electron generation from underdense plasmas at 0.35 μm. *The Physics of Fluids*, 27(7):1887–1896, 07 1984.

[31] M. M. Marinak, R. E. Tipton, O. L. Landen, T. J. Murphy, P. Amendt, S. W. Haan, S. P. Hatchett, C. J. Keane, R. McEachern, and R. Wallace. Three-dimensional simulations of Nova high growth factor capsule implosion experiments. *Physics of Plasmas*, 3(5):2070–2076, 05 1996.

[32] A. B. Sefkow, S. A. Slutz, J. M. Koning, M. M. Marinak, K. J. Peterson, D. B. Sinars, and R. A. Vesey. Design of magnetized liner inertial fusion experiments using the Z facility. *Physics of Plasmas*, 21(7):072711, 07 2014.

[33] A. J. Harvey-Thompson, A. B. Sefkow, T. N. Nagayama, M. S. Wei, E. M. Campbell, G. Fiksel, P.-Y. Chang, J. R. Davies, D. H. Barnak, V. Y. Glebov, P. Fitzsimmons, J. Fooks, and B. E. Blue. Diagnosing laser-preheated magnetized plasmas relevant to magnetized liner inertial fusion. *Physics of Plasmas*, 22(12):122708, 12 2015.

[34] A. J. Harvey-Thompson, A. B. Sefkow, M. S. Wei, T. Nagayama, E. M. Campbell, B. E. Blue, R. F. Heeter, J. M. Koning, K. J. Peterson, and A. Schmitt. Laser propagation measurements in long-scale-length underdense plasmas relevant to magnetized liner inertial fusion. *Phys. Rev. E*, 94:051201, Nov 2016.

[35] Ian Karlin Steven H. Langer and Michael M. Marinak. Performance characteristics of hydra, a multi-physics simulation code from llnl. In *VECPAR*, 2014.

[36] Dean Rovang Adam Sefkow Stephen Slutz Ray Lemke Michael Cuneo Mark Herrmann Chris Jennings Marc Jobe Derek Lamppa Matt Martin Charlie Nakhleh Albert Owen John McKenney Ray Mock Todd Peters Gerald Torres Eduardo Waisman Daniel B. Sinars, Ryan McBride. Stability of fusion target concepts on z. Technical report, Sandia National Laboratories, 09 2012.

[37] M. R. Gomez, S. A. Slutz, A. B. Sefkow, K. D. Hahn, S. B. Hansen, P. F. Knapp, P. F. Schmit, C. L. Ruiz, D. B. Sinars, E. C. Harding, C. A. Jennings, T. J. Awe, M. Geissel, D. C. Rovang, I. C. Smith, G. A. Chandler, G. W. Cooper, M. E. Cuneo, A. J. Harvey-Thompson, M. C. Herrmann, M. H. Hess, D. C. Lamppa, M. R. Martin, R. D. McBride, K. J. Peterson, J. L. Porter, G. A. Rochau, M. E. Savage, D. G. Schroen, W. A. Stygar, and R. A. Vesey. Demonstration of thermonuclear conditions in magnetized liner inertial fusion experiments. *Physics of Plasmas*, 22(5):056306, 2015.

[38] Adam M. Steiner. *The Electrothermal Instability on Pulsed Power Ablations of Thin Foils*. PhD thesis, University of Michigan, 2016.

[39] A. M. Steiner, P. C. Campbell, D. A. Yager-Elorriaga, N. M. Jordan, R. D. Mcbride, Y. Y. Lau, and R. M. Gilgenbach. The Electrothermal Instability on Pulsed Power Ablations of Thin Foils. *IEEE Transactions on Plasma Science*, 46(11):3753–3765, Nov 2018.

[40] John Hall Gladstone and T.P. Dale. Researchers on the refraction, dispersion, and sensitiveness of liquids. *Royal Society*, 153:317, 343, 1863.

[41] D. C. Rovang, D. C. Lamppa, M. E. Cuneo, A. C. Owen, J. McKenney, D. W. Johnson, S. Radovich, R. J. Kaye, R. D. McBride, C. S. Alexander, T. J. Awe, S. A. Slutz, A. B. Sefkow, T. A. Haill, P. A. Jones, J. W. Argo, D. G. Dalton, G. K. Robertson, E. M. Waisman, D. B. Sinars, J. Meissner, M. Milhous, D. N. Nguyen, and C. H. Mielke. Pulsed-coil magnet systems for applying uniform 10–30 T fields to centimeter-scale targets on Sandia's Z facility. *Rev. Sci. Instrum.*, 85(12):–, 2014.

[42] D N Maywar, J H Kelly, L J Waxer, S F B Morse, I A Begishev, J Bromage, C Dorrer, J L Edwards, L Folnsbee, M J Guardalben, S D Jacobs, R Jungquist, T J Kessler, R W Kidder, B E Kruschwitz, S J Loucks, J R Marciante, R L McCrory, D D Meyerhofer, A V Okishev, J B Oliver, G Pien, J Qiao, J Puth, A L Rigatti, A W Schmid, M J Shoup III, C Stoeckl, K A Thorp, and J D Zuegel. Omega ep high-energy petawatt laser: progress and prospects. *Journal of Physics: Conference Series*, 112(3):032007, may 2008.

[43] C. Stoeckl, G. Fiksel, D. Guy, C. Mileham, P. M. Nilson, T. C. Sangster, III Shoup, M. J., and W. Theobald. A spherical crystal imager for OMEGA EP. *Review of Scientific Instruments*, 83(3):033107, 03 2012.

[44] M. R. Weis, A. J. Harvey-Thompson, and D. E. Ruiz. Scaling laser preheat for MagLIF with the Z-Beamlet laser. *Physics of Plasmas*, 28(1):012705, 01 2021.

[45] B.L. Henke, E.M. Gullikson, and J.C. Davis. X-ray interactions: Photoabsorption, scattering, transmission, and reflection at e = 50-30,000 ev, z = 1-92. *Atomic Data and Nuclear Data Tables*, 54(2):181–342, 1993.

[46] R. D. McBride, S. A. Slutz, C. A. Jennings, D. B. Sinars, M. E. Cuneo, M. C. Herrmann, R. W. Lemke, M. R. Martin, R. A. Vesey, K. J. Peterson, A. B. Sefkow, C. Nakhleh, B. E. Blue, K. Killebrew, D. Schroen, T. J. Rogers, A. Laspe, M. R. Lopez, I. C. Smith, B. W. Atherton, M. Savage, W. A. Stygar, and J. L. Porter. Penetrating radiography of imploding and stagnating beryllium liners on the z accelerator. *Phys. Rev. Lett.*, 109:135004, Sep 2012.